2023년 2월
석사학위 논문

Functional Energy Material with Ion-conductible and Robust Structure for Enhanced Electrochemical Performance

조 선 대 학 교 대 학 원

화 학 공 학 과

박 희 경

Functional Energy Material with Ion-conductible and Robust Structure for Enhanced Electrochemical Performance

전기화학적 성능 향상을 위한 이온전도성 및 견고한 구조의 기능성 에너지 재료

2023년 2월 24일

조 선 대 학 교 대 학 원

화 학 공 학 과

박 희 경

Functional Energy Material with Ion-conductible and Robust Structure for Enhanced Electrochemical Performance

지 도 교 수 이정수

이 논문을 공학 석사학위신청 논문으로 제출함

2022년 10월

조 선 대 학 교 대 학 원

화 학 공 학 과

박 희 경

박희경의 석사학위논문을 인준함

위 원 장 조선대학교 교 수 이 중 헌 (인)

위 원 조선대학교 교 수 이 정 수 (인)

위 원 조선대학교 교 수 안 성 훈 (인)

2022년 12월

조 선 대 학 교 대 학 원

CONTENTS

List of Tables ····· vi

List of Figures ····· vii

ABSTRACT ····· xiv

Ⅰ. Introduction ····· 1

A. Background of Study ····· 1

B. Background of Experimental ····· 3

1. Energy Storage Device ····· 3

a. Lithium Ion Battery (LIBs) ····· 3

b. Supercapacitor ····· 5

2. Electrode Configuration ····· 7

a. Cathode ····· 7

b. Anode ····· 9

c. Electrolyte ····· 11

d. Binder ····· 12

C. Ionic liquid ····· 15

D. Purpose of Research ····· 18

Ⅱ. Dual Effect-Assisted Polymer Binder of LIBs ····· 19

A. Introduction ····· 19

B. Experimental ····· 23

1. Materials ····· 23

2. Method ····· 23

a. Synthesis of Poly(vinyl imidazole) ····· 23

b. Quaternization of PVIm with Allyl bromide ····· 23

c. Anion Exchange of Poly(N-allyl-vinyl imidazolium)·$TFSI^-$ ····· 23

d. Thermal Cross-linked Poly(N-allyl-vinyl imidazolium)·$TFSI^-$ ····· 24

3. Characterization ····· 24

4. Electrochemical Characterization ····· 24

C. Results and Discussion ····· 26

1. ^{1}H-NMR Spectra ····· 27

2. FT-IR Spectra ····· 29

3. Gel Content Analysis ····· 31

4. DSC Curves ····· 33

5. TGA Curves ····· 35

6. SEM Images ····· 37

7. XPS Spectra ····· 39

8. Electrochemical Analysis ····· 42

D. Conclusion ····· 44

Ⅲ. Radical Scavenging and Robust Polymer Binder ····· 45

A. Introduction ····· 45

B. Experimental ····· 48

1. Materials ····· 48

2. Method ····· 48

a. Prepared PAA/TAc Film ····· 48

b. DPPH Radical Scavenging Assay ····· 48

3. Characterization ····· 49

4. Preparation of Si anode for Half-Cells ····· 49

5. Electrochemical Characterization ····· 50

C. Results and Discussion ····· 51

1. FT-IR Spectra ····· 52

2. Gel Content Analysis ····· 56

3. DSC Curves ····· 58

4. TGA Curves ····· 60

5. DPPH Radical Scavenging activity ····· 62

6. Electrochemical Analysis ····· 65

7. SEM Images ····· 71

8. Electrochemical Performances ····· 73

D. Conclusion ····· 76

Ⅳ. Cross-Linked Organic/Inorganic Polymer Binder ····· 77

A. Introduction ····· 77

B. Experimental ····· 80

1. Materials ····· 80

2. Method ····· 80

a. Synthesis of Poly(vinyl imidazole) ····· 80

b. Quaternization of PVIm with 3CPTES ····· 80

c. Cross-linked Poly(1-vinyl-propyl triethoxysilane imidazolium)·Cl^- · 81

d. Synthesis of $Ni(OH)_2$ Nanostructure ····· 81

e. Synthesis of Porous NiO Nanostructure ····· 81

3. Characterization ····· 81

4. Electrochemical Characterization ····· 82

C. Results and Discussion ····· 83

1. ^{1}H-NMR Spectra ····· 85

2. FT-IR Spectra ····· 88

3. Gel Content Analysis ····· 94

4. TGA Curves ····· 97

5. 180^o Peeling Test ····· 100

6. SEM Images ····· 102

7. Electrochemical Analysis ····· 107

D. Conclusion ····· 111

Ⅴ. Summary ····· 112

References ····· 113

List of Tables

[Ⅲ. Radical Scavenging and Robust Polymer Binder]

Table 1. Electrochemical performances of Si PAA, Si TAc and Si C-PAA/TAc. ····· 68

Table 2. EIS data of Si PAA, Si TAc and Si C-PAA/TAc after 100th cycles. ····· 69

[Ⅳ. Cross-Linked Organic/Inorganic Polymer Binder]

Table 1. List of band assignments for FT-IR spectra. ····· 92

Table 2. FT-IR spectra peak and corresponding functional groups of PVIm_Si. ····· 93

List of Figures

[Ⅰ. Introduction]

Figure 1. Operation of LIBs. ····· 4

Figure 2. Operation of supercapacitor (a) EDLC, (b) PSEUDO. ····· 6

Figure 3. Representative crystal structures of cathode materials for LIBs. ···· 8

Figure 4. Carbon-based anode materials. ····· 10

Figure 5. Challenges of Si-based anodes in LIBs. ····· 10

Figure 6. Progress of nanostructured metal oxides. ····· 10

Figure 7. Schematic illustrations of electrode configuration. ····· 14

Figure 8. Binder requirement characteristics. ····· 14

Figure 9. Typical cations and anions used in the formation of ILs. ····· 16

Figure 10. Advances on the use of PIL-based electrolytes and binders for LIBs. ····· 17

[Ⅱ. Dual Effect-Assisted Polymer Binder of LIBs]

Figure 1. Description of uncross-linked and cross-linked rubber chains. ····· 21

Figure 2. Illustration showing ion channel expansion of research concept. · 21

Figure 3. Illustration showing dual-effect binder. ····· 22

Figure 4. Schematic illustration showing synthesis of C-PAVIm. ····· 26

Figure 5. ^{1}H-NMR spectra of (a) PVIm; (b) Allyl bromide; (c) PAVIm. ···· 28

Figure 6. FT-IR spectra of PAVIm and C-PAVIm. ····· 30

Figure 7. Gel contents of C-PAVIm 0–C-PAVIm 3. ····· 32

Figure 8. DSC curves of PAVIm and C-PAVIm 0–C-PAVIm 3. ····· 34

Figure 9. TGA curves of (a) C-PAVIm 0–C-PAVIm 3; (b) Final weight based on TGA. ····· 36

Figure 10. SEM images showing cross-section of electrode: PVDF (a) Before and (b) After 20th cycles; C-PAVIm 1 (c) Before and (d) After 20th cycles at 1.0C. ····· 38

Figure 11. XPS spectra for before cycling and after 20th cycles: (a) PVDF C1s; (b) C-PAVIm 1 C1s; (c) PVDF O1s; (d) C-PAVIm 1 O1s. ····· 40

Figure 12. Schematic illustration showing Li-ion conduction of PVDF and C-PAVIm in Si electrodes. ····· 41

Figure 13. (a) Charge-discharge profiles during first cycle for Si-graphite composite anodes with C-PAVIm as a binder; (b) Cycling performance of

Si-graphite composite anodes with C-PAVIm (red) and PVDF (navy) as binders and 1.0 M $LiPF_6$/EC:DEC electrolyte at 1C; (c) Rate capability performance of Si-graphite composite anodes with C-PAVIm and PVDF as binders and 1.0 M $LiPF_6$/EC:DEC electrolyte; (d) Electrochemical impedance spectra (EIS) profiles at 26 °C for charging cycles of PVDF after formation, PVDF 20^{th} cycles, C-PAVIm after formation and C-PAVIm after 20^{th} cycles. 43

[Ⅲ. Radical Scavenging and Robust Polymer Binder]

Figure 1. Schematic illustration showing preparation of binder using poly(acrylic acid) (PAA) and tannic acid (TAc). (a) Preparation of PAA and TAc solution; (b) Nano-sized Si particles and interaction between PAA and TAc; (c) PAA and TAc structure. ····· 51

Figure 2. FT-IR spectra of PAA, TAc, C-PAA/TAc (8:2), C-PAA/TAc (5:5), and C-PAA/TAc (2:8). ····· 53

Figure 3. Molecular structure of tannic acid (TAc). ····· 54

Figure 4. Cross-linked binder formed by condensation between PAA and TAc. ····· 55

Figure 5. Gel contents of C-PAA/TAc (8:2), C-PAA/TAc (5:5), C-PAA/TAc (2:8). ····· 57

Figure 6. DSC curves of C-PAA/TAc (8:2), C-PAA/TAc (5:5), C-PAA/TAc (2:8). ····· 59

Figure 7. TGA curves of (a) C-PAA/TAc (8:2), C-PAA/TAc (5:5), C-PAA/TAc (2:8); (b) Final weight based on TGA. ····· 61

Figure 8. (a) Absorption vs. TAc concentration; (b) DPPH radical scavenging activity of C-PAA/TAc. ····· 63

Figure 9. Reaction of antioxidant and DPPH free radical. ····· 64

Figure 10. (a) Schematic assembly illustration of Si ‖ Li half cell configuration; (b) Galvanostatic charge-discharge profiles for half cell by

controlling binder ratio of C-PAA/TAc; (c) Cycling performance of Si PAA, Si TAc and Si C-PAA/TAc at 0.5 C-rate; (d) Coulombic efficiency of cycling performance of Si PAA Si TAc and Si C-PAA/TAc; (e) Electrochemical impedance spectroscopy of Si PAA, Si TAc and C-PAA/TAc after 100 cycles. ····· 67

Figure 11. (a) Optical images of the tapes peeled from the Si PVDF, Si TAc, Si C-PAA/TAc, and Si PAA electrodes; (b) 180° peel-off test results of Si PVDF, Si TAc, Si C-PAA/TAc, and Si PAA electrodes EIS data of Si PAA, Si TAcand Si C-PAA/TAc; (c) The average peeling forces. ····· 70

Figure 12. Cross-sectional SEM images: (a) Si PAA electrode and (b) After 100 cycles; (c) Si C-PAA/TAc (5:5) electrode and (d) After 100 cycles. ·· 72

Figure 13. Electrochemical performances of the Si ‖ Li half-cell with a high mass loading (~1.1 mg cm^{-2}): (a) Galvanostatic charge-discharge profiles for half cell Si PAA and Si C-PAA/TAc (5:5); (b) Cycling performance of Si PAA and Si C-PAA/TAc at 0.5 C-rate. ····· 74

Figure 14. Cycling performance of Si C-PAA/TAc low (~ 0.35 mg cm^{-2}) and high (~1.1 mg cm^{-2}) loading at 0.5 C-rate. ····· 75

[Ⅳ. Cross-Linked Organic/Inorganic Polymer Binder]

Figure 1. Schematic illustration showing synthesis of C-PVIm_Si. ····· 83

Figure 2. Schematic illustration showing reaction of NiO@C-PVIm_Si. ····· 84

Figure 3. Schematic illustration showing metal surface reaction. ····· 84

Figure 4. ^{1}H-NMR spectra of (a) PVIm; (b) 3CPTES. ····· 86

Figure 5. ^{1}H-NMR spectra of PVIm_Si 50, PVIm_Si 70, PVIm_Si 100. ··· 87

Figure 6. FT-IR spectra of PVIm_Si 50, PVIm_Si 70, PVIm_Si 100. ····· 89

Figure 7. FT-IR spectra of C-PVIm_Si. a) C-PVIm_Si 50 (150 °C 1h); b) C-PVIm_Si 70 (150 °C 1h); c) C-PVIm_Si 100 (150 °C 1h); d) C-PVIm_Si 50 (150 °C 2h); e) C-PVIm_Si 70 (150 °C 2h); f) C-PVIm_Si 100 (150 °C 2h); g) C-PVIm_Si 50 (160 °C 1h); h) C-PVIm_Si 70 (160 °C 1h); i) C-PVIm_Si 100 (160 °C 1h). ····· 90

Figure 8. FT-IR spectra of NiO@C-PVIm_Si. ····· 91

Figure 9. Schematic illustration showing silanol reaction. ····· 95

Figure 10. Gel contents of C-PVIm_Si 50, C-PVIm_Si 70, C-PVIm_Si 100. 96

Figure 11. TGA curves of (a) C-PVIm_Si 50, C-PVIm_Si 70, C-PVIm_Si 100; (b) Final weight based on TGA. ····· 98

Figure 12. TGA curves of (a) NiO@C-PVIm_Si; (b) Final weight based on TGA. ····· 99

Figure 13. (a) The 180° peeling tests for the Ni electrode with different binders; (b) The optical images of the tape and electrode surface after the peel test. ····· 101

Figure 14. SEM images showing of (a) $Ni(OH)_2$; (b) NiO. ····· 103

Figure 15. SEM image, energy dispersive X-ray (EDX) elemental mapping of (a)–(e) $Ni(OH)_2$. ····· 104

Figure 15. SEM image, energy dispersive X-ray (EDX) elemental mapping of (f)–(j) NiO. ····· 105

Figure 16. XRD patterns of $Ni(OH)_2$ and NiO. ····· 106

Figure 17. Schematic illustration of working electrode. ····· 108

Figure 18. Cyclic voltammogram curve of (a) Cycle test; (b) PVDF; (c) PVIm_Si 100; (d) C-PVIm_Si 100. ····· 109

Figure 19. EIS spectra of the device showing the internal resistances NiO@PVDF and NiO@C-PVIm_Si 100. ····· 110

ABSTRACT

전기화학적 성능 향상을 위한 이온전도성 및 견고한 구조의 기능성 에너지 재료

Park, Hui Gyeong
Advisor : Prof. Lee, Jung-Soo, Ph.D.
Department of Chemical Engineering,
Graduate School of Chosun University

환경오염과 지구 온난화는 현대 사회의 심각한 문제로 자리 잡고 있다. 화석 연료의 소비를 줄이고 환경오염을 완화하기 위해 깨끗하고 지속 가능한 에너지 시스템의 개발은 전 세계적으로 중요한 전략 중 하나이다. 화학 에너지와 전기 에너지 사이의 높은 변환 효율로 인해 이차전지, 연료 전지 및 슈퍼커패시터와 같은 전기화학 에너지 저장 장치가 많은 주목을 받고 있다. 그중 유망한 후보로 꼽히고 있는 리튬이온 배터리와 슈퍼커패시터는 전 세계적으로 놀라운 속도로 개발되어 휴대용 전자 기기를 넘어 전기자동차, 선박, 중장비 등 다양하게 적용되고 있다. 현재 높은 에너지 밀도 및 고속 충·방전이 가능한 에너지 저장 장치 개발에 대한 요구가 높아지고 있는 추세이다. 따라서, 더 높은 용량을 나타내는 새로운 전극 재료 탐색이 본질적으로 중요하다.

에너지 저장 시스템의 전극은 활물질, 도전재, 바인더로 구성된다. 바인더는 소량으로 사용되지만, 에너지 저장 장치의 전극 사이에 상호 연결성과 접착력을 제공하기 때문에 전극의 필수 구성요소이며 사이클 안정성에 매우 중요한 역할을 한다.

본 연구에서는 가교 반응을 통해 견고한 구조를 갖는 기능성 고분자 바인더를 제작하였다. 제작된 기능성 바인더는 화학 구조의 물리적 안정성과 향상된 접착 성능을 제공하였으며 반복되는 충·방전 과정 동안 우수한 내구성과 전기화학적 특성을 나타

내었다. 본 연구의 기능성 고분자 바인더는 현재 사용되는 상용 바인더보다 안정하고 우수한 성능을 보여주었다. 본 연구 결과는 소재 연구 개발의 중심이 될 것으로 기대된다.

Keywords: energy storage devices, lithium-ion batteries, supercapacitor, functional polymeric binder, cross-linking

Ⅰ. Introduction

A. Background of Study

As technology advances, modern society demands the development of high-efficiency, high-density, and long-life energy storage devices ranging from portable electronic devices to electric vehicles [1]. Energy has been generated based on fossil fuels for decades until today, but fossil fuels have turned the history of civilization upside down by efficiently providing unprecedented amounts of energy to mankind. Fossil fuels have a strong storage capacity, a large amount of calories, and a wide range of uses, so they played a key role in modern human history, including the industrial revolution. However, fossil fuels are gradually being depleted, causing serious environmental problems such as global warming [2]. Therefore, as a more fundamental solution along with the efficient use of fossil fuels, the development of a sustainable energy storage system (ESS) is one of the most important strategies worldwide to reduce the consumption of fossil fuels and alleviate environmental pollution [3, 4].

ESS is an energy solution that can store the produced electrical energy and use it when power is needed. In addition, research is in progress, focusing on improving differentiation with high energy density, low price, and miniaturization.

The necessity of ESS is increasing in terms of efficient power utilization, high-quality power, and stable power supply. ESS must be externally exchanged with the outside through electrical energy, and the Power Conversion System (PCS) is supplied with power and converts it into a specific form for discharge when necessary [5]. ESS is a physical method such as positive power or compressive air, a chemical method such as lithium-ion batteries (LIBs) or sodium sulfur batteries (NaS), or an electromagnetic method such as supercapacitors or superconducting magnetic energy storage (SMES) stored in the same electromagnetic way [6−9].

Various ESSs are selectively used according to the surrounding environment and purpose of use. Among these ESSs, the electrochemical storage device and the electrical storage device are considered the most popular technologies because they show superior performance compared to other storage devices and are less restricted by the

environment.

Among storage devices, LIBs and supercapacitors receive the most attention; this research focused on them.

B. Background of Experimental

1. Energy Storage Device

a. Lithium Ion Battery (LIBs)

LIBs are a type of secondary battery that moves lithium ions during charging and discharging to produce electricity and can be charged through an electrochemical redox reaction (Figure 1). It is used in portable electronic devices such as laptops and smart phones because of its light weight and high density compared to conventional batteries; it is not affected by the memory effect and has low power loss [10]. In addition, it is a representative technology of the Fourth Industrial Revolution that can be applied to various applications based on the design of packs and modularized products and applied to wearable devices through miniaturization.

Recently, the supply of electric vehicles has been replacing internal combustion locomotives in order to reduce greenhouse gas emissions in response to climate change [11-15]. Unfortunately, LIBs have not yet improved their energy density and cycling performance compared to conventional internal combustion engines. To solve these problems, the search for new electrode materials with higher capacity is intrinsically important [16]. This is because the electrochemical properties of LIBs are highly dependent on material, structure, and design [17]. The LIBs market is growing steadily, centered on energy storage devices that enable efficient storage.

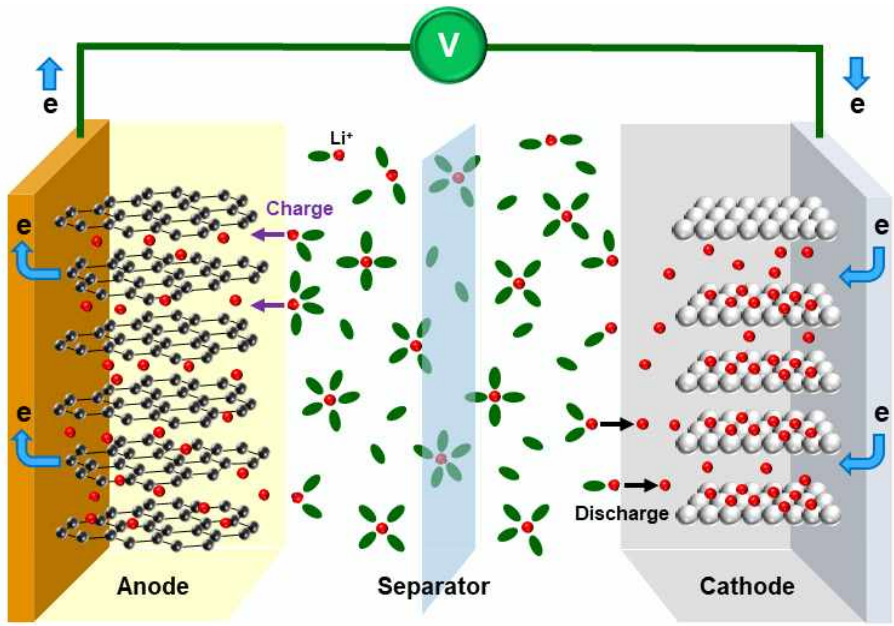

Figure 1. Operation of LIBs.

b. Supercapacitor

Supercapacitors are characterized by high charging and discharging speeds, a very long cycle life, and semi-permanent power density [18]. A capacitor is a device that can store electrical energy, store a large amount of energy, and produce a high output. Therefore, it is expected to be the most suitable storage device for electric vehicles, renewable energy generation, and smart grid fields. With the development of IoT electronic devices and the 4th industrial revolution approaching, various power supply products can be applied to our lives, attracting attention as a new energy storage device.

Supercapacitors can be divided into electric double-layer supercapacitors (EDLC) and pseudocapacitors (PSEUDO) according to the charge storage mechanism (Figure 2). Supercapacitors with ion adsorption or desorption are called EDLC, and those with surface chemical reactions are called PSEUDO. There is also a hybrid supercapacitor that appropriately mixes these characteristics [19].

PSEUDO can store more electrons than EDLC, which simply charges without oxidation-reduction (redox) reactions and shows a capacity increase of more than 100 times [20−22]. As development that can store and increase output energy while maintaining cycle characteristics is a major trend, it is expected that PSEUDO's continuous research and development (R&D) as an industry group will open up new opportunities.

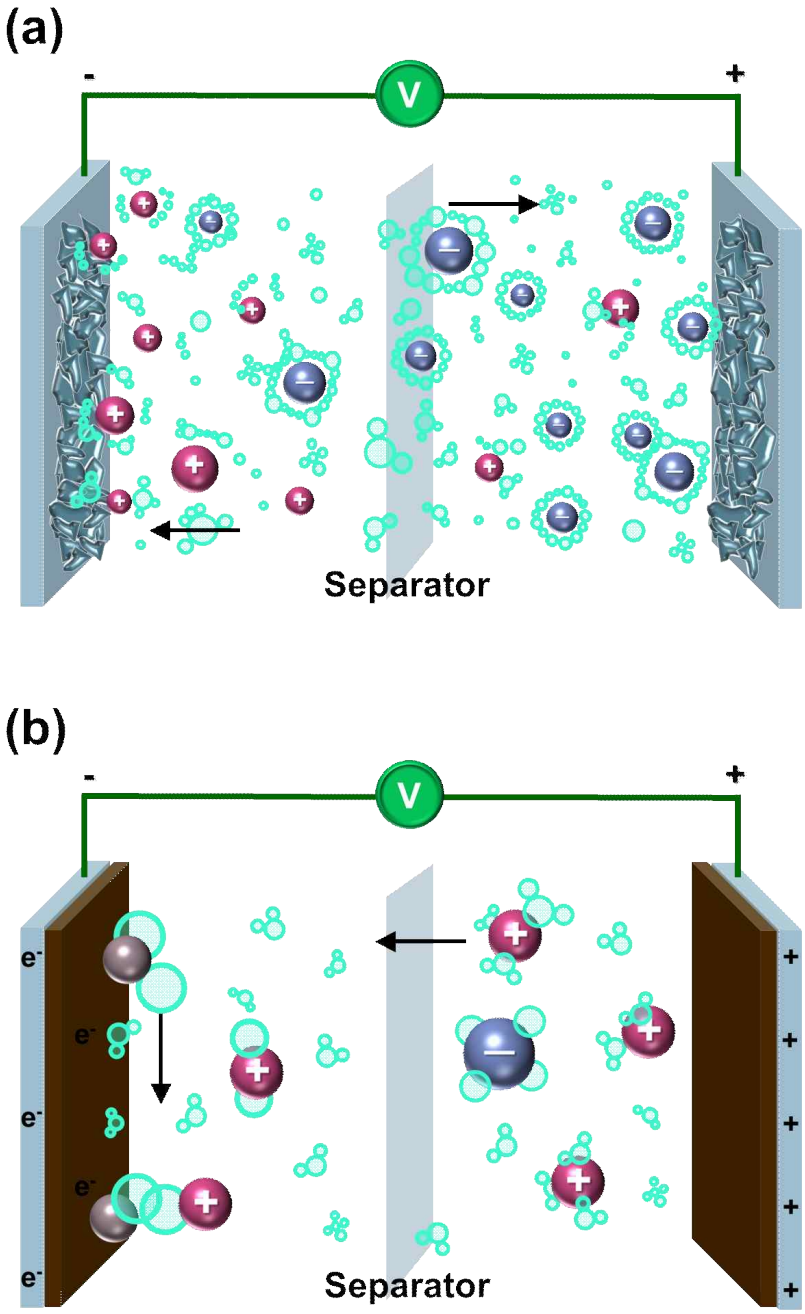

Figure 2. Operation of supercapacitor (a) EDLC, (b) PSEUDO.

2. Electrode Configuration

a. Cathode

The cathode, one part of the electrode, requires a high-voltage cathode material because the stored energy is proportional to the cell's operating voltage [23]. The cathode material is composed of a combination of lithium and metal components, and the density of the battery varies depending on the ratio of this combination [24].

Metal oxide series cathode materials include lithium cobalt oxide (LCO; $LiCoO_2$) with a layered structure, lithium manganese oxide (LMO; $LiMn_2O_4$) with a spinel structure, and lithium iron phosphate (LFP; $LiFePO_4$) with an olivine structure [25−28]. The characteristics of each material are shown in Figure 3. There are lithium nickel manganese cobalt oxides (NCM; $LiNiCoMnO_2$) and lithium nickel cobalt aluminum oxides (NCA; $LiNiCoAlO_2$), etc. LCO, which is advantageous in charging and synthesis, is used as a cathode material for small batteries. In addition, NCM and NCA, which have excellent instantaneous power and lifespan, are used as materials for medium- and large-sized batteries [29].

LCO, which has a layered structure, is a typical cathode material for LIBs due to its high energy output. It has the advantage of being stable and easy to manufacture in the atmosphere. However, the usable capacity is low, and cobalt raw materials are difficult to supply, so recycling research is in progress to extract cobalt from waste batteries [30].

LMO, having a spinel structure, is cheaper than LCO, but it has the disadvantage of being thermochemically unstable [31].

Although LFP with an olivine structure has excellent structural stability, a high lifespan, and is inexpensive, However, it has the disadvantage that the ion diffusion rate is slow during charging [32].

NCM is a cathode material with manganese added to nickel and cobalt [33]. NCA is a cathode material made by adding aluminum to nickel and cobalt [34].

NCM and NCA, which require advanced technology, are conducting additional research on stability to secure cost competitiveness.

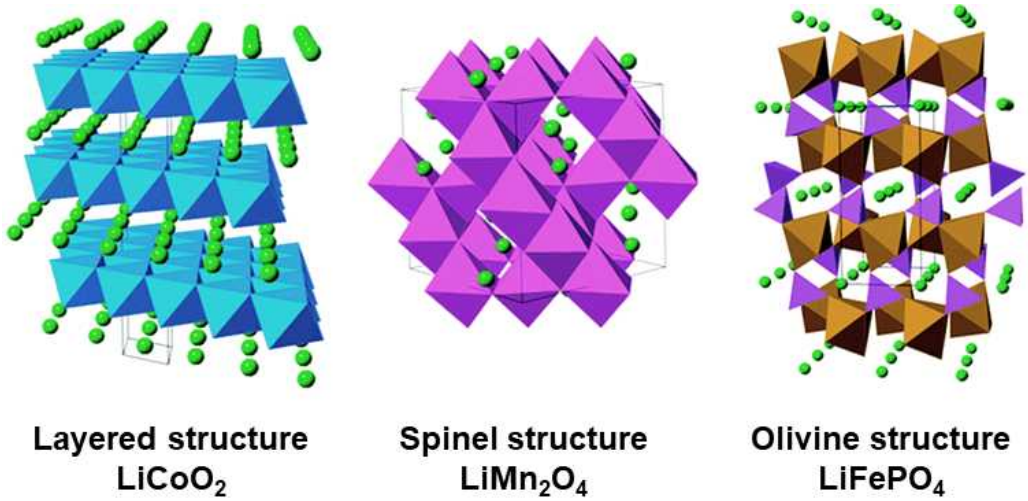

Figure 3. Representative crystal structures of cathode materials for LIBs [29].

b. Anode

The anode absorbs and releases lithium ions from the cathode to allow current to flow. Therefore, it must be thermally and mechanically stable and be able to store Li-ions well.

Graphite, which has low electrochemical reactivity, structural stability, and low cost, is usually used as the anode material. Graphite has a layered structure, which facilitates the movement of lithium ions [35, 36]. However, the lifespan is reduced due to the volume change caused by repeated cycles. Therefore, carbon-based materials are being studied.

Carbon-based materials include graphene, carbon nanotubes (CNT), fullerenes, etc. [37]. Carbon-based anode materials have been used in commercial Li-ion cells since 1991 because of their good electrochemical properties, low cost, and nontoxicity [38]. But since there is a limit to the capacity, metal oxides are being studied in addition to carbon-based materials, as shown in Figure 4.

In general, metal oxides have not received much attention because of their poor conductivity. However, an appropriate nano-sized metal oxide shows promising properties as a cathode material for batteries [39].

Metal oxides currently being studied include Zn, Ti, Si, Ge, Sn, Mn, Fe, Ru, Ni, and Co, etc. Among them, Si, which has about 10 times higher energy density than graphite, is also attracting attention as a next-generation anode material [40]. Si can provide specific capacities through an alloying-dealloying mechanism with Li [41]. However, there are problems to overcome with volume expansion, low efficiency, and a short lifespan (Figure 5). By changing the appropriate binder material and adding electrolyte solution, the volume expansion and lifespan problems of Si are being addressed.

As such, various metal oxides other than carbon are being studied. In addition, various studies are being conducted so that it can have better capacity and cycle stability than conventional carbon anodes and metal oxides by combining metal oxide and carbon or utilizing a core/shell structure (Figure 6).

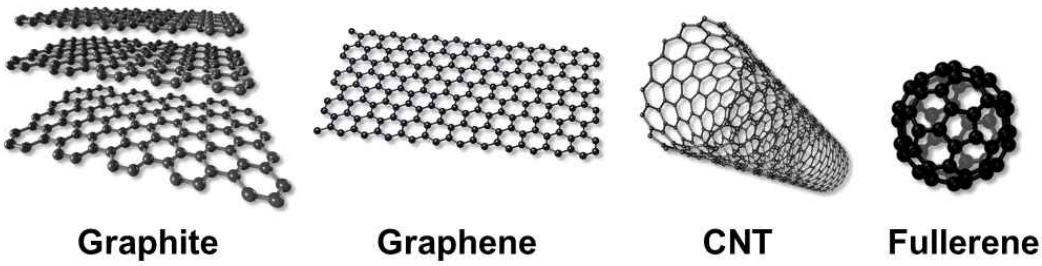

Figure 4. Carbon-based anode materials.

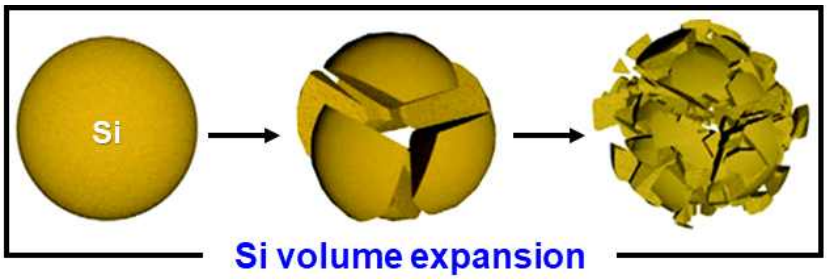

Figure 5. Challenges of Si-based anodes in LIBs.

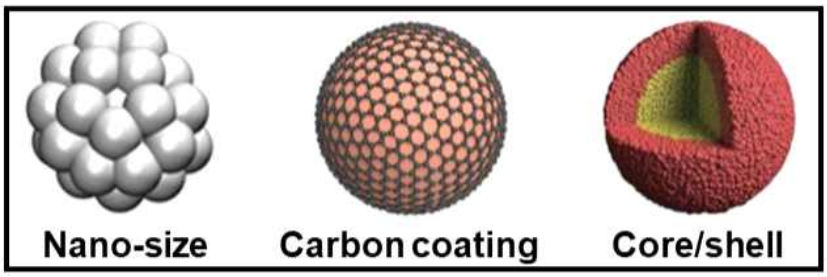

Figure 6. Progress of nanostructured metal oxides.

c. Electrolyte

In the battery, electrons move through the wire and Li-ions move through the electrolyte. The electrolyte requires low chemical reactivity and high ion conductivity to promote ion transport and must be able to withstand a voltage range without being easily decomposed. Electrolytes are classified into liquid electrolytes composed of organic solvents, solid state electrolytes, and ionic liquid (IL) electrolytes, etc. [42–46].

The liquid electrolyte is a state in which Li salts ($LiPF_6$, $LiClO_4$, $LiBF_4$, LiTFSI, etc.) are dissolved in an organic solvent (DMC; Dimethyl carbonate; DEC; Diethyl carbonate; EC; Ethylene carbonate, etc.). [47]. Liquid electrolytes have high ionic conductivity and excellent low-temperature characteristics, but there are temperature restrictions, so studies on electrolyte additives are being conducted for solid-state electrolytes with excellent high-temperature stability and efficiency of storage devices.

Solid state electrolytes have no issues of leakages of toxic organic solvents, easy to process, and have excellent thermal stability. Unfortunately, highly low ion conductivity limits their use.

Finally, ILs, which are receiving much attention as a material to replace the existing electrolyte, have favorable physical properties such as negligible vapor pressure, high ion conductivity, chemical inertness, and broad electrochemical stability. ILs have been extensively studied for use as electrolytes. However, since the current density is low when the ILs are used alone as an electrolyte, research on using the ionic liquid as an additive is also in progress.

d. Binder

An electrode is fabricated by the active electrode materials, the conductive agent, and the binder on the current collector [48–50]. The binder adheres and holds the active materials and conductive agent close to the current collector (Figure 7). Binders have received comparatively little attention, although recent reviews have begun to highlight their importance, especially in high-capacity battery systems [51]. While they only make up a small portion (such binder material whose weight is less than 2-5% of the electrode mass) of the electrode material, binder is crucial in determining the function of the battery, especially for their cycle performance. First, they help to disperse the other components in solvent during the fabrication process. Second, they hold together the various components of energy storage devices [52, 53].

With all the roles binders play in an electrode, there are many different properties that are desirable in a good binder. The main characteristics required of the electrode binder can be represented as shown in Figure 8. Even after the electrolyte environment or long-term electrochemical evaluation, the initial adhesive force should be able to be maintained significantly. The solubility of the solvent should also be appropriately high to effectively produce the electrode slurry. In addition, the ability to reversibly buffer the unavoidable volume changes of the active material and to inhibit the degeneration of the interfaces during battery operation is also a requisite.

Poly (vinylidene fluoride) (PVDF) has been widely used as an organic solvent-soluble binder in commercial batteries. PVDF has good electrochemical stability and adhesion to conventional electrodes and electrolytes. However, PVDF cannot afford sufficient binding to high-capacity anode particles that exhibit huge volume changes, and the usage of N-methyl pyrrolidone (NMP) is undesirable and not friendly to the environment [54–57]. In addition, the deadliest disadvantages of PVDF binder are its insulating character and a relatively large amount of electrolyte swelling. As a result, a passivation layer known as solid electrolyte interphase (SEI) was formed on the surface of electrodes from electrolyte decomposition products [58, 59]. The most problematic disadvantage was that SEI layer formation and growth led to capacity fading, increased

battery resistance, and reduced power density [60]. To overcome these disadvantages, a new design of the binder is urgently required.

In recent studies, several water-soluble polymer binder materials, such as carboxymethyl cellulose (CMC), polyvinyl alcohol (PVA), styrene-butadiene rubber (SBR), and polyacrylic acid (PAA), have been reported. Hydroxyl (-OH), carboxylic acid (-COOH), and amino ($-NH_2$) functional groups present in the polymer binder can effectively combine with the electrode surface [61, 62].

As mentioned earlier, binders have received relatively little attention. Since it has the potential to significantly improve performance when used in small amounts compared to other materials, we intend to conduct research on a new binder that can replace the existing PVDF binder.

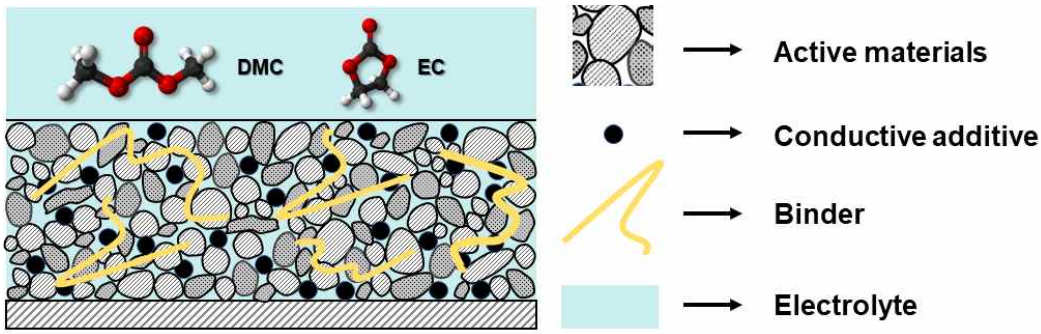

Figure 7. Schematic illustrations of electrode configuration.

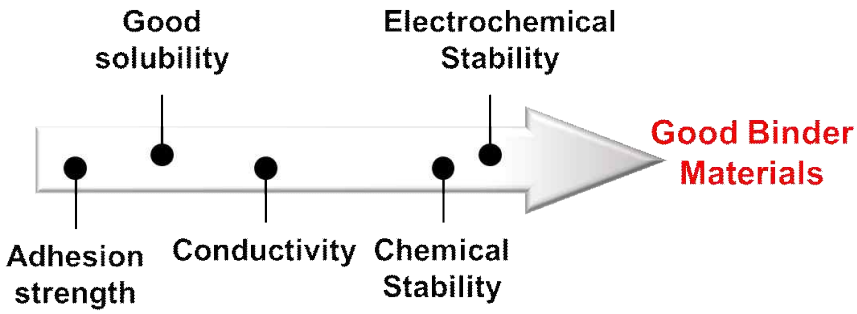

Figure 8. Binder requirement characteristics.

C. Ionic liquid

ILs are normally defined as compounds completely composed of ions (anions and cations) with a melting point below 100 ºC [63, 64]. The first IL, ethyl ammonium nitrate, was reported in 1914 by Paul Walden, who at that time did not realize that ILs would become a major scientific field [65]. Actually, ILs as innovative fluids have received wide attention only during the past two decades. Multidisciplinary research on IL has emerged in various ways, including in chemistry, material science, chemical engineering, and environmental science. This indicates that more and more researchers are engaged in studying this exciting area.

ILs have emerged as a greener alternative to conventional organic solvents thanks to their low volatility and flammability and their wide liquid-state window. IL is tunable by an appropriate selection of constituent ions. That is, it can be variously transformed into a wide range of multiple structures. Among various ILs, the cations mainly used are imidazolium, pyridinium, etc. [66, 67]. In addition, there are various types of anion, such as TFSI, PF_6, and BF_4 [68, 69]. ILs exhibit various chemical and physical properties depending on the type of anion (Figure 9). Therefore, we can design combinations of ILs according to the purpose. In addition, ILs have high electrical stability, a wide electrochemical range, and excellent ionic conductivity, so they are also applied to catalyst, separation, membrane, and electrochemical fields [70, 71].

Poly(ionic liquid) (PILs) is a type of ILs monomer polymerization. PILs, like ILs, can be engineered with a wide range of physicochemical properties and rich chemical structures using a variety of IL monomers and backbones. Many of the favorable qualities of ILs, including thermal and chemical stability and ion conductivity, are preserved in PILs (Figure 10).

PIL dramatically changed the research scope of existing ionic polymers and polymer electrolytes. As a candidate material for solid electrolytes and binders, PIL is attracting a lot of attention in battery and fuel cell-related applications. Currently, PILs are being intensively researched for use in products including batteries, supercapacitors, fuel cells, and photovoltaic devices [72–81].

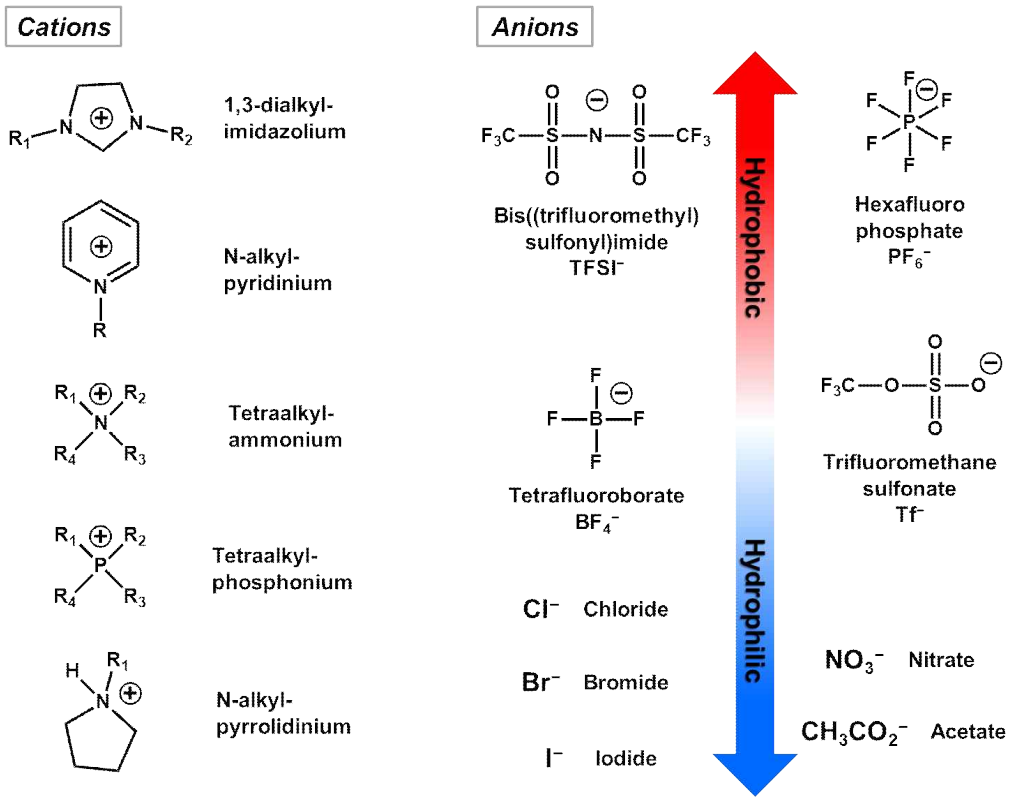

Figure 9. Typical cations and anions used in the formation of ILs.

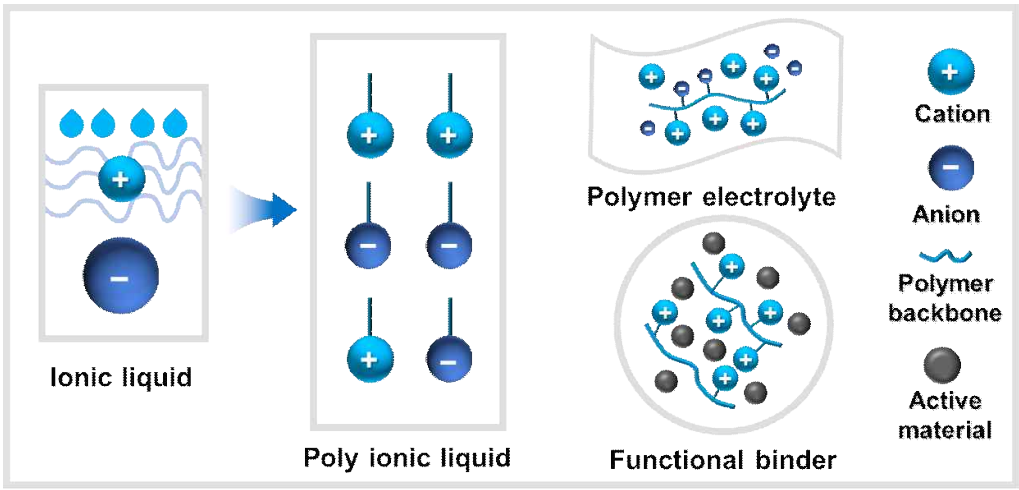

Figure 10. Advances on the use of PIL-based electrolytes and binders for LIBs.

D. Purpose of Research

Electrochemical energy storage systems, such as batteries and supercapacitors, play a crucial role together with renewable energy sources in creating a greener and more sustainable future. Batteries, though often used in small doses, play an important role. However, the role of binders was underestimated, and thus development of binders was not prioritized. PVDF has been widely used for its good chemical stability and adhesion. However, PVDF does not deliver satisfactory performance. A SEI layer is formed at the electrode interface, interfering with lithium ion transport. Also, PVDF cannot buffer a huge volume change. Due to these problems, PVDF alternatives have become a really important and essential topic. Herein, we intend to design a new binder to replace the PVDF binder.

ILs have attracted great attention as candidates for electrolytes and binders due to their remarkable characteristics such as low vapor pressure, electrochemical stability, and structural stability. When an IL is used as a binder, it is dissolved in an electrolyte, so polymerization is attempted to increase the physical properties of the ionic liquid. In other words, it is an attempt to produce a functional binder by synthesizing a PIL.

Biomass, a renewable resource that is continuously productive and replaces fossil fuels, is becoming increasingly interesting as a future energy resource that can respond to climate change. Tannic acid (TAc) derived from biomass was considered a si anode binder in this study. It was cross-linked with radical-scavenging activity, a unique ability of TAc and PAA to produce a functional binder with a robust structure.

Our binder is expected to overcome the shortcomings of PVDF, be used in various energy storage devices, and be the center of research and development of existing materials.

Ⅱ. Dual Effect-Assisted Polymer Binder of LIBs

A. Introduction

With the rapid advancement of energy storage systems, rechargeable battery systems with safe and long lifetime have been drawing attention over the several decades. Lithium-ion batteries (LIBs) are one of the most promising energy storage devices owing to their high energy and power density [1, 2]. High energy density and stability, it does not suffer from memory effects has low power loss, which is considered an important issue in the field of energy storage [3–8]. Although there are extensive studies on anodes, cathodes, electrolytes, separators, etc. to improve the efficiency of lithium batteries, there are still insufficient studies on polymer binders [9]. These binder materials account for 1 wt% of the electrode mass, they are adhesives that physically stabilize the active materials and conductive materials by fixing them to the electrode. Polymer binders can improve cycle performance and stability by interacting between electrolytes and active materials at interfaces. In addition, recent studies have shown that polymer binders improve the performance of electrochemical devices [10–15].

Polymer binders play multi important roles in battery performance. They act insolubility in the electrolyte, suitable adhesiveness, strong ion/electron conductivity.

In general, poly(vinylidene fluoride) (PVDF) hass been widely used representative polymer binder [16–18]. PVDF is routinely used in LIB for its adhesion, chemical inertness, and availability [19, 20]. However, the disadvantage of PVDF binders are its insulating character and a relatively large amount of electrolyte swelling. Moreover, when using PVDF as a binder, we observe lithium interruption that prevents the transport of lithium ions at the interface. As a result, a passivation layer called solid electrodes interphase (SEI) is formed on the surface of electrodes from electrolyte decomposition products [6, 21]. The most problematic disadvantage is that SEI layer formation and growth lead to capacity fading, increased battery resistance and reduced power density. To overcome these disadvantages, a new design of the binder is urgently required. In our opinion, if the newly designed binder participates in electrochemical reactions and is as stable as PVDF, will have a part to play resolve a

problem [1, 22].

Poly ionic liquids (PIL)s, which has recently attracted attention due to its high electrochemical stability, ion conductivity and excellent processability, it is very sustainable for electrochemical applications [23–27]. PILs were found to be a highly attractive class of functional polymers. Moreover, it is known to be highly stable for use as a LIB binder [28]. PIL can wrap powder components and improve cycle properties by allowing Li^+ to flow. During the cycle, PIL particles can penetrate between electrolyte free spaces and maintain contact between conductive components [29–31].

Cross-linking is an effective method to reduce crystallinity while substantially improving mechanical strength and thermal stability (Figure 1). Moreover, the cross-linked polymer binder can improve the binding force of components and minimize the effects of swelling and contraction when charging and discharging the electrode [32–36]. Therefore, the binder composition comprising such cross-linked polymer system can improve the capacity of LIBs [37, 38].

In summary, we designed this method to cross-link allyl groups to increase the length of the ion channel (Figure 2). The designed binder has ionic conductivity and robustness, and adequately controls the SEI layer due to electrolyte degradation during cycling. Accordingly, a multifunctional binder with improved cycle life and LIB performance was developed. In this paper, we introduce a non-traditional binder concept, “dual-effect assisted cross-linked binder” (Figure 3).

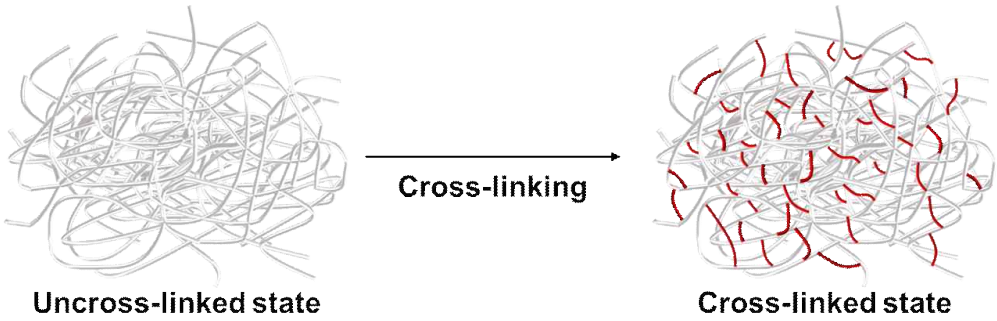

Figure 1. Description of uncross-linked and cross-linked rubber chains.

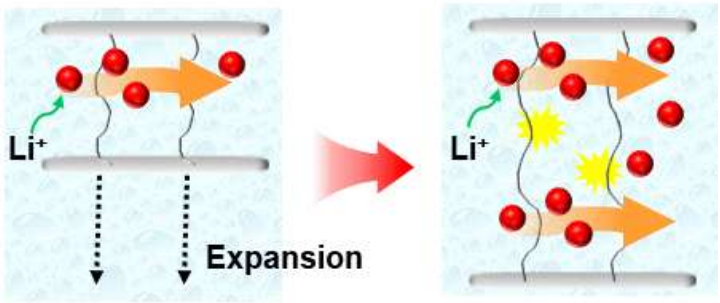

Figure 2. Illustration showing ion channel expansion of research concept.

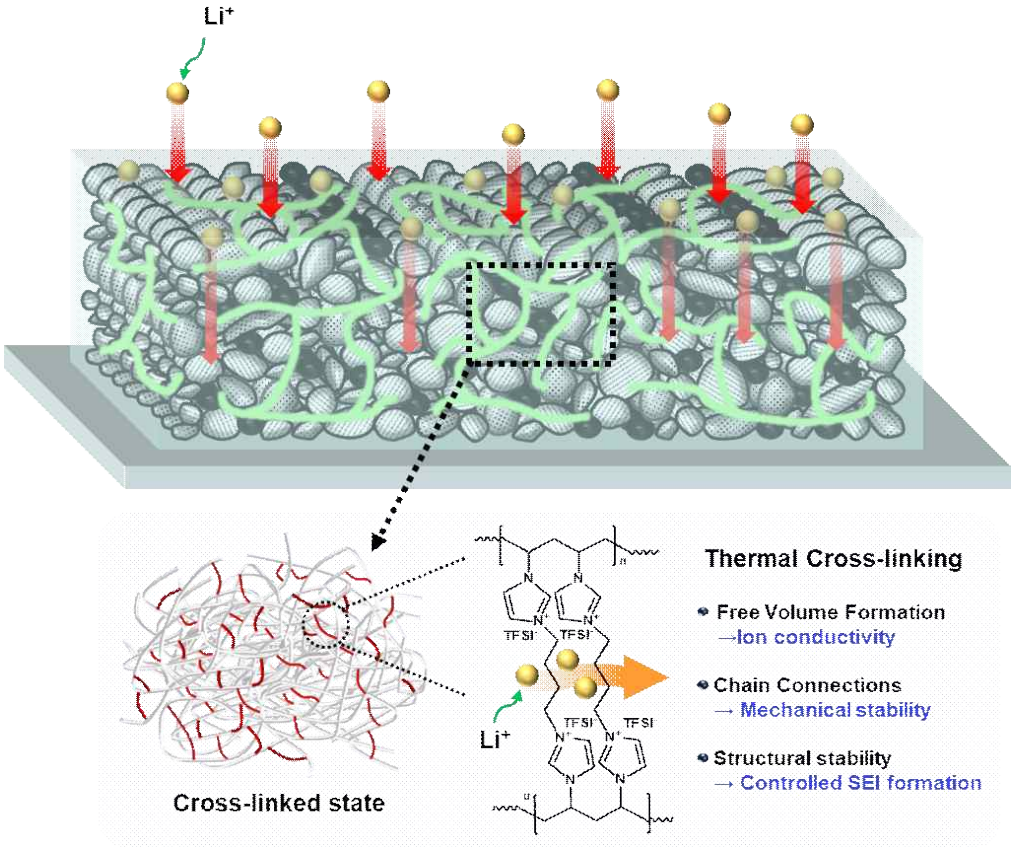

Figure 3. Illustration showing dual-effect binder.

B. Experimental

1. Materials

1-Vinylimidazole (Vm) (Alfa Aesar), allyl bromide (Sigma Aldrich), a,a'-azobisisobutyronitrile (AIBN) (JUNSEI), dimethylformamide (DMF) (JUNSEI), acetone (Duksan), methanol (MeOH) (Duksan), lithium bis(trifluoromethanesulfonyl)imide (LiTFSI) (Duksan) were used without any further purification. AIBN was recrystallized from MeOH.

2. Method

a. Synthesis of Poly(vinyl imidazole)

Vm, AIBN, and DMF were mixed together in a flask. The mixture was slowly heated to 70 °C under an inert atmosphere such as nitrogen. After, the mixture was reacted polymerization for 24 h via magnetic stirring. The resulting mixture was cooled to room temperature and precipitated using acetone. The resultant product was filtered and dissolved in acetone many time. The product was vacuum dried at 60 °C for overnight to obtain a white powder.

b. Quaternization of PVIm with Allyl bromide

PVIm, allyl bromide and MeOH were mixed together in a flask and allowed to react at 40 °C for 48 h under magnetic stirring. Next, the mixture was terminated, the mixture was precipitated with diethyl ether. Finally, the product was dried overnight in a vacuum oven at 40 °C, as shown in Figure 4.

c. Anion Exchange of Poly(N-allyl-vinyl imidazolium)·$TFSI^-$

An ion exchange reaction was performed to obtain PAVIm·Br^- and TFSI by solubilizing PAVIm·Br^- in distilled water, followed by the dropwise addition of an aqueous solution of LiTFSI. The mixture was then stirred at room temperature for 10 h. Finally, the precipitated powder was washed with distilled water in a aspirator and vacuum dried at room temperature for over night.

d. Thermal Cross-linked Poly(N-allyl-vinyl imidazolium)·$TFSI^-$

The prepared PAVIm·$TFSI^-$ film were placed in a vacuum oven at 100 °C for 1 h (C-PAVIm 0), 150 °C for 1 h (C-PAVIm 1) and 2 h (C-PAVIm 2), and 160 °C for 1 h (C-PAVIm 3) to cross-link them thermally.

3. Characterization

The chemical structures of the films were analyzed via Fourier-transform infrared spectrometry (FT-IR, Nicolet6700) and proton nuclear magnetic resonance (^{1}H-NMR, JEOL-JNM-AL300) in DMSO-d_6 at 300 MHz. The thermal properties of C-PAVIm were investigated using differential scanning calorimetry (DSC, TA Instruments DSC25) under a N_2 atmosphere (at a temperature range of 25 °C−180 °C and a heating rate of 5 °C min^{-1}) and via thermogravimetric analysis (TGA, TA Instruments SDT650) under a N_2 atmosphere (at a temperature range of 25 °C−1000 °C and a heating rate of 10 °C min^{-1}). To confirm the degree of chemical cross-linking, the gel content was determined using the solvent extraction method and calculated using the following equation:

$$\frac{M_2}{M_1} \times 100\% = \text{gel content},$$

where M_1 is the weight of C-PAVIm and M_2 is the weight of the extracted solvent [39].

Morphological and chemical characterizations of the electrode were conducted via scanning electron microscopy (SEM, Hitachi Regulus 8100) and X-ray photoelectron spectroscopy (XPS, Thermo Scientific, NEXSA) before and after the electrochemical cycle test.

4. Electrochemical Characterization

All electrodes, including the cross-linked binder (C-PAVIm) and PVDF (1100, Kureha Chemical Industry, Japan, 10 wt%), were manufactured base on the same composition ratio. The constituent materials were a Si−graphite composite as the active material,

C-PAVIm and PVDF as the binder and Super-P (Timcal Inc.) as the conductive material, in a mass ratio of 88:8:4. A binder solution comprising C-PAVIm and PVDF was adopted, along with 4 wt% of NMP solvent. The loading levels of all manufactured electrodes were approximately 3 mg cm^{-2}. We utilized 1.15 M $LiPF_6$ in ethylene carbonate (EC)/ethyl methyl carbonate/dimethyl carbonate (DEC) (at a ratio of 3:5:2 (v/v)) and microporous polyethylene as the electrolyte and separator, respectively. A 2032R coin cell assembled in an argon-filled glove box was used for all electrochemical tests. It was tested for charging/discharging at 0.05C (1C = 550 mA g^{-1}) for the formation cycle, 1.0C for the cycle life test and 0.2C, 0.5C, 1.0C, 3.0C and 5.0C for rate capability tests in the voltage range of 1.5 to 0 V at 26 Â °C. Charging was performed at a constant current mode. Electrochemical impedance spectroscopy (EIS, IVIUM) was conducted to confirm the impedance at a frequency range of 0.003−300 kHz and an amplitude of 1.5 V for the pristine samples and samples that underwent 20 charging cycles at 26 °C.

C. Results and Discussion

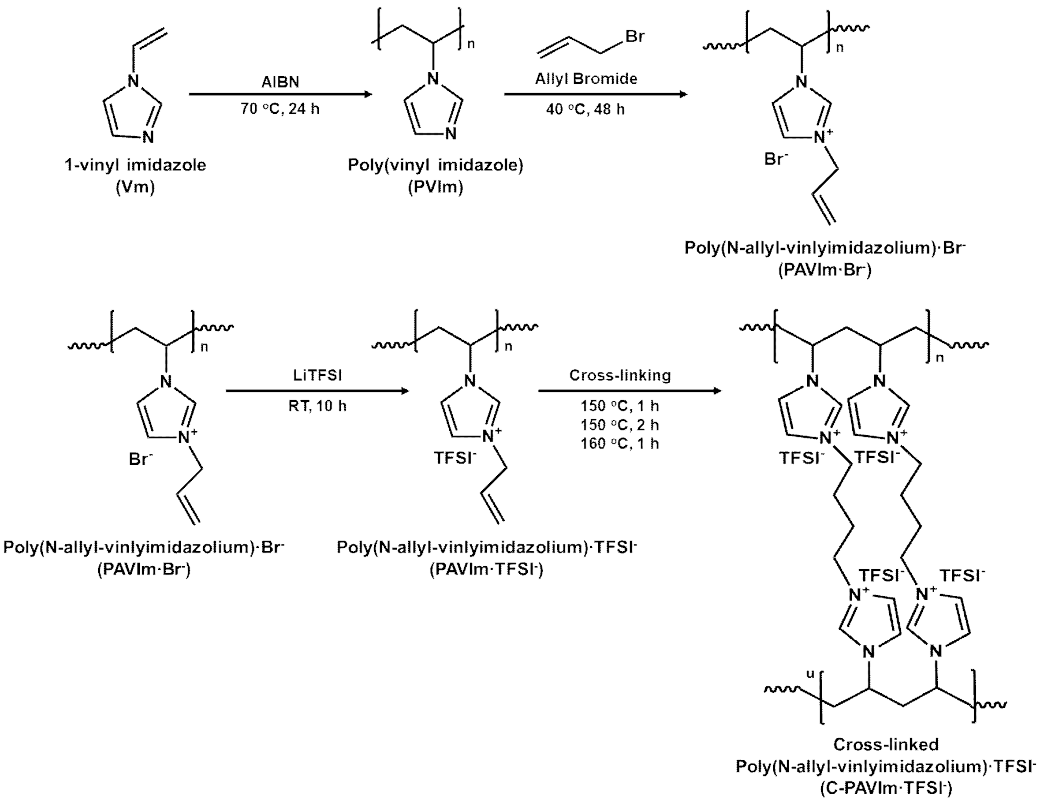

Figure 4. Schematic illustration showing synthesis of C-PAVIm.

1. ^{1}H-NMR Spectra

The structure of the as-synthesized PAVIm was identified by ^{1}H-NMR in DMSO-d_6. As show in Figure 5. (a), the signals at 1.6–2.2 ppm (Ha) 2.8–3.2 ppm (Hb) are ascribed to the backbone protons (CH_2 and CH-). This suggests the successful polymerization of vinyl group of 1-Vinyl imidazole. Likewise, the peaks at around 6.4–7.2 ppm are associated with the protons (Hc, Hd and He) on the imidazole ring. The well-defined peaks indicate that the polymerization proceeds smoothly. In Figure 5. (b), the NMR spectrum of allyl bromide shows specific peaks at 5–6.2 ppm (Ha, Hb) can be assigned to the protons on the allyl group of the allyl bromide. After the reaction between PVIm-allyl bromide and the quaternization of the resultant molecules to yield PAVIm, the proton resonance in imidazole ring (Hc, Hd, and He) shifted to 7.0–8.0 ppm, which are due to existence of allyl group at 5–6.2 ppm (Hf, Hg, Hh) in Figure 5. (c). ^{1}H-NMR spectra of PAVIm show that successful polymerization [40–42].

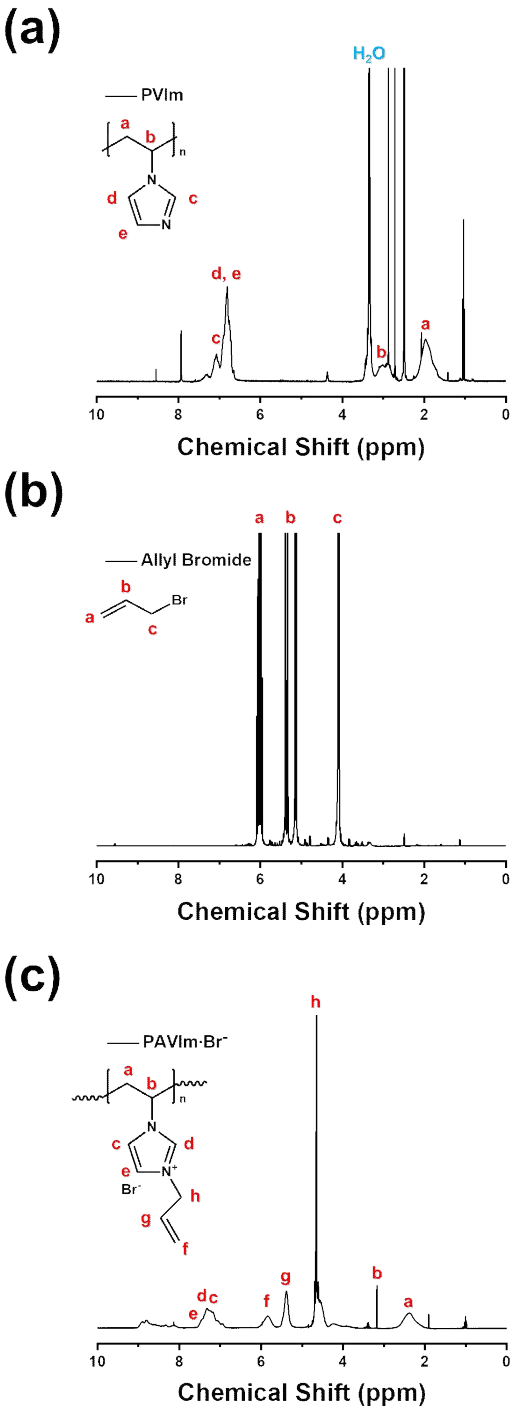

Figure 5. ^{1}H-NMR spectra of (a) PVIm; (b) Allyl bromide; (c) PAVIm.

2. FT-IR Spectra

FT-IR spectroscopy was used to characterize the cross-linking bond formation in the resulting C-PAVIm network, as shown in Figure 6. The peaks at 3100–3000 cm^{-1} are attributable to sp^2 -CH. And the spectra for sp^3 -CH have peak at 2950–2800 cm^{-1}. These are the peaks that can confirm the structure of PVIm [43]. The characteristic peaks at 1170 and 1126 cm^{-1} are attributed to the C-N asymmetric stretching freqency of the imidazole ring, whereas the peaks at 1750–1550 cm^{-1} are attributed to the -C=N stretching of the imidazole ring [44]. The two peaks at 992 and 944 cm^{-1} are attributed allylic -CH. In particular, the alkane of the allyl group decreased at peaks of 730–720 cm^{-1} as the temperature increased for the cross-linking. The ovserved degradation of aromatic amines in C-PAVIm 2 and C-PAVIm 3 due to decreased peak at 1335–1250 cm^{-1} [42, 45, 46]. Therefore, C-PAVIm 1 was considered the optimal condition.

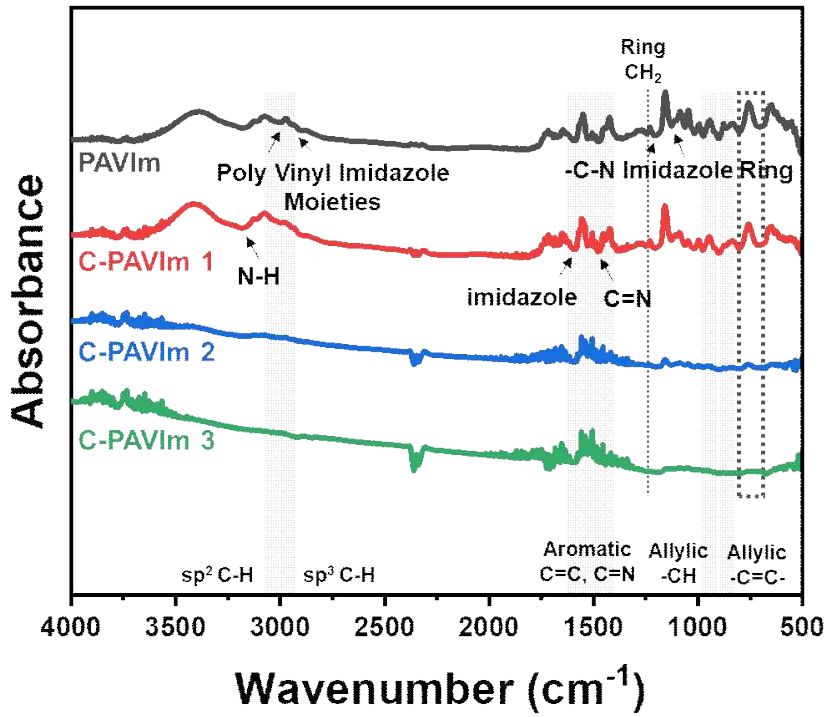

Figure 6. FT-IR spectra of PAVIm and C-PAVIm.

3. Gel Content Analysis

The gel content of C-PAIVM was measured at different temperatures during thermal treatment, as shown in FIgure 7. The C-PAVIm were prepared by thermal annealing cross-linking followed by PAVIm. The results of the analysis showed that the cross-linking was the highest when the thermal annealing cross-linking was performed at PAVIm 1 (68.9%). This result indicates that if the temperature and thermal annealing time are increased, the cross-linking is break off and the deterioration occurs in the polymer property. At conditions higher than 150 ℃ (C-PAVIm 1), the gel content decreased slightly owing to the collapse of the polymeric chemical structure, as confirmed via FT-IR analysis. The gel content increased with the thermal treatment temperature until C-PAVIm 1, above which it saturated.

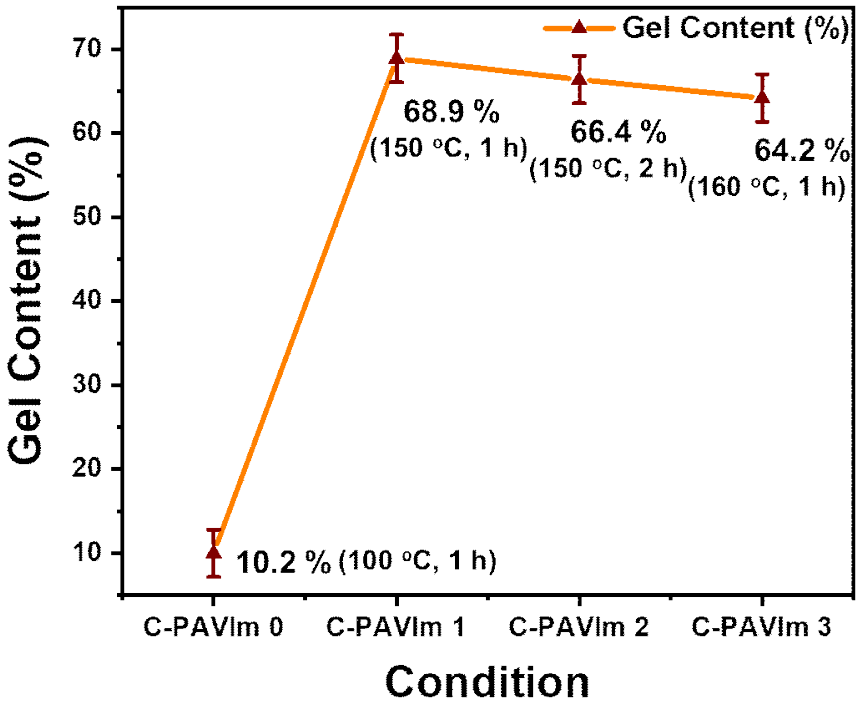

Figure 7. Gel contents of C-PAVIm 0–C-PAVIm 3.

4. DSC Curves

DSC refers to the thermal analytical techniques of heat flow through sample and response, and is measured as a function of temperature, i.e., a curve is drawn between the heat flow vs. the temperature. The thermal property of the C-PAVIm prepared via thermal treatment was analyzed using DSC. Figure 8 shows the plots of the derivative of heating scans as a function of temperature. The peak values indicate the Tg of PAVIm in the C-PAVIm for different compositions. The data show that glass transition temperature of the prepared samples increased with the cross-linking temperature. Through these results, it can be seen that thermal stability can be improved through thermal cross-linking.

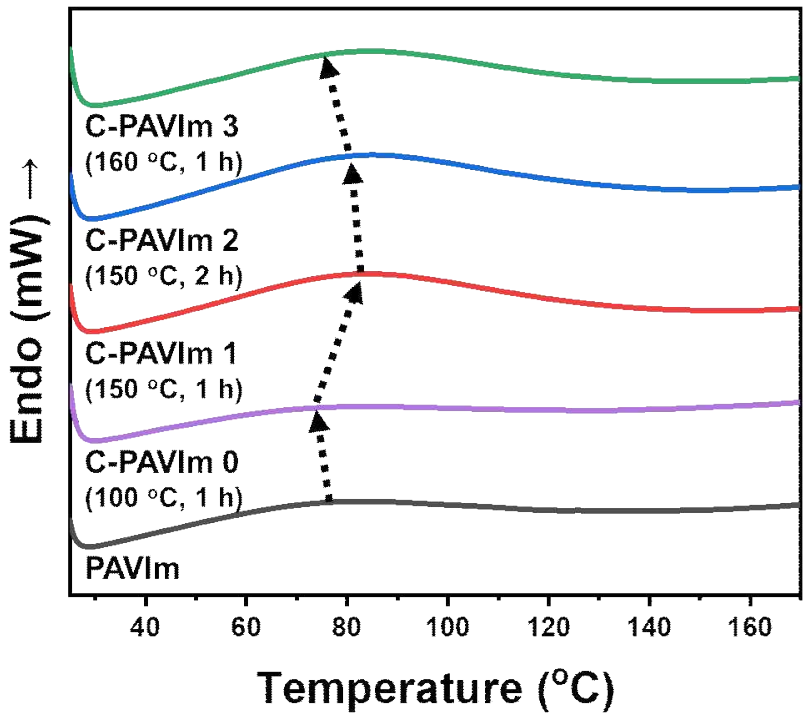

Figure 8. DSC curves of PAVIm and C-PAVIm 0–C-PAVIm 3.

5. TGA Curves

The TGA results are shown in Figure 9 a. All of the samples generally exhibit two thermal degradation patterns. The first slight weight loss (< 10%) below 300 °C can be attributed to the elimination of water in the C-PAVIm. The second degradation region, the onset decomposition temperature is above 480 °C, which is ascribed to the decomposition of imidazolium cross-linked main chain [47]. The second covering amount of C-PAVIm 0, C-PAVIm 1, C-PAVIm 2 and C-PAVIm 3 are 3.70, 8.45, 5.84, 4.94 wt%, respectively. The TGA results indicated that the final weight of C-PAVIm 1 was the highest. A critical observation shows a decrease in weight loss in C-PAVIm 1. The Figure 9 b shows the final weight when the temperature is raised from room temperature to 1000 °C.

Improved thermal stability of the C-PAVIm 1 binder was achieved. In fact, it is more thermally stable than other binders. The enhancement of cross-linking network is probably beneficial to the binder thermal stability.

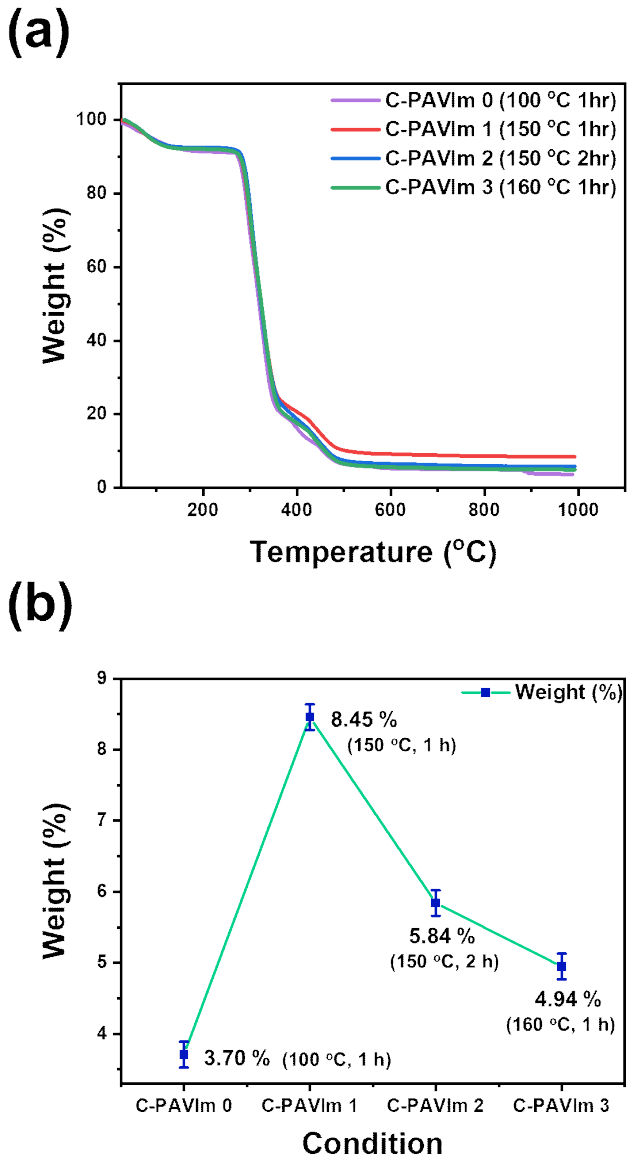

Figure 9. TGA curves of (a) C-PAVIm 0–C-PAVIm 3; (b) Final weight based on TGA.

6. SEM Images

The cross sectional morphological status of the anode electrodes was observed after 20 charge/discharge cycles via SEM and the results are shown Figure 10 [48].

Figure 10 a, b as shown, the PVDF-based electrode was clear swelling and a thick SEI layer. By contrast, the C-PAVIm 1-based electrode exhibited less swelling and a thinner SEI. Thus, the SEM images confirmed that the C-PAVIm 1 binder participated in the formation of the SEI layer owing to the degradation of the electrolyte and contributed positively to the cycling performance.

Our designed C-PAVIm shows that the ionic conductivity and robustness of the electrode improved owing to the formation of an appropriate SEI aleyr and thermal cross-linking. Meanwhile, PVDF formed a thick SEI laer, which inhibited ion conductivity and disintegrated the structure of the silicon nanoparticle. This finding verified the successful realization of our experimental design. The enhanced performance in the presence of silicon nanoparticles and C-PAVIm 1 can be explained based in the schematic illustration shown in Figure 10 c, d.

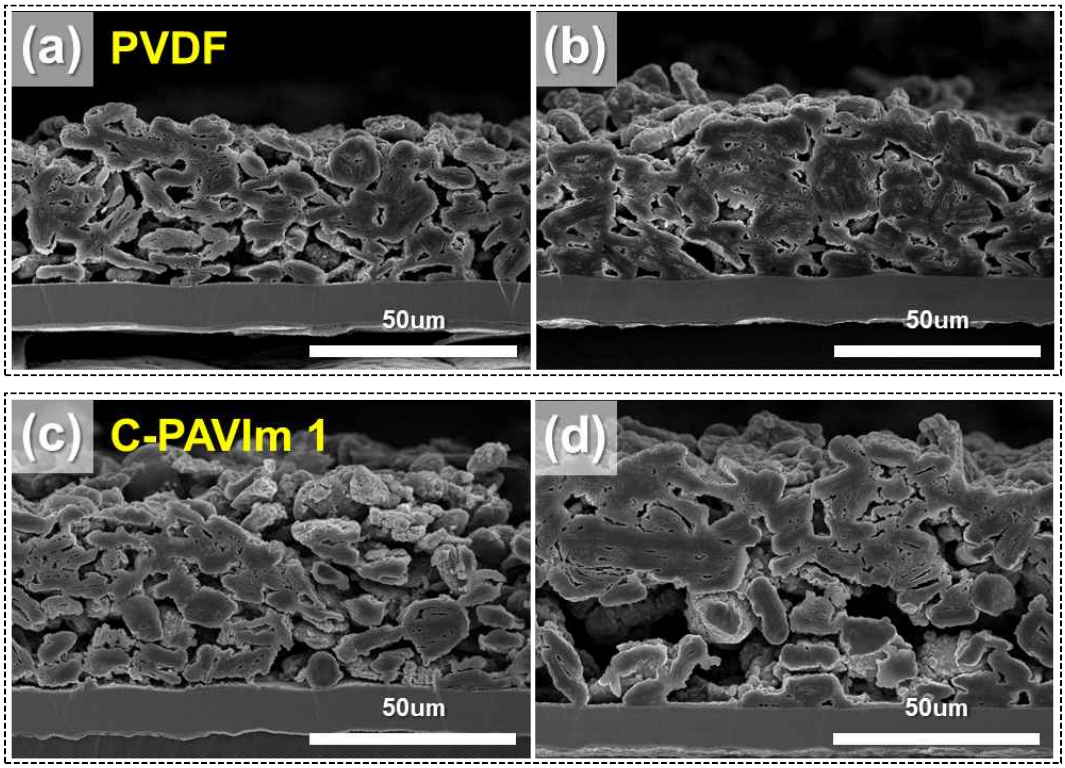

Figure 10. SEM images showing cross-section of electrode: PVDF (a) Before and (b) After 20th cycles; C-PAVIm 1 (c) Before and (d) After 20th cycles at 1.0C.

7. XPS Spectra

The surface composition of PVDF and C-PAVIm 1 were qualitatively probed using XPS as shown in FIgure 11. C1s and O1s can be found in the XPS spectrum of PVDF and C-PAVIm 1. The peak at approximately 289 eV was assigned to Li_2CO_3 and RO-COO. Li_2CO_3 and RO-COO have been widely reported as the main components of SEI layer formed on silicon. Based on the electrochemical reaction, the most likely principal component is Li_2CO_3, owing to the decomposition of the DMC electrolyte [49]. The relative intensities of the Li_2CO_3 and RO–COO peaks in the PVDF-based electrodes after 20 cycles were much higher than those of the C-PAVIm 1-based electrode (Figure 11 a, b). In addition, C=O and C-OH bonds were formed at 287 and 286 eV, respectively [50–55]. Therefore, the stable cycling performance and SEI layer formation are attributable to the C-PAVIm of the cross-linked network and ionic conductivity on the surface of the si nanoparticles.

XPS was performed on the si electrodes before cycling; after 20 cycles, as shown in Figures 11 c and d, C=O and O-C=O were shown. This is believed to be due to oxidation occurring in the manufacturing and storage process of PVDF, C-PAVIm 1 binder.

The enhanced performance in the presence of silicon nanoparticles and C-PAVIm 1 can be explained based on the schematic illustration shown in Figure 12. Our designed C-PAVIm shows that the ionic conductivity and robustness of the electrode improved owing to the formation of an appropriate SEI layer and thermal cross-linking. Meanwhile, PVDF formed a thick SEI layer, which inhibited ion conductivity and disintegrated the structure of the silicon nanoparticles. Hence, we focused on multifunctional binder designs that can enhance lithium-ion transport by supporting the formation of a conductive SEI, thereby affording a longer cycle life and improved overall LIB performance.

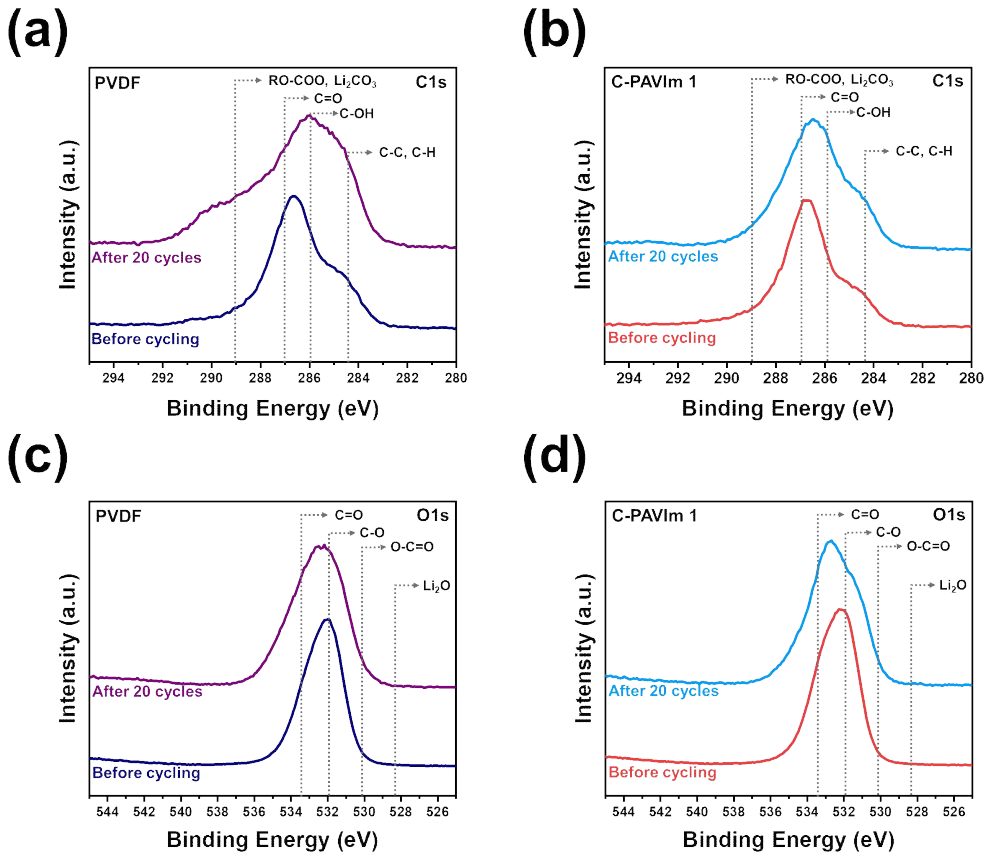

Figure 11. XPS spectra for before cycling and after 20th cycles: (a) PVDF C1s; (b) C-PAVIm 1 C1s; (c) PVDF O1s; (d) C-PAVIm 1 O1s.

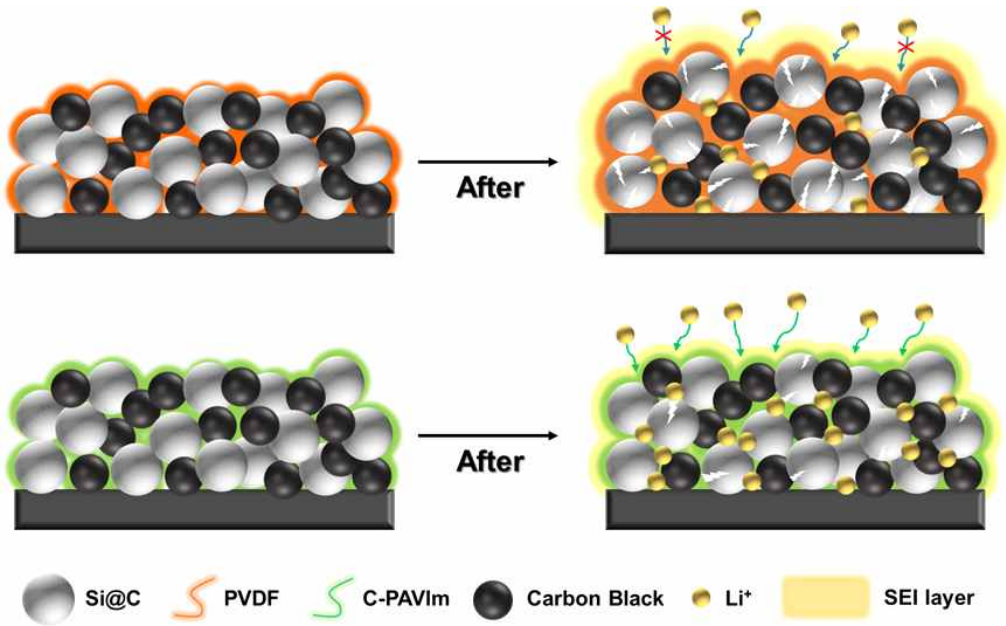

Figure 12. Schematic illustration showing Li-ion conduction of PVDF and C-PAVIm in Si electrodes.

8. Electrochemical Analysis

Figure 13 a shows the charge-discharge profile for the C-PAVIm-based electrode. In the first cycle observed at approximately 0.7 V, an irreversible reactions taking place lead to the formation of SEI. The C-PAVIm electrode demonstrated superior discharge and charge capacity of 610 and 520 mAh g^{-1}.

The C-PAVIm electrode exhibited a higher discharge capacity than the PVDF-based electrode during the cycling life test (Figure 13 b). After cycles, the C-PAVIm and PVDF electrodes indicated saturated capacity of 190 and 105 mAh g^{-1}, respectively. This implied that the C-PAVIm electrode offers a more efficient transfer of Li even after ling charge/discharge cycles.

Figure 13 c shows the rate capabilities of the electrodes composed of C-PAVIm and PVDF were verified up to 5.0C. Based on the rate capability, we believe that the low Li-ion diffusivity of the PVDF electrode resulted in inferior electrical power properties, as compared with the C-PAVIm electrode.

It is evident that the C-PAVIm electrode significantly outperform that with the PVDF binder.

The EIS for the corresponding to C-PAVIm and PVDF after the formation and 20^{th} cycles shown in Figure 13 d. The interfacial resistance post cycling for the C-PAVIm-based electrode was less than half the value for the PVDF-based electrode. Also, it can be noted that the resistance corresponding to the diffusion of the of Li-ion into the active material was drastically reduced for C-PAVIm1-based electrode after cycling. These EIS results are consistent with the other electrochemical results presented above. Furthermore, the solution resistance of the PVDF electrode increased significantly after the 20^{th} cycle, whereas that of the C-PAVIm electrode remained the same. This implies that the PVDF electrode exhausted the electrolyte continuously during the cycling test owing to the unstable interface between the active materials and electrolyte [56-60].

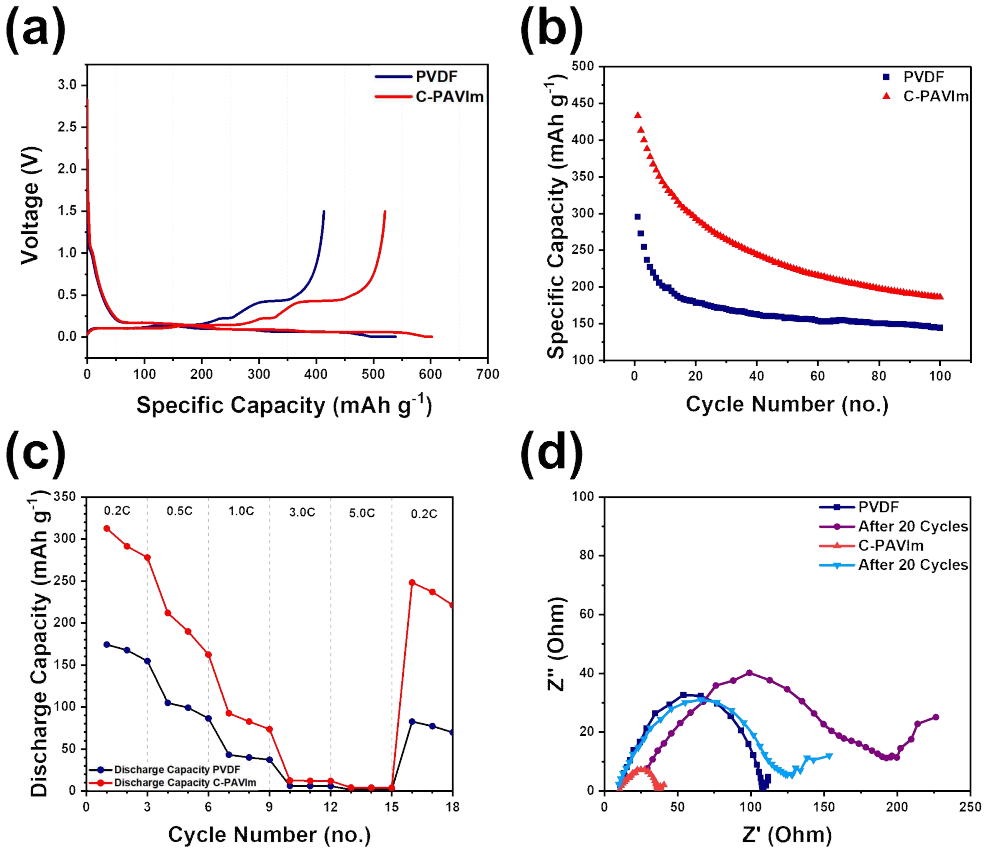

Figure 13. (a) Charge-discharge profiles during first cycle for Si-graphite composite anodes with C-PAVIm as a binder; (b) Cycling performance of Si-graphite composite anodes with C-PAVIm (red) and PVDF (navy) as binders and 1.0 M $LiPF_6$/EC:DEC electrolyte at 1C; (c) Rate capability performance of Si-graphite composite anodes with C-PAVIm and PVDF as binders and 1.0 M $LiPF_6$/EC:DEC electrolyte; (d) Electrochemical impedance spectra (EIS) profiles at 26 ^{o}C for charging cycles of PVDF after formation, PVDF 20th cycles, C-PAVIm after formation and C-PAVIm after 20th cycles.

D. Conclusion

In conclusion, we have demonstrated that a cross-linked binder comprising cyclic and polymers can be utilized to improve the cycling performance. C-PAVIm as a binder in Si-graphite composite anodes demonstrated an enhanced performance as compared to the commercially employed PVDF binder. C-PAVIm-based electrode indicated the formation of a better SEI compared to PVDF-based electrode. These properties cumulatively led to the improved charge/discharge performance of the C-PAVIm binder. Also, it displayed an enhanced rate performance and higher discharge capacity than PVDF at higher charge/discharge rates indicating good stability. All of these results indicate C-PAVIm to be a potential alternative for PVDF as a binder in LIBs. It improved interaction with the electrode material and the current collector helps to maintain the electrode integrity over a long cycling. This innovative binder will provide a practical solution for polymer binder, which are highly promising electrode material.

Ⅲ. Radical Scavenging and Robust Polymer Binder

A. Introduction

Energy has been generally produced by consuming fossil fuels for decades up to today [1, 2]. As a result, fossil fuels are significantly depleting with serious environmental issues such as global warming and greenhouse gas emissions [3–7]. To achieve sustainable growth globally, it is necessary to ensure carbon neutralization by using Carbon Capture Utilization & Storage (CCUS), renewable energy, and biomass-recycling [8–10]. Among them, the utilization of carbon-neutral biomass is important now that the reduction of global warming gas emissions is urgently needed. Biomass is a well-known resource expected to be a powerful weapon against global warming because it has been counted as zero carbon dioxide (CO_2) emissions [11]. Currently, the technological development using biomass as energy or products is being actively pursued [12, 13].

The demand for eco-friendly and safe energy storage system in various fields is increasing rapidly [14, 15]. It has led to the active research on lithium-ion batteries (LIBs) with high energy density. LIBs have been generally used as energy storage devices in various applications such as a variety of portable electronic devices and electric vehicles [16]. A lot of electrode materials have been widely studied regarding LIBs anodes. However, the need to improve the performance and energy density of LIBs has increased interest in electrode material development. Graphite has been widely used as an anode material for LIBs because of its long-life properties, electrochemical stability, abundance, and price competitiveness. Unfortunately, the theoretical energy density of graphite is 372 mAh g^{-1} [17]. Thus, there is urgent to develop anode active material with higher energy density.

Researchers have been extensively studying materials with high lithium-ion storage capability silicon (Si) to replace the graphite anode in LIBs. Si has the highest theoretical capacity of ~3572 mAh g^{-1} and this is particularly attractive due to its low charge/discharge potential [18, 19]. Also, Si is abundant, low cost and eco-friendly which makes it more promising for high energy LIBs. However, Si anode materials

undergo significant volume changes (>300 %) during lithiation/delithiation and have low electrical conductivity. This causes poor electrical contact between conductive materials and Si particles besides severe crushing of Si particles and excessive growth of solid-electrolyte interfaces (SEI) layer [16, 20, 21]. Consequently, Si anodes exhibit fast capacity fading, low Coulombic efficiency, and electrode degradation during cycling [22–24]. In order to overcome this problem, many researchers have reported several approaches to improve the lifespan characteristics of Si anodes such as the manufacture of nano-sized Si particles, carbon coating to maintain electrical conductivity, core-shell structure to reduce persistent SEI layer formation and development of mechanically superior binders [19, 25-31]. Among the various approaches, the development of binders has received much attention because it is relatively simple and not only maintains the structural stability of the electrode, but also plays an important role for the stabilization of the electrode-electrolyte interface [32].

In general, poly(vinylidene fluoride) (PVDF) binders have been widely used [33]. However, it is PVDF is not suitable to prevent substantial volume expansion that occurs during charging and discharging of Si anodes [34]. Deadliest disadvantages of PVDF binder are its insulating feature and the usage of N-methyl pyrrolidone (NMP) is undesirable and not friendly to the environment [35]. Thus, it is essential to develop an eco-friendly, low-cost, water-soluble binder. In recent studies, several water-soluble polymer binders, such as carboxymethyl cellulose (CMC), polyvinyl alcohol (PVA), styrene-butadiene rubber (SBR), and polyacrylic acid (PAA), have been reported.[36–43]. Hydroxyl (-OH), carboxyl (-COOH), amino ($-NH_2$) functional groups present in the polymer binder can effectively combine with native oxide layer of Si surface [44]. In particular, carboxylic-rich binders forming the strong covalent bonds interactions with Si particles have been reported to promote cycle life growth of Si particle-based electrodes. The performance of carboxylic-rich binders is able to be enhanced by inducting adhesive groups into polymer chains.

Tannic acid (TAc) is significantly cheaper and more abundant, which is widely used in many industries such as food, pharmaceuticals, and cosmetics [45–47]. Moreover, as a natural polyphenol compound, it has been widely used for material preparation and modification in the various fields of energy devices. Nowadays, most TAc is being

studied as an eco-friendly adhesive and coating due to its high solubility in water and high reactivity with aldehydes, as well as its economical aspect [48, 49]. Especially TAc has many remarkable properties as antioxidant [49–53]. Thus, we assume that the polyphenols of TAc maybe will scavenge the superoxide radicals during the discharge and charge processes, and then improve the cycle stability of LIBs. This can not only prevent excessive SEI layer formation, but also improve the conductivity of Li-ions [54–58]. The binder we designed is unique because the elimination activity of superoxide radicals generated by electrolyte decomposition is inside the battery.

Herein, we present cross-linkable PAA/TAc as a water-soluble binder for Si anodes.

This binder inhibits side reactions during cycling because of the antioxidant characteristics of TAc, contributes to the formation of a compact SEI layer, and improves the conductivity of Li ions. The obtained cross-linked network structure of the C-PAA/TAc binder would benefit the Si anode by buffering the change in volume. Therefore, we demonstrate that a cross-linked binder can be utilized to improve the cycling performance and mitigate the large volume expansion of Si anodes upon the incorporation of Li.

B. Experimental

1. Materials

PAA (ACROSS, M.W. 240,000), TAc (Sigma Aldrich, M.W. 1701.20), methanol (MeOH) (Duksan), 2,2-Diphenyl-1-picrylhydrazyl (DPPH) (Alfa Aesar), MeOH (Duksan, HPLC Grade), silicon nanoparticles (50 nm, Nanostructured & Amorphous Materials, Inc.), and Super P (Wellcose) were used without further purification.

2. Method

a. Prepared PAA/TAc Film

A 10 wt% mixed solution was prepared to synthesize cross-linkable PAA/TAc. The prepared PAA/TAc (8:2, 5:5, AND 2:8) were placed in a vacuum oven at 150 ^{o}C for 2 h to conduct thermal cross-linking. They were designated as C-PAA/TAc (8:2), C-PAA/TAc (5:5) and C-PAA/TAc (2:8), respectively, and were immersed in MeOH to remove any unreacted monomers. Finally, the samples were dried overnight in a vacuum oven at room temperature (Figure 1).

b. DPPH Radical Scavenging Assay

DPPH is a stable free radical that is typically used to test the radical-scavenging activity of antioxidant molecules. The DPPH radical scavenging activities of TAc, PAA, and C-PAA/TAc were measured using ultraviolet–visible (UV-vis) spectroscopy. In terms of the radical-scavenging mechanism, the antioxidant molecule serves as a hydrogen donor, transforming the DPPH radical into its reduced form. Therefore, the radical property of DPPH is neutralized, and its color transforms from purple to yellow. Briefly, a 0.2 mM DPPH solution prepared in MeOH (HPLC grade) solution and the sample solution were mixed for 30 min at room temperature. All measurements were performed under dim-light conditions. Spectrophotometric measurements were performed at a wavelength of 517 nm.

3. Characterization

The chemical structure of C-PAA/TAc was characterized via UV-vis absorbance (Amersham Biosciences, Ultrospec 2100 pro). The chemical structures of the films were analyzed using Fourier-transform infrared spectrometry (FT-IR, Nicolet6700). The thermal properties of C-PAA/TAc were investigated using differential scanning calorimetry (DSC, TA Instruments DSC25) under a N_2 atmosphere (at a temperature range of 25 °C−180 °C and a heating rate of 5 °C min^{-1}) and thermogravimetric analysis (TGA, TA Instruments SDT650) under a N_2 atmosphere (at a temperature range of 25 °C−1000 °C and a heating rate of 10 °C min^{-1}). The morphology of the electrodes was investigated using scanning electron microscopy (FE-SEM (MSE40) UHR FE-SEM). To confirm the degree of chemical cross-linking, the gel content was determined using the solvent extraction method and calculated as follows:

$$\frac{M_2}{M_1} \times 100\% = \text{gel content},$$

where M_1 is the weight of C-PAA/TAc, and M_2 is the weight of the extracted solvent [59]. The peel-off test was conducted by Universal Testing Machine (Shimadzu, Japan) at an extension speed of 50 mm min^{-1}. Each electrode was taped with a 3M magic tape (2.5 cm in width).

4. Preparation of Si anode for Half-Cells

Silicon slurries were prepared by mixing 60 wt% of silicon nanoparticles as the active material, 20 wt% of PAA and TAc solution as binders, and 20 wt% of Super P as a conducting agent in deionized water. For comparison, the binders were mixed at various mass ratios of 5:5, 8:2, and 2:8 (PAA:TAc) and labeled as C-PAA/TAc (5:5), C-PAA/TAc (8:2), and C-PAA/TAc (2:8), respectively. The mixtures were cast on Cu foil using a doctor blade, which measured 40 μm thick. Additionally, an electrode with a higher mass loading was fabricated by controlling the amount of deionized water in the slurries. The coated electrode was dried in a convection oven at 80 °C for 1 h,

followed by in a vacuum oven at 150 °C for 2 h. The low (0.35 mg cm^{-2}) and high (1.1 mg cm^{-2}) mass loading electrodes were prepared to conduct the different electrochemical performance.

5. Electrochemical Characterization

The CR2032 coin-type half cells of Si anode was assembled in a glove box (KK-011AS, KIYON, Korea) under an argon atmosphere (O_2 < 0.01 ppm, H_2O < 0.01 ppm). The electrodes were punched into disks with a diameter of 14 mm. A lithium foil (Wellcos, Korea) measuring 300 μm thick was punched into disks with a diameter of 16 mm as the counter and reference electrodes. The silicon anodes were separated using a polypropylene separator (Cellgard 2400) in a coin cell. The electrolyte was 1M LiPF6 dissolved in a mixture of ethylene carbonate (EC), and diethyl carbonate at a volumetric ratio of 3:7 with the addition of 10 wt% fluoroethylene carbonate (FEC) and was purchased from Wellcos. The galvanostatic charge/discharge performance of the precycle was tested at a rate of 0.05C, and the cycling performance of the coin cells for 100 cycles was tested at a rate of 0.5C in the voltage window of 0.05 to 1.0 V (vs. Li/Li^+) at room temperature. (1C = 3000 mA g^{-1}). Electrochemical impedance spectroscopy (EIS) was performed at a 10 mV amplitude signal in the frequency range of 500 kHz to 0.1 Hz.

C. Results and Discussion

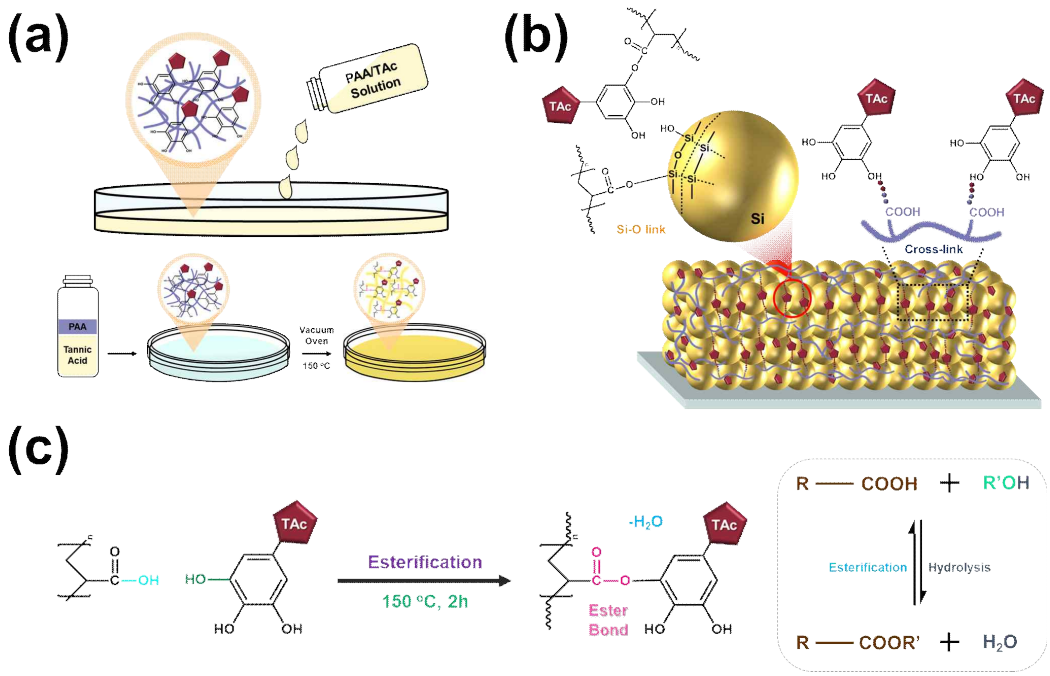

Figure 1. Schematic illustration showing preparation of binder using poly(acrylic acid) (PAA) and tannic acid (TAc). (a) PreparationofPAAandTAcsolution; (b) Nano-sized Si particles and interaction between PAA and TAc; (c) PAA and TAc structure.

1. FT-IR Spectra

FT-IR spectroscopic analysis in the 500–4000 cm^{-1} region reveals the characteristic bands for PAA, TAc, C-PAA/TAc (8:2), C-PAA/TAc (5:5), and C-PAA/TAc (2:8); the results are presented in Figure 2. The ordinary peaks at 3340 and 1028 cm^{-1} were assigned to the -OH stretching vibration. The peaks near 2800−3000 cm^{-1} and 1319 cm^{-1} were due to C−H stretching vibrations assigned to the -CH and -CH_2 groups of aliphatic hydrocarbons. The characteristic peaks at 1645, 1707, and 1604 cm^{-1} were attributed to the C=O stretching frequency of the ester groups. The absorption band at 1448 cm^{-1} was attributed to the aromatic C=C of TAc. The bands at 1193 cm^{-1} are characteristic of C−O formed by interchain cross-linking. The high intensity C−C stretching peak at the bands in the 616–890 cm^{-1} were associated with the C−H of benzene rings and the O−H of alcohol vibrations. The strong interaction between PAA and TAc is the key factor affecting the stability of silicon-based electrodes [45, 60, 61]. Morever, Figure 3 displays the overall structures of the TAc. And the cross-linked structure of PAA and TAc can be seen in Figure 4.

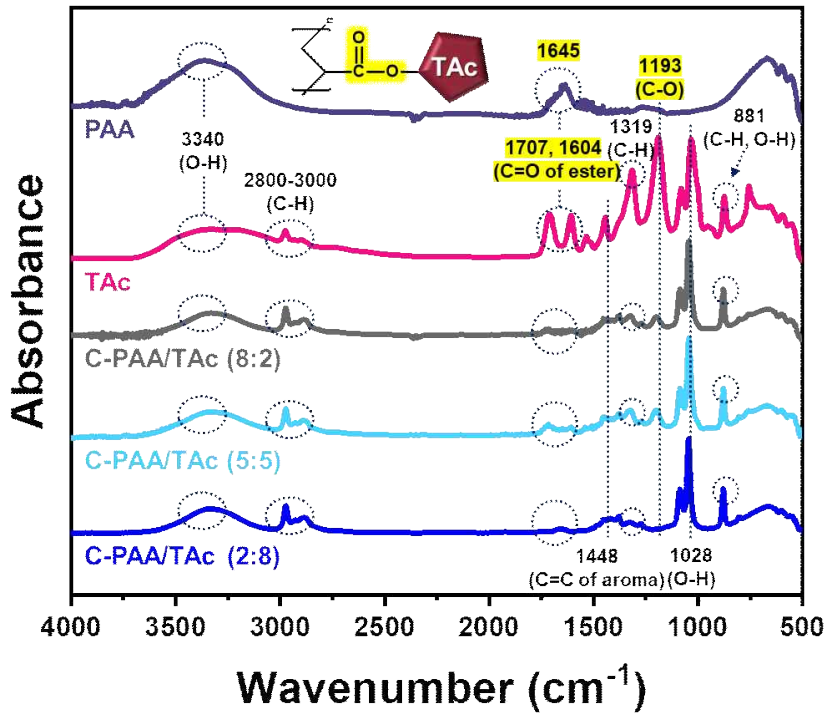

Figure 2. FT-IR spectra of PAA, TAc, C-PAA/TAc (8:2), C-PAA/TAc (5:5), and C-PAA/TAc (2:8).

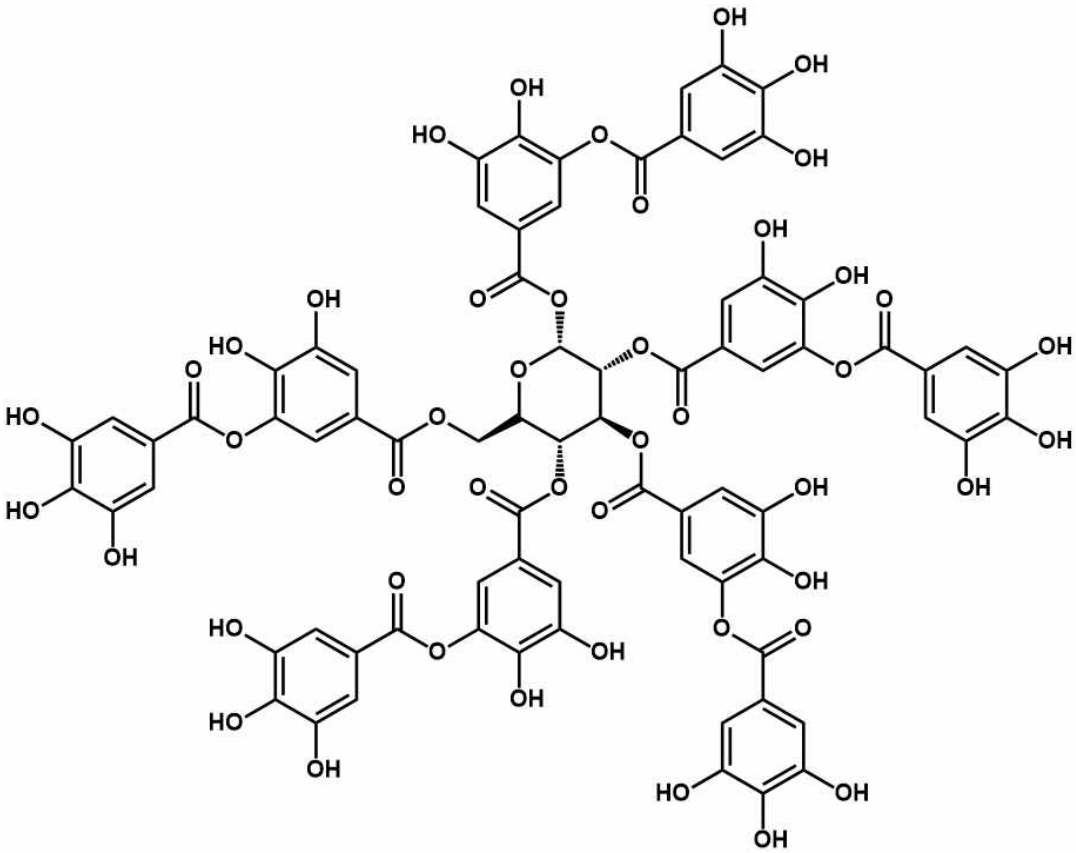

Figure 3. Molecular structure of tannic acid (TAc).

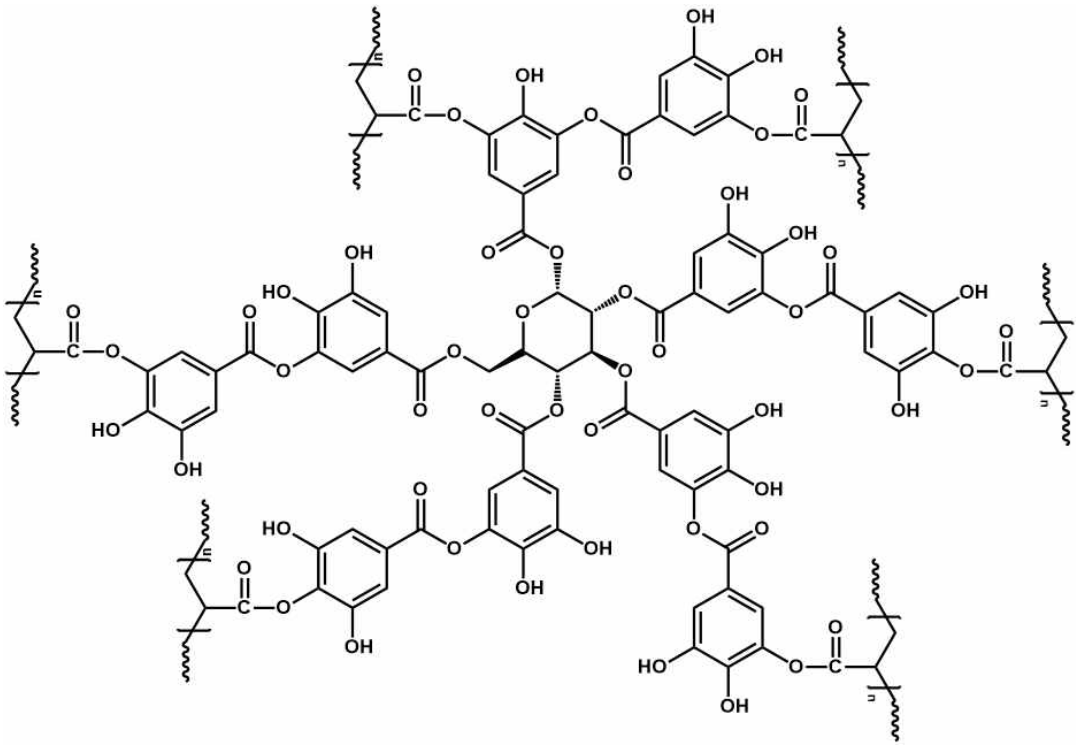

Figure 4. Cross-linked binder formed by condensation between PAA and TAc.

2. Gel Content Analysis

To confirm the degree of cross-linking, the gel content of C-PAA/TAc was measured for each weight ratio, as shown in Figure 5. The gel content was the highest for C-PAA/TAc (5:5). These results indicate that cross-linking was effective when the PAA and TAc weight ratios were equal. Conversely, as the amount of TAc increased, cross-linking occurred less, similar to C-PAA/TAc (2:8) [48, 62]. A similar trend was observed from the results of FT-IR, DSC, and TGA.

Condensation reaction between the COOH groups of PAA and OH group of TAc will cause the hydroxyl (-OH) groups to disappear. In organic chemistry, a condensation reaction is a type of chemical reaction in which two molecules are combined to form a single molecule, usually with the loss of a small molecule such as water. This condensation reaction can be seen in Figure 1 c. When thermal annealing is performed to form a cross-linking structure, a dehydration reaction occurs, resulting in an ester (-O-C=O) bond between PAA and TAc.

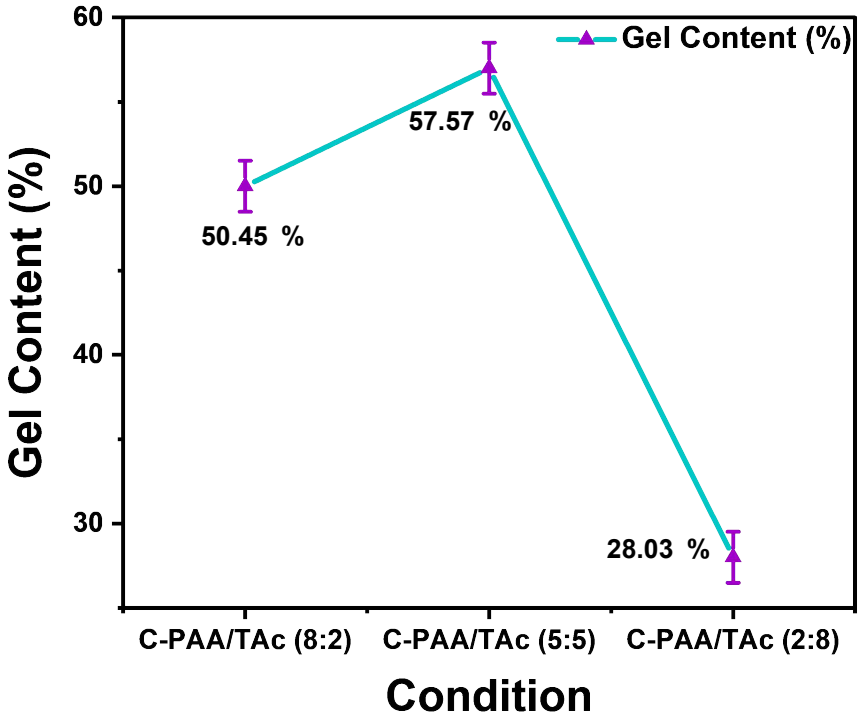

Figure 5. Gel contents of C-PAA/TAc (8:2), C-PAA/TAc (5:5), C-PAA/TAc (2:8).

3. DSC Curves

The thermal behavior of C-PAA/TAc was analyzed via DSC, which is a typically used method for investigating polymer composites (Figure 6). All the samples showed similar images. C-PAA/TAc (8:2) and C-PAA/TAc (2:8) indicated glass transition temperatures (Tg) of 131 ℃ and 137 ℃, respectively, whereas C-5:5 indicated a Tg of 158 ℃. The thermal properties of C-PAA/TAc (5:5), analyzed via DSC, were significantly better than those of C-PAA/TAc (8:2) and C-PAA/TAc (2:8). This thermal behavior shows similar tendencies in both Figure 3, and is an indicator that the characteristics of C-PAA/TAc (5:5) are the most excellent in electrochemical characteristics.

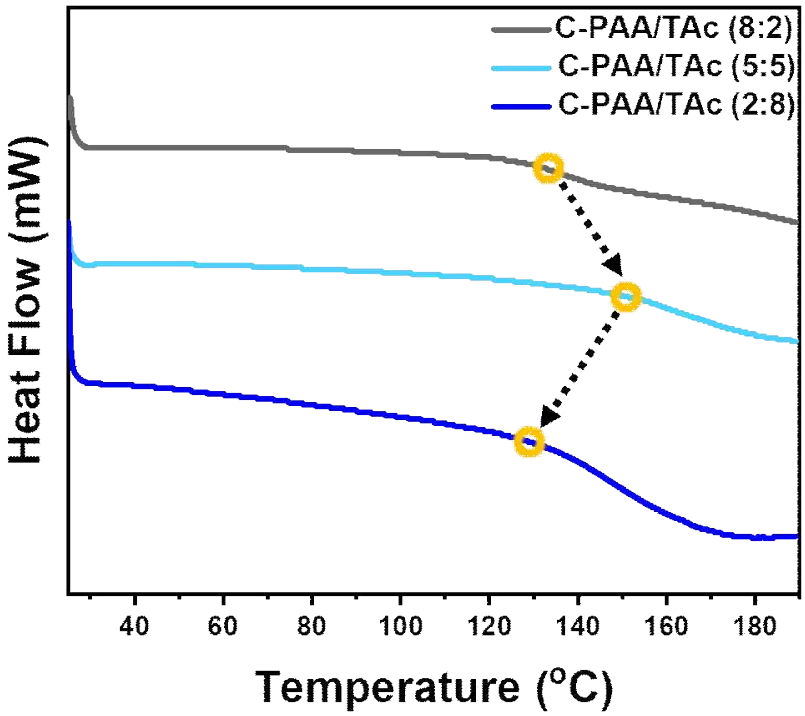

Figure 6. DSC curves of C-PAA/TAc (8:2), C-PAA/TAc (5:5), C-PAA/TAc (2:8).

4. TGA Curves

The TGA results show that C-PAA/TAc (5:5) and C-PAA/TAc (2:8) exhibited similar thermal behaviors in the first stage (Figures. 7 a and b). However, they exhibited different thermal behaviors in the second stage. The first weight loss stage (< 5%) occurred from room temperature to 210 °C, which was induced by the evaporation of absorbed water from the sample. The second weight loss stage occurred from 210 °C to 320 °C. The second mass loss lying in between 210 and 320 °C is attributed to the decomposition of groups (e.g., oxygen-containing groups) and the oxidation of carbon. The third weight loss stage, which occurred form 320 °C to 700 °C, was caused by the decomposition of the C-PAA/TAc interaction. All samples exhibited weight losses of less than 5% below 210 °C, which is more than sufficient for Si anode applications. Hence, the good thermal stability of C-PAA/TAc (8:2), C-PAA/TAc (5:5), and C-PAA/TAc (2:8) was confirmed. The Figure 7 b shows the final weight when the temperature is raised from room temperature to 1000 ºC.

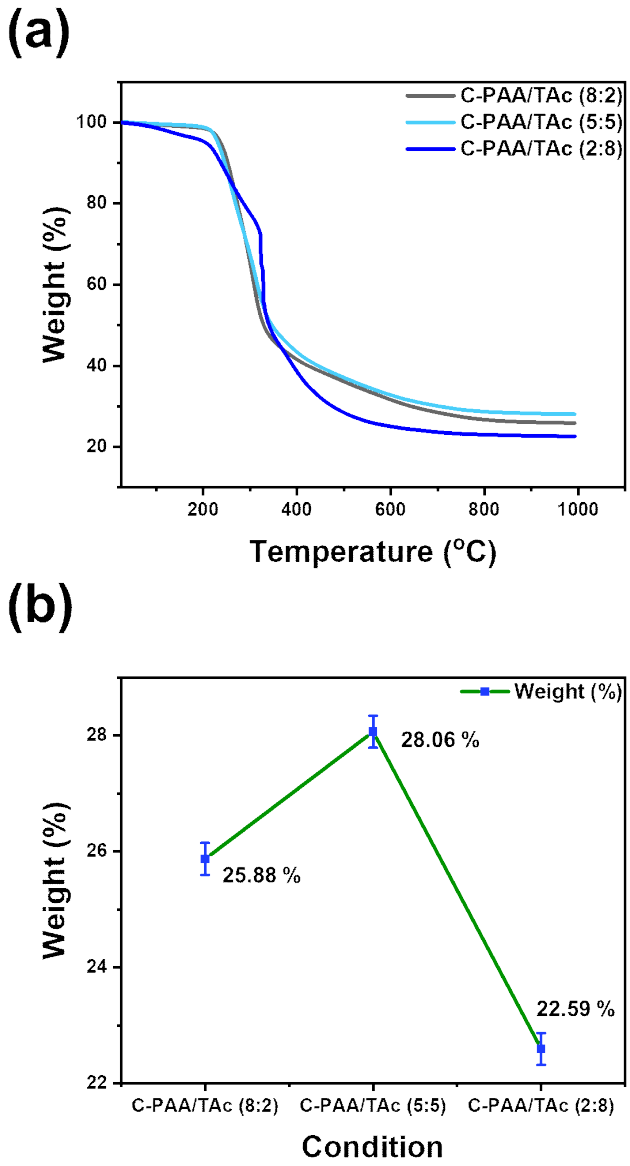

Figure 7. TGA curves of (a) C-PAA/TAc (8:2), C-PAA/TAc (5:5), C-PAA/TAc (2:8); (b) Final weight based on TGA.

5. DPPH Radical scavenging activity

Various methods are currently used to assess the antioxidant activity of plant phenolic compounds. DPPH has been widely used to evaluate the free-radical scavenging effectiveness of various antioxidant substances. In the DPPH assay, antioxidant activity analysis is performed based on the inhibition of the DPPH radical by antioxidants.

The optimal initial concentration of DPPH was evaluated to determine the assay sensitivity. The intensity represented in violet increased rapidly as the DPPH concentration increased from 0 to 0.2 mM [63, 64]. Using this method, the antiradical power of the antioxidant can be determined based on the decrease in the absorbance of DPPH• at 517 nm (Figure 8) [65, 66].

Figure 8 a illustrates the significant decrease in the concentration of DPPH radicals owing to the scavenging ability of TAc and a standard. The scavenging effects of TAc and the standard on the DPPH radicals decreased in the order of C-PAA/TAc (2:8) > C-PAA/TAc (5:5) > C-PAA/TAc (8:2); quantitatively, they were 92.66%, 92.57%, and 80.50%, respectively. The DPPH free radical-scavenging activity of TAc increased with the TAc ratio Figure 8 b [67, 68]. The reaction between the antioxidant and DPPH free radical can be seen in Figure 9.

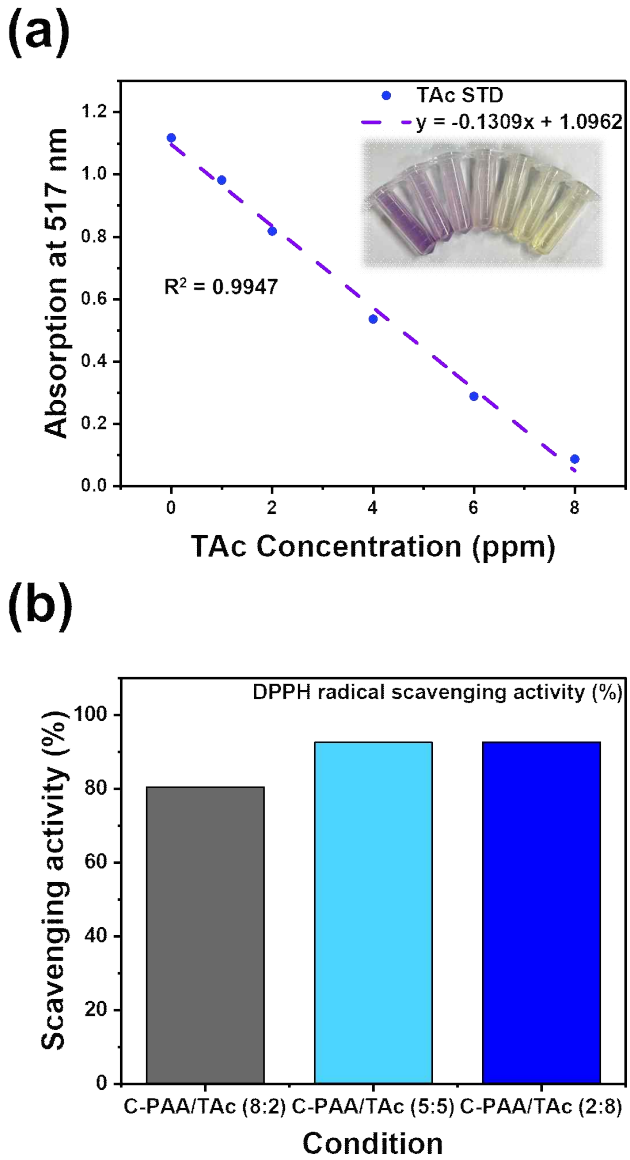

Figure 8. (a) Absorption vs. TAc concentration; (b) DPPH radical scavenging activity of C-PAA/TAc.

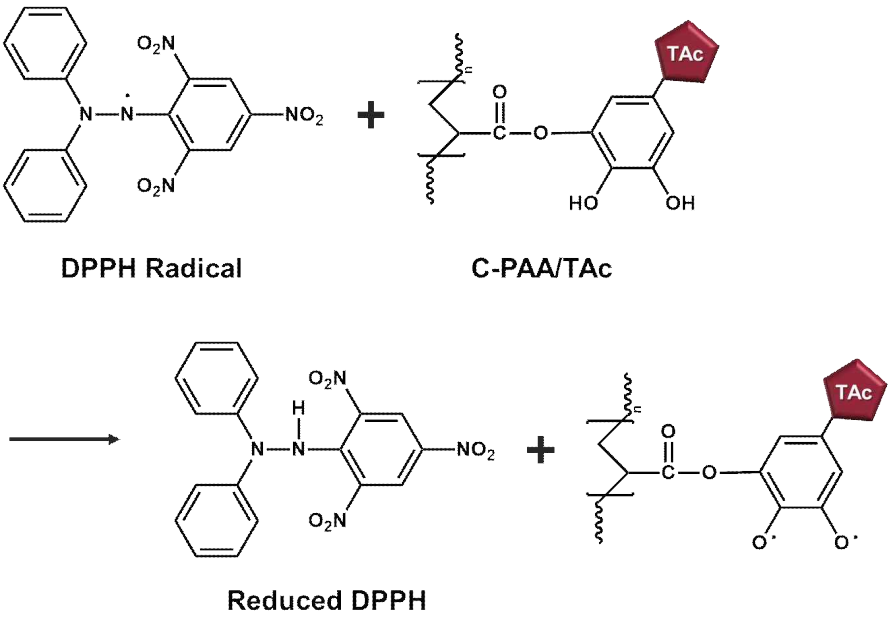

Figure 9. Reaction of antioxidant and DPPH free radical.

6. Electrochemical Analysis

The results in Figure 10 b show that the first galvanostatic charge/discharge voltage profiles of the Si C-PAA/TAc binser electrode were evaluated in the 0.05−1 V vs. Li/Li+ voltage range at room temperature at 0.05C. Significantly, Si C-PAA/TAc (8:2), C-PAA/TAc (5:5), C-PAA.TAc (2:8) electrodes exhibit higher reversible capacities (2706, 2672, 2595 mAh g^{-1}) than the PAA and TAc electrode (2583, 2205 mAh g^{-1}), which is probably ascribed to excellent adhesive abilities and improved mechanical properties of C-PAA/TAc electrodes.

The initial Coulombic efficiencies of the Si C-PAA/TAc (8:2), C-PAA/TAc (5:5), C-PAA.TAc (2:8), PAA and TAc electrodes were 82.6%, 81.5%, 79.4%, 82.3% and 73.3%, respectively. These results indicate the initial Coulombic efficiencies of C-PAA/TAc (2:8) and TAc were lower than those of the other electrodes because these electrodes featured weak chemical bonds, which hindered electrical conduction owing to the excessive polyphenol groups [69, 70]. Meanwhile, the capacities of C-PAA/TAc (5:5) and C-PAA/TAc (8:2) were much higher than that of the Si PAA electrode, indicating that the cross-linked structure of C-PAA/TAc accommodated the volume change in Si without pulverization and contributed to the formation of a compact SEI layer [46].

Figure 10 c displays the long-term cycle performance of all electrodes with different polymeric binders at 0.5C for 100 cycles. The C-PAA/TAc (8:2), (5:5), and (2:8) electrodes retained much higher capacities after 100 cycles than the PAA and TAc electrodes. C-PAA/TAc (5:5), which indicated a higher cross-linking degree than C-PAA/TAc (8:2) and C-PAA/TAc (2:8), as confirmed in Figure 5. These results indicate that cross-linking was effective for electrode.

We evaluated the adhesion strength of Si electrodes with PAA and C-PAA/TAc binders to conduct a 180° peel-off test in Figure 11. As a result, the average peel strengths of the Si electrodes with PAA, C-PAA/TAc (8:2), C-PAA/TAc (5:5), C-PAA/TAc (2:8), TAc, and PVDF were 4.08, 4.11,5.48, 2.29, 1.21, and 0.47 N, respectively. The applied Si anode with a C-PAA/TAc (5:5) binder was 5.48 N, which was higher than the Si electrodes with other binders. Furthermore, the C-PAA/TAc

(5:5) binder showed that a large amount of anode materials was retained on the current collector after peeling (Figure 11). These results suggest that the increase in electrode adhesion strength is attributed to the hydrogen bonding interaction between our binder and the Si powder. Based on these results, the adhesion properties of the designed binder clearly demonstrate an advantage as a binder for Si anodes.

In addition, the Coulombic efficiency of all electrodes showed approximately 98% over the entire cycle (Figure 10 d). The electrochemical performance of all electrodes is listed in Table 1. Excellent cycle stability and high reversible capacity were achieved because TAc with numerous hydrogen bonds can interact with silicon, and the strong adhesive cross-linking between the TAc and PAA chains can hinder significant volume changes and structural collapse during continuous cycles [46, 71].

Figure 10 e shows the nyquist plots of the Si PAA, C-PAA/TAc (8:2), C-PAA/TAc (5:5), C-PAA.TAc (2:8) electrodes after 100 cycles. To determine the resistance properties of the electrodes with different binders, we conducted EIS after 100 cycles. The measured resistance is presented in Table 2. The resistance in the high-frequency region corresponds to the resistance of the ionic electrolyte (R_s), the diameter of the semicircle represents the interfacial resistance of the anode material (R_{SEI}), and the medium-frequency region is associated with the charge transfer resistance (R_{ct}). we can find obviously all of Si C-PAA/TAC electrodes have much smaller semicircles than the Si PAA electrode, which indicates the Si C-PAA/TAc electrodes have much better charge transfer abilities that is, the cross-linked network structure of the C-PAA/TAc binder can help decrease R_{ct}.

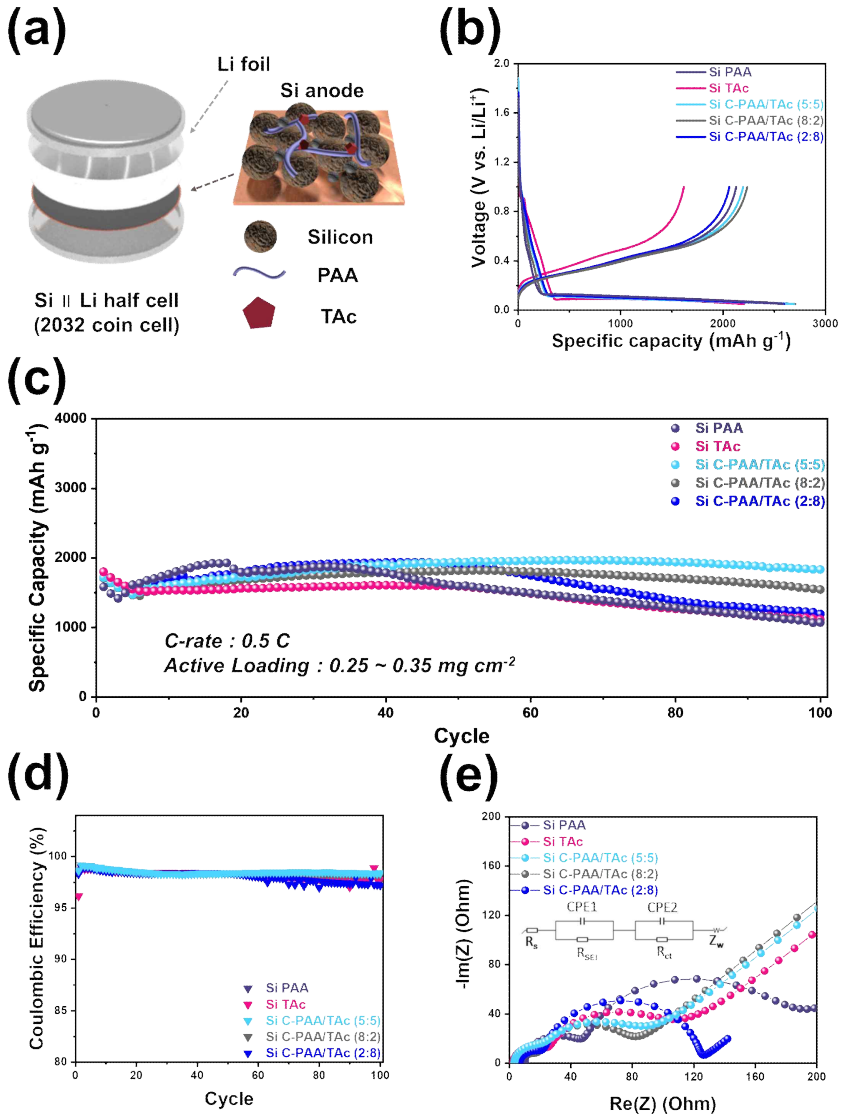

Figure 10. (a) Schematic assembly illustration of Si ‖ Li half cell configuration; (b) Galvanostatic charge-discharge profiles for half cell by controlling binder ratio of C-PAA/TAc; (c) Cycling performance of Si PAA, Si TAc and Si C-PAA/TAc at 0.5 C-rate; (d) Coulombic efficiency of cycling performance of Si PAA Si TAc and Si C-PAA/TAc; (e) Electrochemical impedance spectroscopy of Si PAA, Si TAc and C-PAA/TAc after 100 cycles.

Table 1. Electrochemical performances of Si PAA, Si TAc and Si C-PAA/TAc

	1st Discharge Capacity (mA h g^{-1})	1st Charge Capacity (mA h g^{-1})	1st Cycle Efficiency (%)	100th Cycle Capacity (mA h g^{-1})	Capacity Retention (100th Cycle)
Si PAA	2583	2126	82.30	1072	67.61
Si TAc	2205	1617	73.33	1112	61.74
Si C-PAA/TAc (5:5)	2692	2195	81.53	1833	106.5
Si C-PAA/TAc (8:2)	2706	2235	82.59	1545	90.35
Si C-PAA/TAc (2:8)	2595	2061	79.42	1193	69.36

Table 2. EIS data of Si PAA, Si TAc and Si C-PAA/TAc after 100th cycles.

	R_s at 100th Cycle	R_{SEI} at 100th Cycle	R_{ct} at 100th Cycle
Si PAA	10.45	11.23	144.33
Si TAc	2.69	23.08	71.79
Si C-PAA/TAc (5:5)	3.28	20.32	55.47
Si C-PAA/TAc (8:2)	6.81	10.31	53.6
Si C-PAA/TAc (2:8)	6.27	13.58	102.1

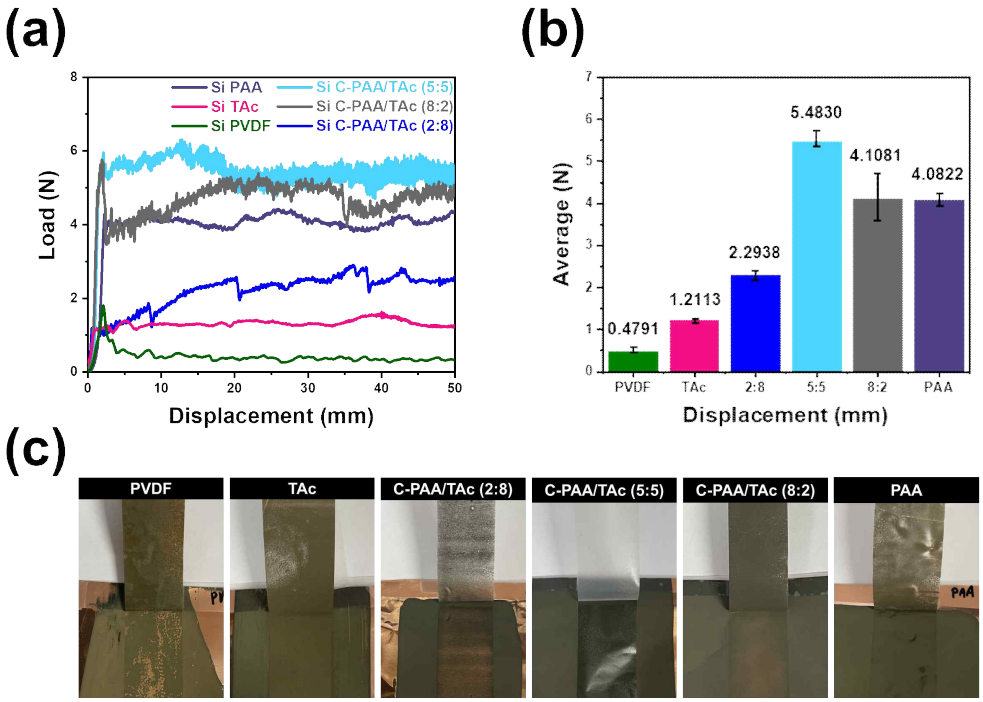

Figure 11. (a) Optical images of the tapes peeled from the Si PVDF, Si TAc, Si C-PAA/TAc, and Si PAA electrodes; (b) 180° peel-off test results of Si PVDF, Si TAc, Si C-PAA/TAc, and Si PAA electrodes EIS data of Si PAA, Si TAcand Si C-PAA/TAc; (c) The average peeling forces.

7. SEM Images

To further confirm the mechanism of the C-PAA/TAc binder, the cross-sectional scanning electron microscopy (SEM) to understand the morphology change and measure the thickness of the electrodes after 100 cycles were also characterized. As shown in Figure 12 a and c, the thickness of Si PAA and Si C-PAA/TAc electrodes before cycling were 7 and 6.5 um, respectively. After cycling, the thickness of the Si PAA and Si C-PAA/TAc electrodes were 24 and 16 um, respectively (Figure 12 b and d, respectively), which corresponded to expansion levels of 350% and 250%, respectively. The SEM images indicate the volume expansion that typically occurs in the Si anodes. However, However, the C-PAA/TAc binder demonstrated superior mechanical properties that allowed it to maintain its active materials during cycling [72].

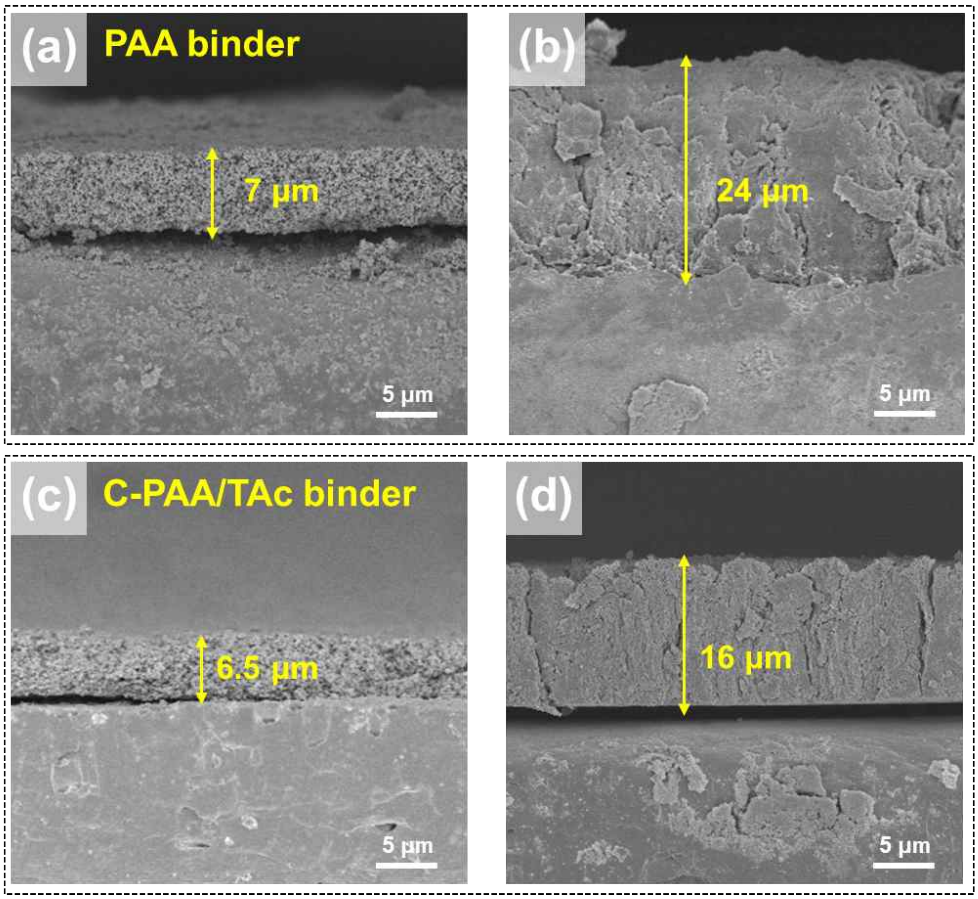

Figure 12. Cross-sectional SEM images: (a) Si PAA electrode and (b) After 100 cycles; (c) Si C-PAA/TAc (5:5) electrode and (d) After 100 cycles.

8. Electrochemical Performances

To commercialize Si C-PAA/TAc for use in LIBs, we tested the electrode using our stable binder for the si anode at a high mass loading (~1.1 mg cm^{-2}), as shown in Figure 13 and Figure 14. The discharge capacity of the C-PAA/TAc electrode with high mass loading was determined to be 2361 mA h g^{-1}_{Si}, and the initial Coulombic efficiency was 82.6% after the first cycle. These values were higher than those for the Si PAA electrode (1602 mA h g^{-1}_{Si} and 77.0%) (Figure 13 a). These electrodes were tested for over 60 cycles. The results show that the capacity retention of the Si C-PAA/TAc electrode with high mass loading was 79.8% after 60 cycles, and its discharge capacity after cycling was 1219 mA h g^{-1}_{Si}, which was much higher than that of Si PAA (804 mA h g^{-1}_{Si}) (Figure 13 b). These results indicate that the cross-linked structure prevented some of the active materials from collapsing from the current collector despite the high active material loading [73].

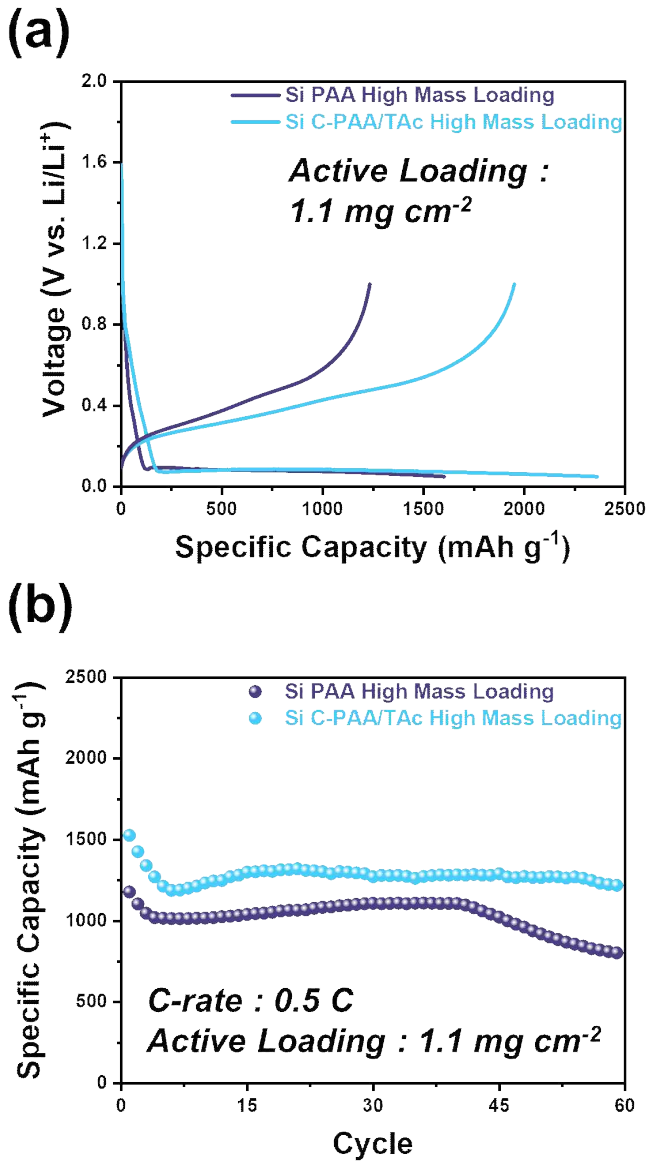

Figure 13. Electrochemical performances of the Si ‖ Li half-cell with a high mass loading (~1.1 mg cm^{-2}): (a) Galvanostatic charge-discharge profiles for half cell Si PAA and Si C-PAA/TAc (5:5); (b) Cycling performance of Si PAA and Si C-PAA/TAc at 0.5 C-rate.

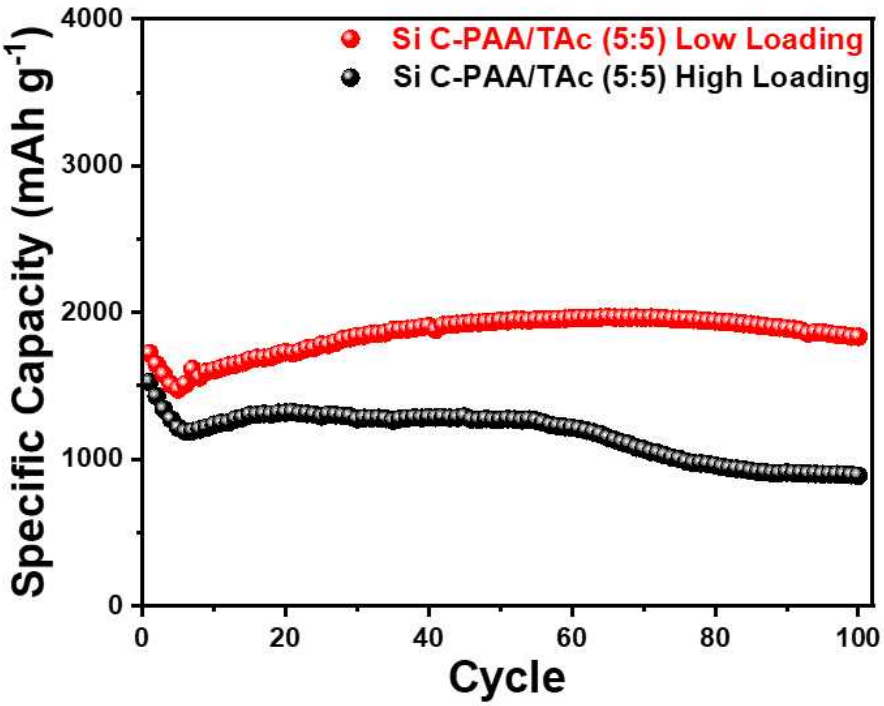

Figure 14. Cycling performance of Si C-PAA/TAc low (~ 0.35 mg cm^{-2}) and high (~1.1 mg cm^{-2}) loading at 0.5 C-rate.

D. Conclusion

Herein, an excellent cross-linked PAA/TAc binder that can be used for the Si anode of LIB is reported. It was shown that TAc with plentiful -OH groups was effectively cross-linked with PAA to achieve high electrochemical performance. These -OH groups readily formed a network structure during cross-linking. Particularly, TAc, which exhibits excellent antioxidant properties, can suppress side reactions during cycling by resident DPPH radicals and maintain stability of LIBs through antioxidants. This not only prevents excessive formation of the SEI layer, but also enhances the conductivity of the Li-ion. We present a unique feature of C-PAA/TAC as a radical scavenging that improves the electrochemical performance of LIBs. Therefore, the C-PAA/TAc binder offers better electrochemical performance. This study demonstrated a sustainable method for manufacturing a robust polymeric binder with high electrochemical durability and excellent radical scrubbing activity. In the future, these innovative binders will be able to provide practical solutions for Si anodes.

Ⅳ. Cross-Linked Organic/Inorganic Polymer Binder

A. Introduction

With advancements in technology, modern society is demanding the development of high-efficiency, high-density, and long-life energy storage devices, ranging from portable electronic devices to electric vehicles [1, 2]. Energy has been generated based on fossil fuels for decades up to this day, but fossil fuels are gradually depleting, causing serious environmental problems such as global warming and environmental destruction [3]. Fossil fuels have been used to produce energy for several decades. Formulating and implementing strategies to develop clean and sustainable energy systems to reduce the consumption of fossil fuels and alleviate environmental pollution is of global significance [4].

Energy storage systems (ESS) play a prominent role in the proper utilization and storage of green energy. Supercapacitors, which store energy by the adsorption of ions or surface redox reactions, are considered the most promising ESSs [5–8].

Supercapacitors offer advantages such as shorter charging/discharging times and higher power densities compared to those offered by lithium-ion batteries (LIBs) [9]. Electrochemical double-layer capacitors (EDLCs) store charges electrostatically at the interface between the electrode material and electrolyte [10, 11]. In response to fast surface redox reactions, pseudocapacitors (PSEUDOs) store charges in the electrode, providing a capacitive-like electrochemical behavior. The active materials of PSEUDO exhibit higher capacitances than those of EDLCs do. However, such PSEUDOs often produce a compromised rate capability and reversibility because they rely on faradaic redox reactions.

Most polymer binders only occupy a small proportion (<5 wt%) of commercial electrodes [12–15]. However, they play an important role in physically stabilizing electrodes [16–20]. When used as binders, polymer materials should not chemically reject organic electrolytes and should instead maintain stable adhesive properties without undergoing side reactions, even in an electrochemical environment. Although polyvinylidene fluoride (PVDF) is the most successful and widely used binder for

conventional LIBs, it suffers from several limitations such as having weak intermolecular interactions with active materials and showing an insulating to support the fast ion transport required under high rates [21, 22].

The homogeneous composite structure of pristine electrodes gets disrupted because of substantial volume changes, leading to mechanical failure and capacity loss over repeated charge/discharge cycles. Several studies have pointed out that the cyclability-related problems of most promising advanced electrode materials can be alleviated by using more efficient battery binders [23–27].

An ideal electrode matrix should (1) form strong interactions with active materials to maintain adhesion over cycles; (2) offer strong adhesion toward current collectors to prevent electrode delamination; (3) provide a continuous conductive network within the electrode; and (4) be electrochemically and chemically stable in harsh environments for batteries [28, 29].

A class of polymers that has recently garnered attention are polymeric ionic liquids (PILs), whose high electrochemical stability, conductivity, and good processability support their suitability for electrochemical applications [30, 31]. They have been successfully incorporated in supercapacitors, electrochemical sensors, and a variety of energy devices. PILs can wrap powder components while still allowing ion flow, improving cyclability [32].

The cross-linking of polymer binders has been proposed as an effective and simple method for the volume expansion of electrodes [33, 34]. Thermal and mechanical analyses that were conducted to examine some cross-linked polymers revealed a raised glass transition and rheology in them like those in permanently cross-linked polymer matrices.

In this study, we present nickel oxide (NiO) synthesized by the sol-gel method and a cross-linkable organic/inorganic hybrid polymer successfully obtained through the quaternization of poly(N-vinyl imidazole) (PVIm) with a unique functional group containing ethoxysilane. We assumed that durability would be improved through the formation of Si-O bonds between the polymer chains and the active material from introducing a cross-linkable silane group. We fabricated a PSEUDOs with PVIm; the corresponding electrode could provide cycle stability through the simultaneous

improvement in the ion conductivity and physical properties of the composite through cross-linking. Currently, the main trend is developing devices that can be stored while maintaining the cycle characteristics and also increase the output energy; continuous research and development on PSEUDOs is expected to create new opportunities because they are located in an industry group.

B. Experimental

1. Materials

1-Vinylimidazole (Vm) (Alfa Aesar), a,a'-azobisisobutyronitrile (AIBN) (JUNSEI), (3-chloropropryl)triethoxysilane (3CPTES) (Sigma Aldrich), dimethylformamide (DMF) (JUNSEI), acetone (Duksan), methanol (MeOH) (Duksan), Nickel(II) nitrate hexahydrate ($Ni(NO_3)_2 \cdot 6H_2O$) (Alfa Aesar), Hexamethylenetetramine (HMTA) (KANTO), Carbon black (Alfa Aesar), PVDF 1 wt% solution, N-Methylpyrrolidone (NMP) (SAMCHUN) were used without any further purification. AIBN was recrystallized from MeOH.

2. Method

a. Synthesis of Poly(vinyl imidazole)

Vm was polymerized out via free radical polymerization, as shown in Figure 1. Initially, Vm and DMF were briefly added to a round-bottom flask equipped with a magnetic stirrer. AIBN was added into the flask and the mixture was slowly heated to 70 °C under a nitrogen atmosphere. After radical polymerization for 24 h, the resulting yellow viscous solution was cooled to room temperature and precipitated with acetone; this was followed by filtration, which yielded a white powder. The vacuum was dried overnight at 40 °C. The white powder was dissolved in DMF, and the precipitation process was repeated twice. Finally, the resulting wet powder was dried overnight under vacuum at 60 °C to obtain a white powder of PVIm.

b. Quaternization of PVIm with 3CPTES

PVIm_Si was synthesized via the nucleophilic substitution reaction (S_N2) of PVIm and 3CPTES. This synthesis was conducted at molar ratios of 100:50, 100:70, and 100:100.

PVIm and 3CPTES (50, 10.7 mmol), (70, 14.9 mmol), (100, 21.2 mmol) and DMF 40 mL were added to a 250 mL round bottom flask equipped with a magnetic stirrer. The mixture was then stirred at 40 °C for 48 h. The resulting solution was precipitated with acetone, followed by filtration to a white powder. The white powder was dried

overnight under vacuum at 40 °C as shown in Figure 1.

c. Cross-linked Poly(1-vinyl-propyl triethoxysilane imidazolium)·Cl^-

Finally the prepared PVIm_Si films were placed in vacuum at 150, and 160 °C for 1, 2, and 1 h, respectively, to conduct thermal cross-linking. We referred to the obtained sample as C-PVIm_Si.

d. Synthesis of $Ni(OH)_2$ Nanostructure

$Ni(NO_3)_2 \cdot 6H_2O$ and HMTA were dissolved in deionized (DI) water water under magnetic stirring. The mixed solution was then transferred into a 100 mL vial, maintained at 100 °C for 4 h, and then cooled naturally. The synthesized nickel hydroxide products were cleaned by washing with D.I water. The prepared samples were then freeze-dried for 48 h [35].

e. Synthesis of Porous NiO Nanostructure

Porous NiO nanostructure powders were obtained by annealing the as prepared $Ni(OH)_2$ samples at 300 °C for 2 h. NiO is generally known to exhibit excellent electrochemical properties including pseudocapacitance [35, 36].

3. Characterization

The chemical structures of the films were analyzed using Fourier-transform infrared spectroscopy (FT-IR, Nicolet6700) and proton nuclear magnetic resonance (^{1}H-NMR spectra, JEOL-JNM-AL300) in dimethyl sulfoxide-d_6 (DMSO-d_6) at 300 MHz. The thermal properties of C-PVIm were investigated using differential scanning calorimetry (DSC, TA Instruments DSC25) under a N_2 atmosphere (in a temperature range of 25 °C−180 °C and a heating rate of 5 °C min^{-1}) and via thermogravimetric analysis (TGA, TA Instruments SDT650) under a N_2 atmosphere (in a temperature range of 25 °C−1000 °C and a heating rate of 10 °C min^{-1}). To confirm the degree of chemical cross-linking, the gel content was determined using the solvent extraction method and was calculated using the following equation:

$$\frac{M_2}{M_1} \times 100\% = \text{gel content},$$

where M_1 is the weight of C-PVIm_Si and M_2 is the weight of the extracted solvent [37].

Based on American Society for Testing and Materials (ASTM) standards, several 180° peel tests were performed using a universal testing machine (UTM, Shimadzu, AGS-10kNX). The samples were measured at room temperature. (20 mn min^{-1}).

The electrodes were morphologically and electrochemically characterized using scanning electron microscopy (SEM, Hitachi Regulus 8100).

4. Electrochemical Characterization

The working electrode was prepared by mixing the electro active material (NiO, 85 wt%), carbon black (10 wt%), PVDF and PVIm_Si (5 wt%) as a binder. The prepared slurry was measured in a nickel plate electrode, and the PVDF electrode binder was dried at 120 °C for 1 h to remove the NMP. The PVIm_Si binder was manufactured by drying at 120 °C for 1 h to remove the NMP followed by drying for 1 h at 160 °C, this was the optimal cross-linking condition. The cross-linking reaction in such an electrode can be seen in Figure 2 and Figure 3.

The electrochemical performance of the NiO was evaluated using Pt foil as a counter electrode and a KOH solution (2 M) as an electrolyte. A voltage window of -0.05 to 0.4 V was observed at room temperature.

C. Results and Discussion

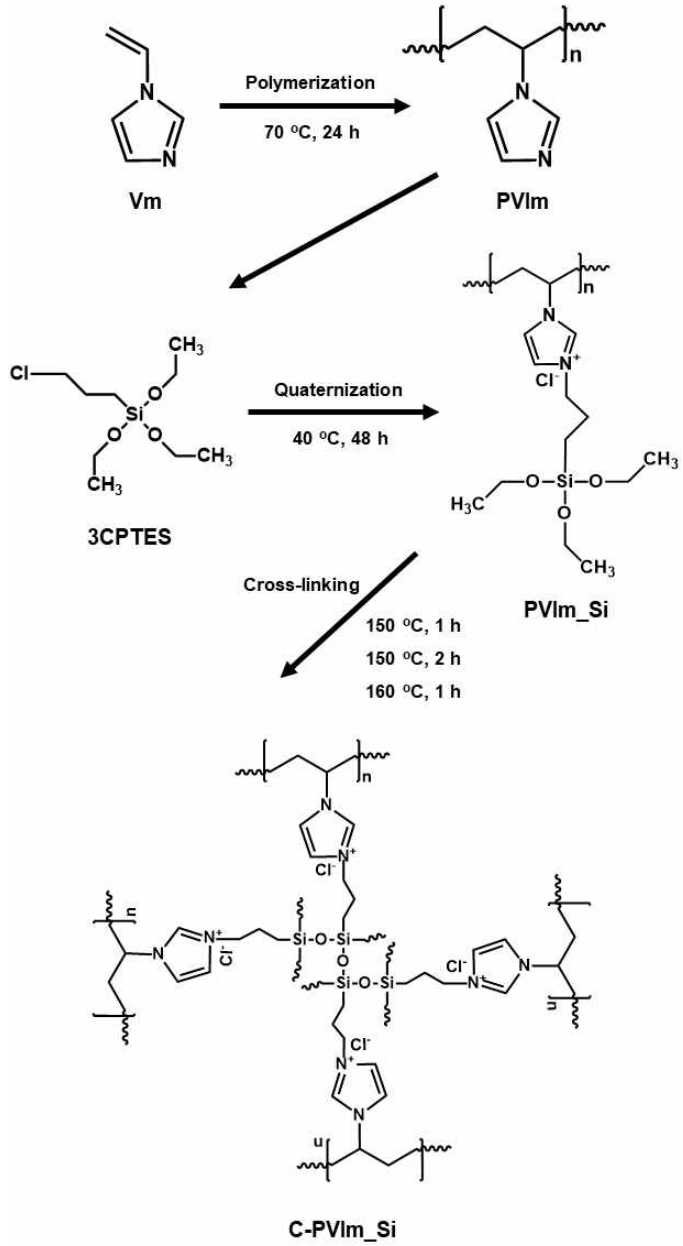

Figure 1. Schematic illustration showing synthesis of C-PVIm_Si.

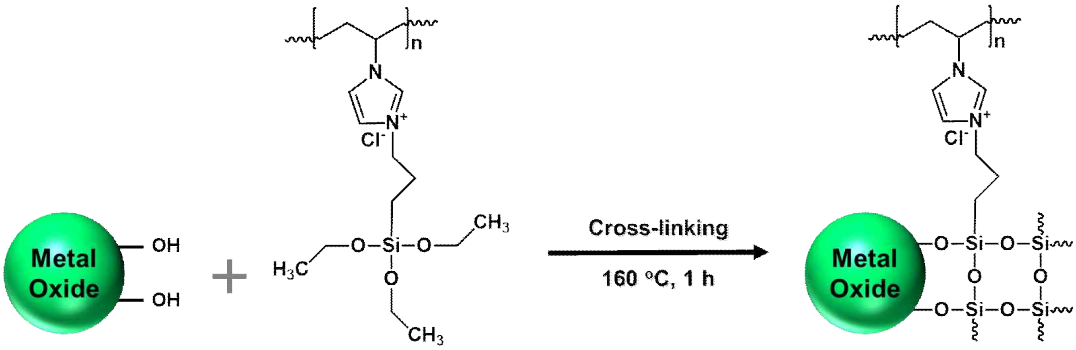

Figure 2. Schematic illustration showing reaction of NiO@C-PVIm_Si.

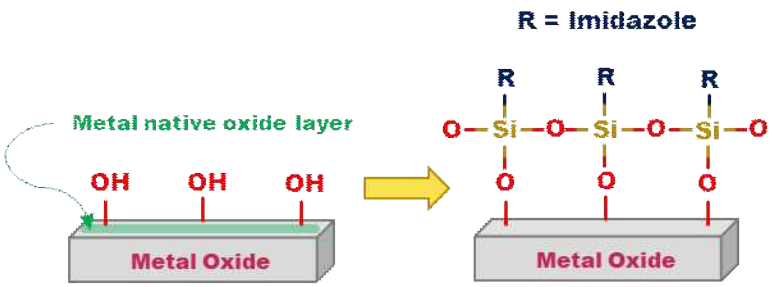

Figure 3. Schematic illustration showing metal surface reaction.

1. ^{1}H-NMR Spectra

Free radical polymerization was used to prepare PVIm using AIBN as the initiator. PVIm_Si was made from partial functionalization of PVIm with 3CPTES. The ^{1}H-NMR peaks of PVIm and 3CPTES used for quaternary substitution are shown in Figure 4. This rection proceeded smoothly owing to the weak steric hindrance and strong nucleophilicity of the 3-position nitrogen atom in the imidazole ring as well as the high reactivity of 3CPTES. Figure 5 shows the ^{1}H-NMR spectra of PVIm 50, 70, 100 in the range of 0-10 ppm with DMSO-d_6 (yellow dot) as the deuterated reagent. The peaks between 6.6 ppm (H3,4) and 7.6 ppm (H5) are assigned to proton of the imidazole ring. Meanwhile, the peaks at 1.6-2.3 ppm (H1) and 2.88-3.2 ppm (H2) correspond to protons from the polymer backbone (CH_2 and CH-). The peaks at 1.2 ppm (H6) and 3.4 ppm (H7) are ascribed to the ethyl group (CH_3, CH_2) [38, 39].

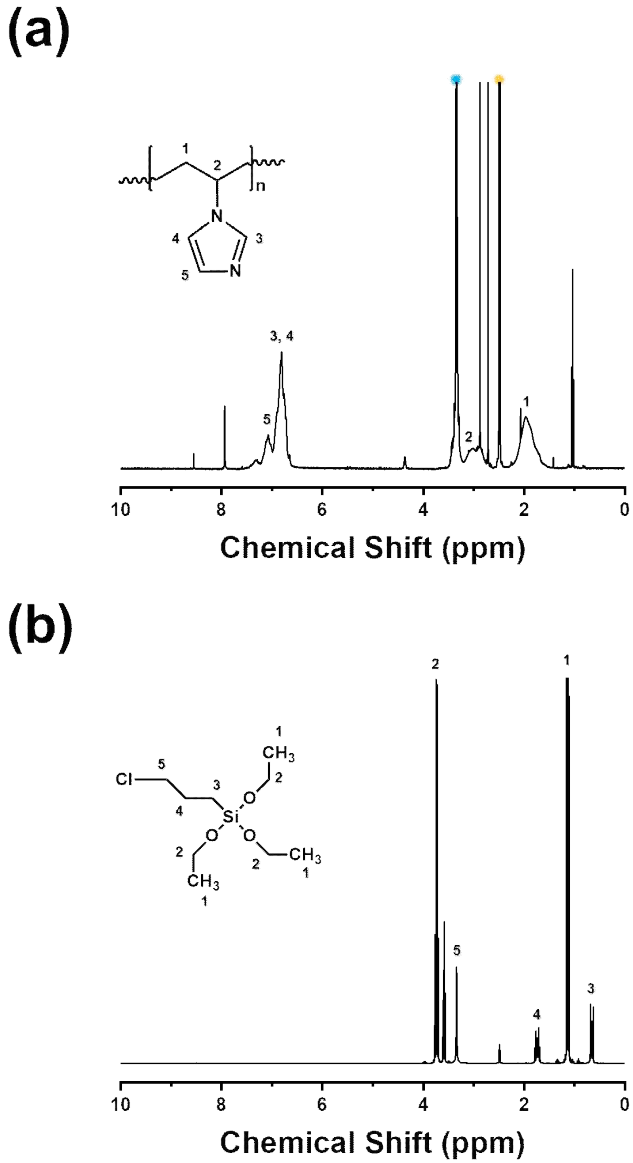

Figure 4. ^{1}H-NMR spectra of (a) PVIm; (b) 3CPTES.

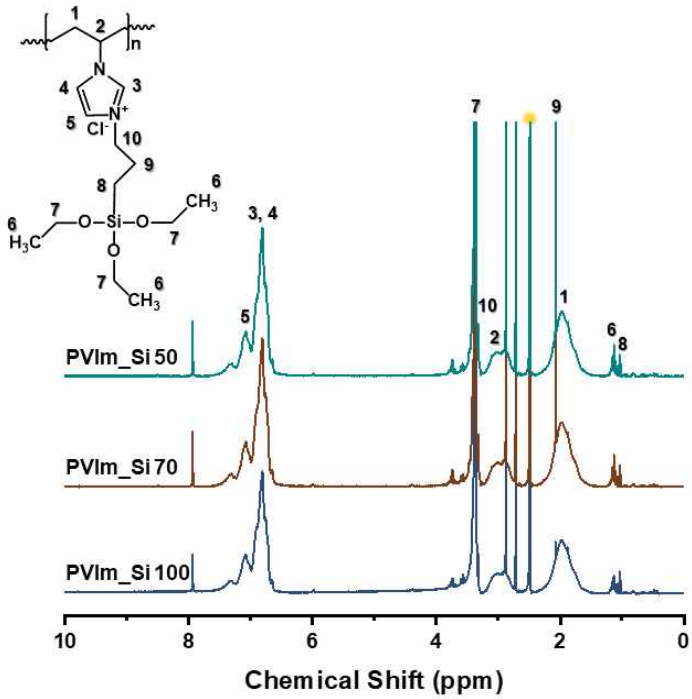

Figure 5. [1]H-NMR spectra of PVIm_Si 50, PVIm_Si 70, PVIm_Si 100.

2. FT-IR Spectra

The chemical structure of imidazolium-based binder was confirmed by FT-IR spectroscopy measurements. Figure 6 shows the FT-IR of C-PVIm_Si; the broad absorption band at approximately 3018 cm^{-1} and 2983 cm^{-1} can be attributed to the stretching vibrations of C-H (sp^2) and C-H (sp^3) groups, respectively. The peaks at 2916 cm^{-1} and 2846 cm^{-1} were attributed to the poly vinyl imidazole moieties. The peak at 1750 cm^{-1} confirmed the presence of an aromatic C=N. The peaks 1510−1276 cm^{-1} confirm the presence of the imidazole ring. The absorption bands at 1250 cm^{-1} and 1084 cm^{-1} were attributed to Si-O-Si and Si-O-C stretching [40–43].

Finally, there are indicates that the synthesis of PVIm_Si was successfully synthesized. The FT-IR peak and the corresponding functional groups of PVIm_Si are shown in Table 2 [44]. Moreover, Figure 7 displays the FT-IR spectrum of C-PVIm_Si with peaks of interest marked. In addition, the structural formula after cross-linking of NiO and PVIm_Si in Figure 2 confirmed the FT-IR peak in Figure 8.

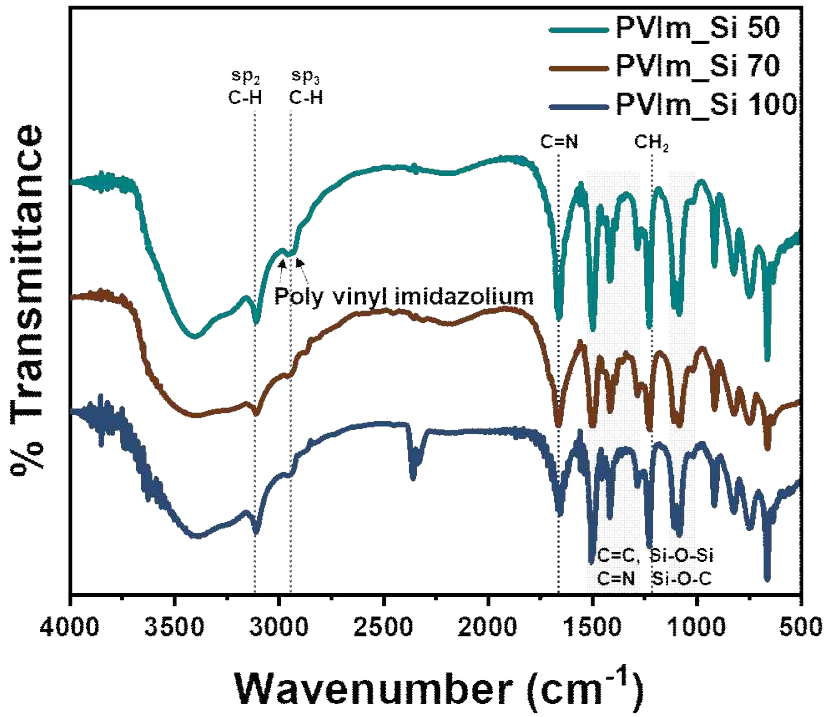

Figure 6. FT-IR spectra of PVIm_Si 50, PVIm_Si 70, PVIm_Si 100.

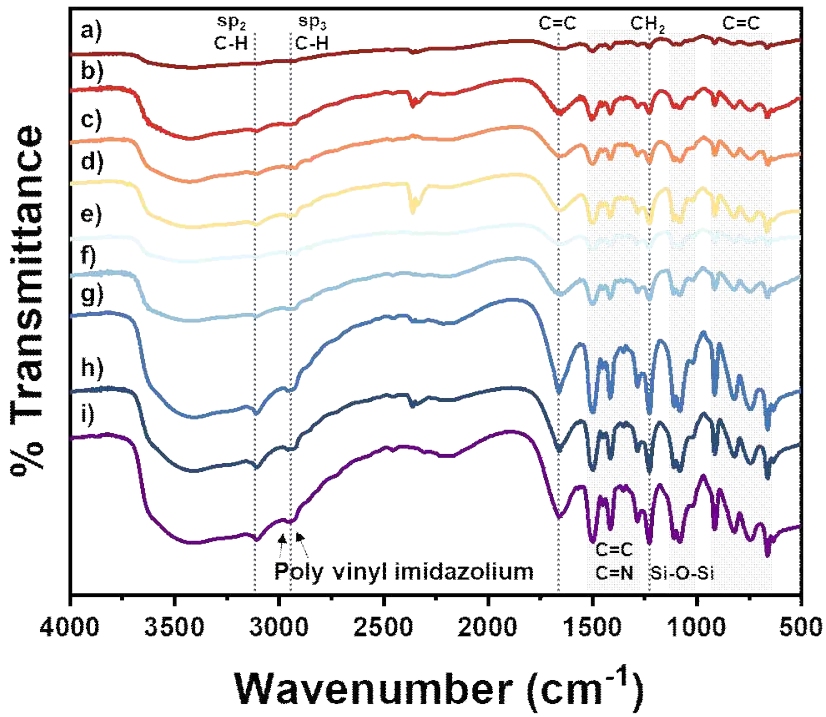

Figure 7. FT-IR spectra of C-PVIm_Si. a) C-PVIm_Si 50 (150 °C 1h); b) C-PVIm_Si 70 (150 °C 1h); c) C-PVIm_Si 100 (150 °C 1h); d) C-PVIm_Si 50 (150 °C 2h); e) C-PVIm_Si 70 (150 °C 2h); f) C-PVIm_Si 100 (150 °C 2h); g) C-PVIm_Si 50 (160 °C 1h); h) C-PVIm_Si 70 (160 °C 1h); i) C-PVIm_Si 100 (160 °C 1h).

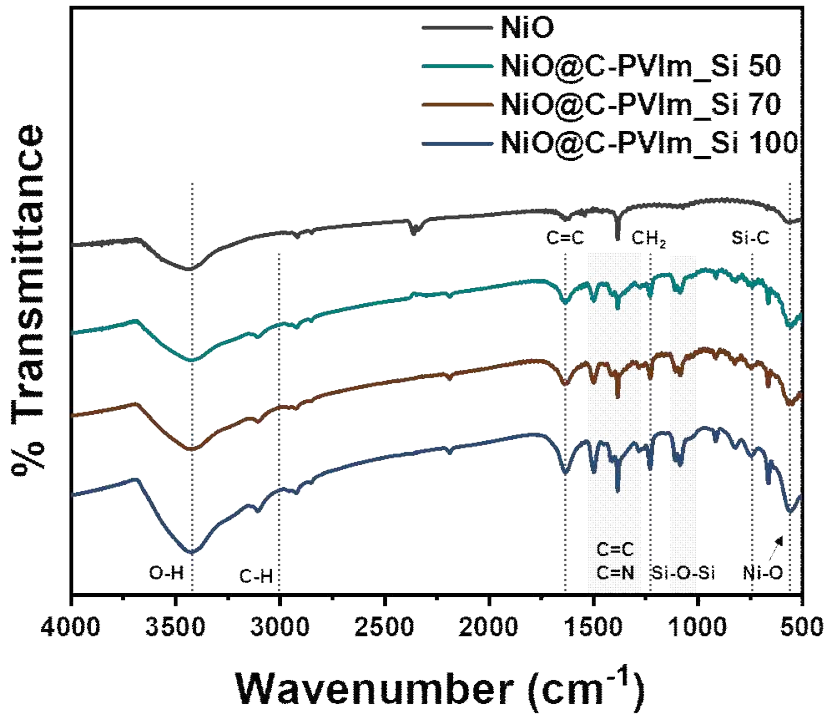

Figure 8. FT-IR spectra of NiO@C-PVIm_Si.

Table 1. List of band assignments for FT-IR spectra [40].

Wavenumber (cm^{-1})	Functional Group
3060	CH Aromatic Group
3010–3020	CH Stretching Alkene Group
3040–3060	CH of Aromatic Ring
2850–2950	CH and CH_2 Stretching Aliphatic Group
2100–2500	C=C Conjugated and C≡C
1610–1620	C=C Unsaturated Compounds
1540	C-N Amide Band
1400–1460	Stretching –C=O Inorganic Carbonate
1450–1370	CH Aliphatic Banding Group
1240–1340	C-N Amide Band
1080	C-O Carbohydrate
1020	SiO_2 Silica
875	Bending –C=O Inorganic Carbonate
690	CH Out of Plane Aromatic Band

Table 2. FT-IR spectra peak and corresponding functional groups of PVIm_Si.

Wavenumber (cm^{-1})	3200-3000	2900-2700	1750-1450	1300-1200	1250-1020
Assignment	sp^2 C-H	Sp^3 C-H	Aromatic C=C, C=N	Ring Stretching CH_2	Si-O-Si, Si-O-C

3. Gel Content Analysis

The C-PVIm_Si was prepared by thermal-induced cross-linking. It is well known that the thermal treatment of ethoxy silane group leads to the formation of insoluble cross-linked networks (Si-O-Si) in the polymer matrix. This is called a silanol reaction, and this reaction is shown in Figure 9. The gel content as a function of temperature is shown in Figure 10. The results confirm that the gel content significantly increased with increasing ratio of quaternized silane in the PVIm matrix and thermal treatment temperature up to 160 °C. Unlike other ratios of C-PVIm_Si, it can be found that 100:100 ratio of C-PVIm_Si shows about 32% gel content at 160 °C 1 hour. Through this, it was verified that, when heat treatment was performed, samples were cross-linked with each other through silanol reaction and became insoluble. On the other hand, in the molar ratio of 100:50 and 100:70 the degree of cross-linking increases as the temperature increases, but it can be seen that the molar ratio of 100:100 has the best thermal stability.

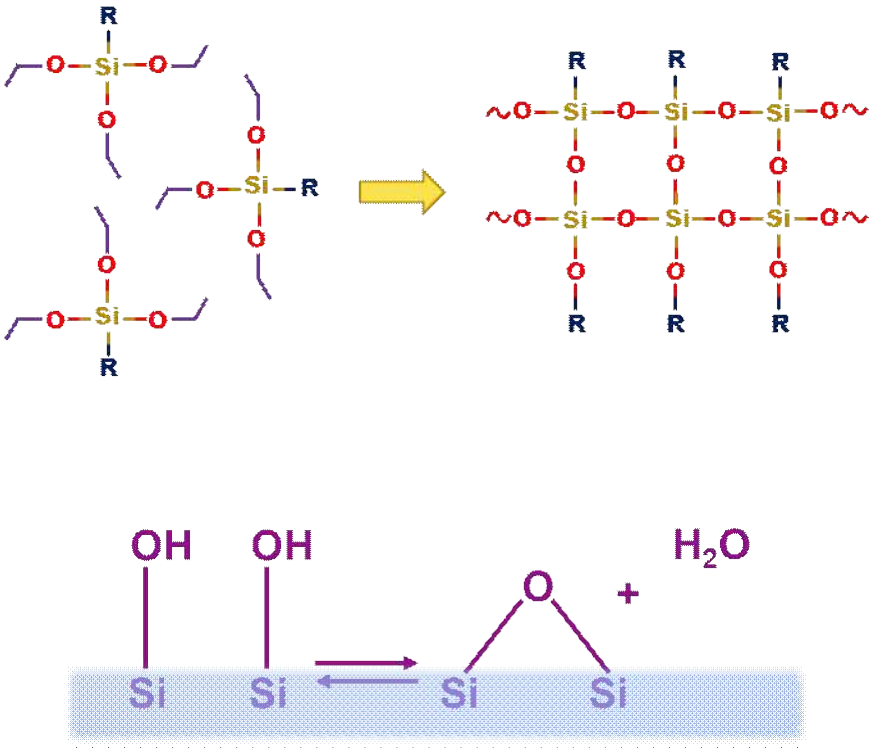

Figure 9. Schematic illustration showing silanol reaction.

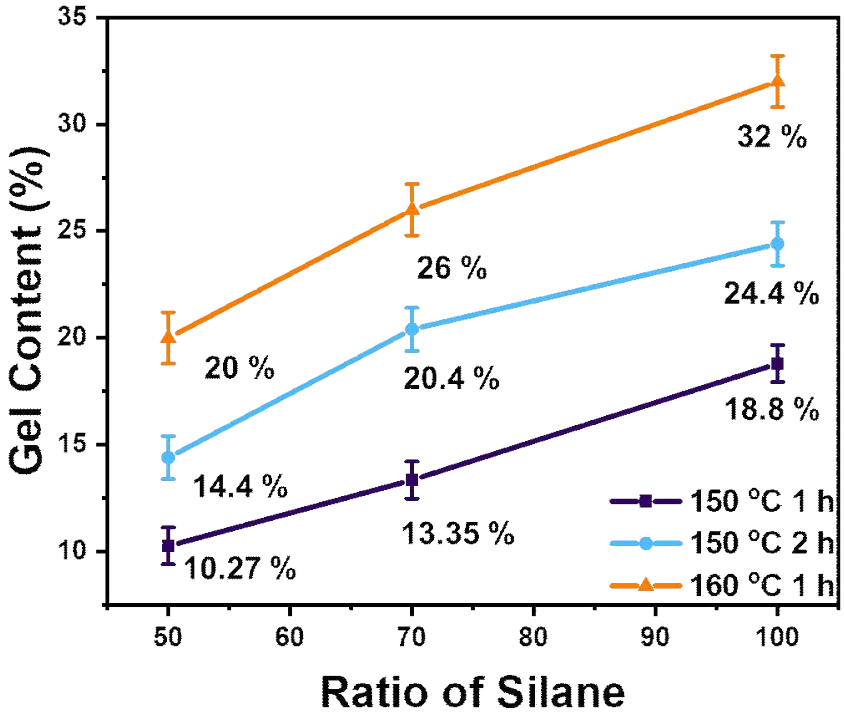

Figure 10. Gel contents of C-PVIm_Si 50, C-PVIm_Si 70, C-PVIm_Si 100.

4. TGA Curves

Excellent thermal stability is a fundamental requirement for PSEUDO in practical application. The thermal degradation behavior of the polymer binder was examined via TGA in a nitrogen atmosphere. As shown in Figure 11 a. Clearly, two degradation steps were observed for the cross-linked binders. The first degradation step from about 180 to 350 ℃ is related to the decomposition of the imidazolium groups. The degradation step above 380 ℃ is believed to be caused by the degradation of the polymer main chain. The Figure 11 b shows the final weight when the temperature is raised from room temperature to 1000 ℃. As a result, it was confirmed that the thermal stability was also improved as the ratio of silane and the temperature of cross-linking increased. Comprehensively observing Figures 10 and Figure 11, it is judged that C-PVIm_Si 100 binder is the best in condition of thermal stability. The TGA curves of the NiO@C-PVIm_Si is diplayed in Figure 12.

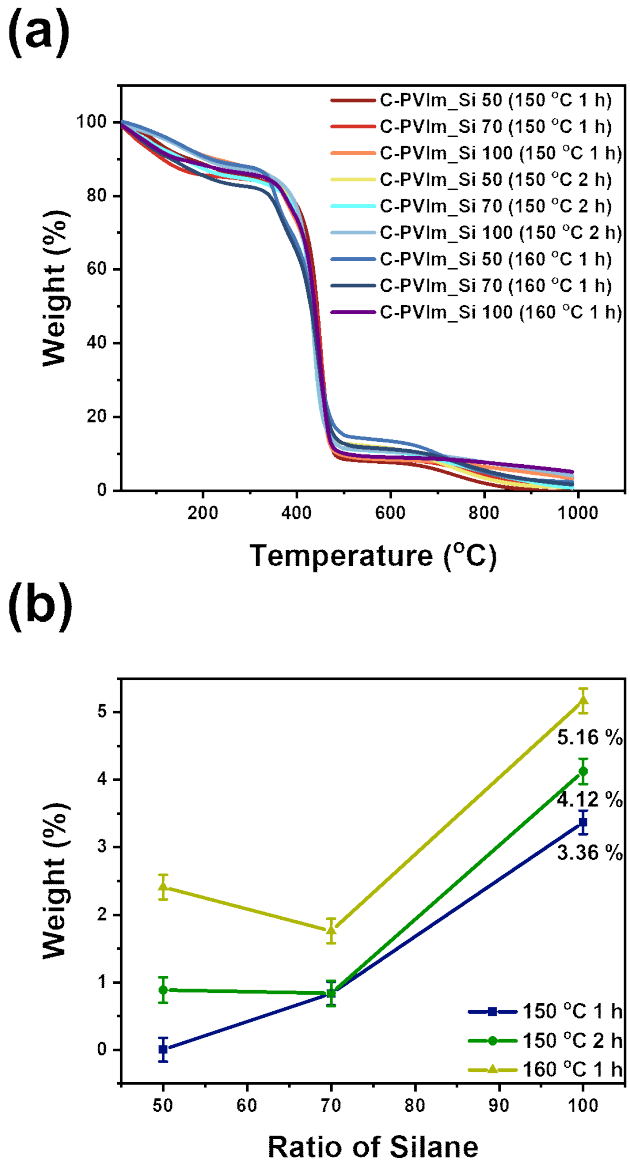

Figure 11. TGA curves of (a) C-PVIm_Si 50, C-PVIm_Si 70, C-PVIm_Si 100; (b) Final weight based on TGA.

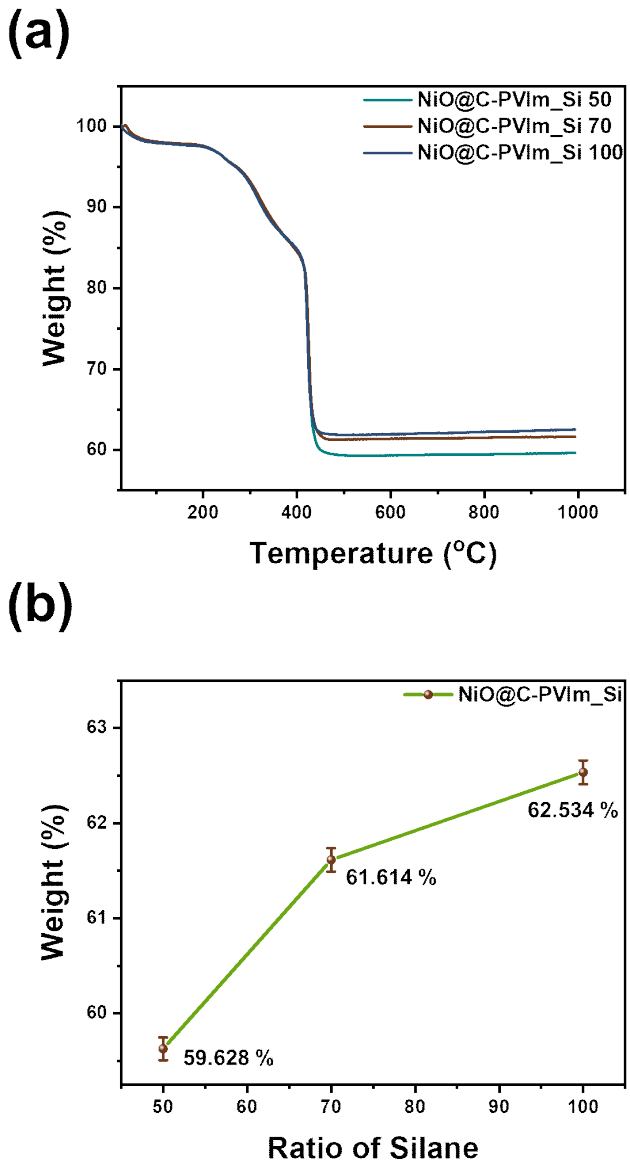

Figure 12. TGA curves of (a) NiO@C-PVIm_Si; (b) Final weight based on TGA.

5. 180° Peeling Test

The force-displacement curves of the Ni electrode as shown in Figure 13 indicate the adhesion between binder and Ni electrode. The average peeling force of C-PVIm_Si 50 (2.02 N), C-PVIm_Si 70 (3.01 N), C-PVIm_Si 100 (3.75 N) binders is also higher than that PVDF (2.54 N) binder (Figure 13 a).

In the case of PVDF binder, uneven exfoliation was shown and strength was measured low.

PVIm_Si binder, on the other hand, showed uniform exfoliation. The results of the mechanical strength analysis confirmed that PVIm_Si produced a higher load value. This is expected to result in improved adhesion to the electrode through the cross-linking of the PVIm_Si binder.

Moreover, the optical images show that when PVDF or C-PVIm_Si was used as binders, a large portion of electrode slurry was peeled off from the Ni electrode and adhered on the tape side after the peeling test (Figure 13 b) [45, 46].

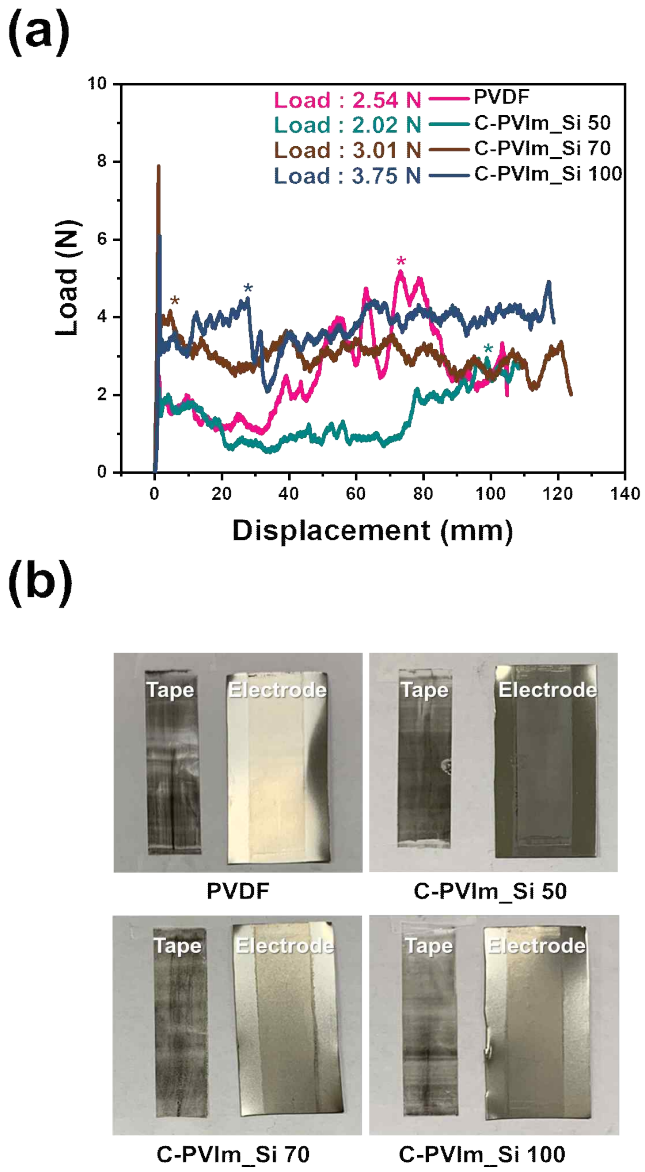

Figure 13. (a) The 180° peeling tests for the Ni electrode with different binders; (b) The optical images of the tape and electrode surface after the peel test.

6. SEM Images

Additionally, concentration of solution, temperature of solution in reactor and complexing reagent of Ni^{2+} ion are also important factors for the preparation of high density spherical $Ni(OH)_2$ with excellent performance.

In a word, concentration of the solutions, complexing reagent, feed-in velocity, intensity of agitation, temperature of reactor, and pH value of solution in reactor are important for optimizing the performance of the product in the process of controlled crystallization. The SEM image shows the external morphology of $Ni(OH)_2$ obtained through synthesis, where particles are of spherical shape (Figure 14) [47].

Porous NiO nanostructure powders were obtained by annealing as-prepared $Ni(OH)_2$ samples. After calcination, a color change from light green to gray was visualized, confirming the trnasformation of $Ni(OH)_2$ into NiO [48]. Elemental mapping by energy-dispersive X-ray spectrometry (SEM/EDS) was performed for $Ni(OH)_2$ and NiO samples. Obtained compositions from the EDS analysis of individual samples were compared to the corresponding targeted chemical phase. The obtained compositions matched well within the typical errors related to EDS analysis. A representative EDS spectrum and elemental mapping is shown in Figure 15 a–j. The obtained data suggest the homogeneous dispersion of Ni, O, in both $Ni(OH)_2$ and NiO (Figure 15 a–e, Figure 15 f–j), respectively.

Moreover, the XRD patterns of $Ni(OH)_2$ and NiO are shown in Figure 16. The XRD peaks in sky blue can be identified as those of a $Ni(OH)_2$, on the basis of the standard pattern in JCPDS card 22-044.

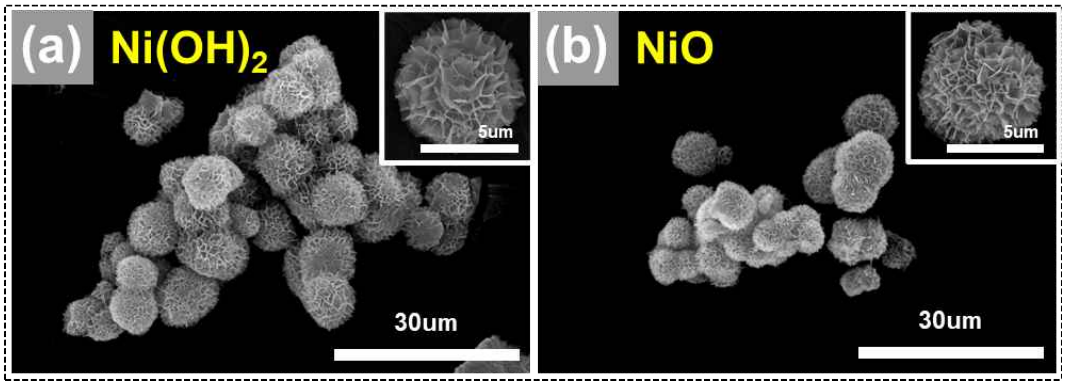

Figure 14. SEM images showing of (a) $Ni(OH)_2$; (b) NiO.

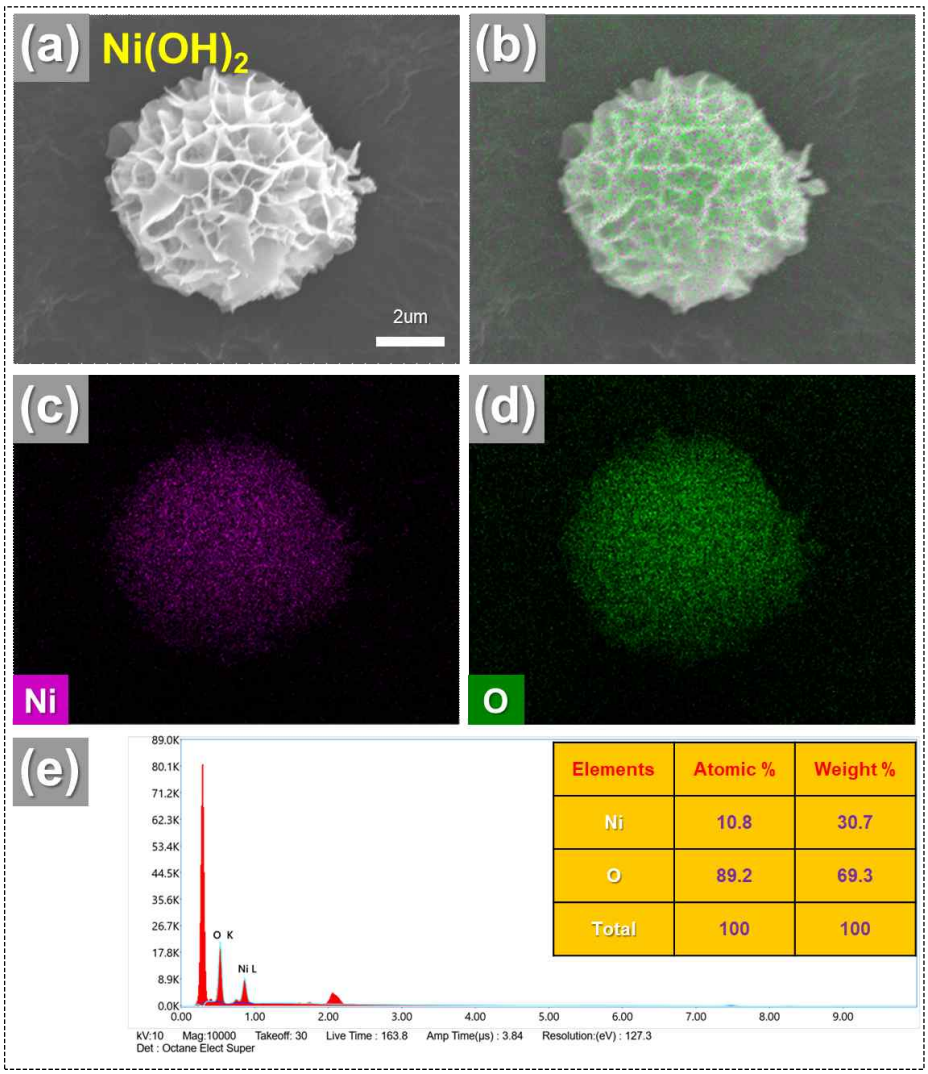

Elements	Atomic %	Weight %
Ni	10.8	30.7
O	89.2	69.3
Total	100	100

Figure 15. SEM image, energy dispersive X-ray (EDX) elemental mapping of (a)–(e) $Ni(OH)_2$.

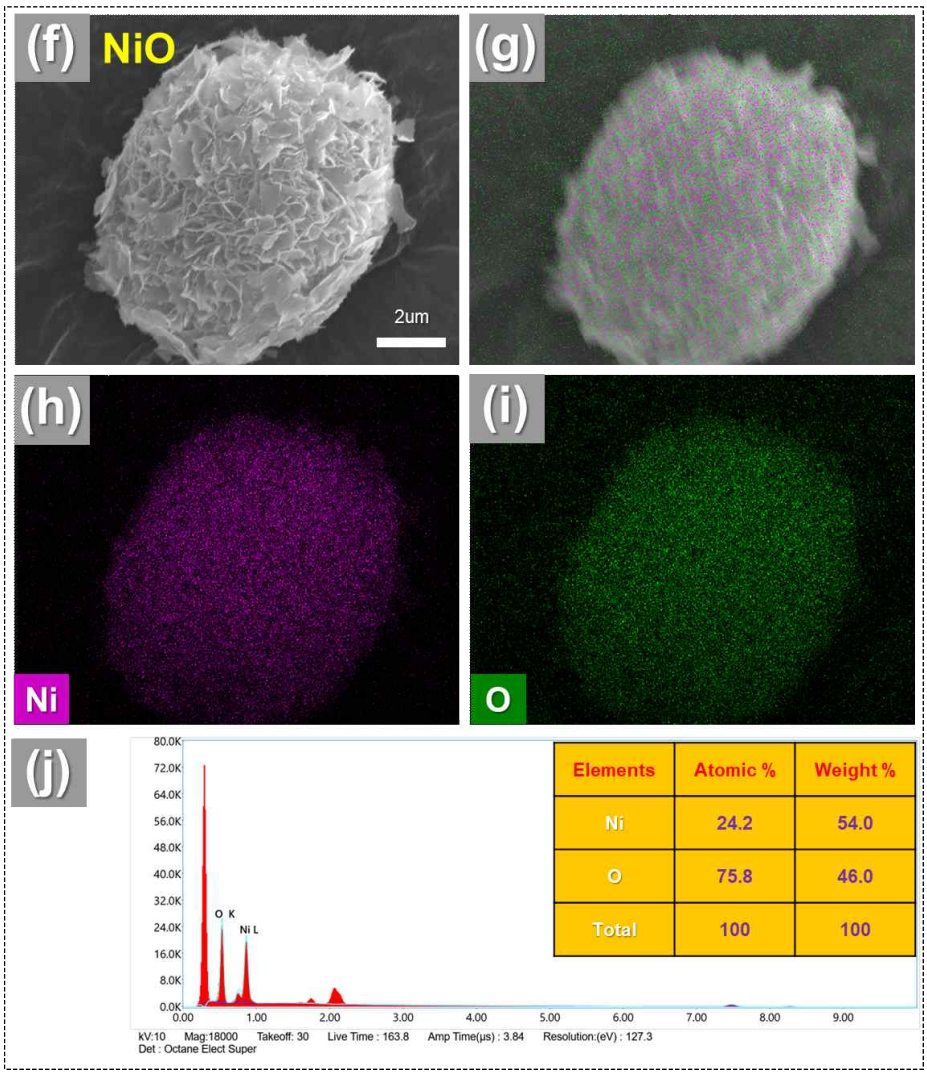

Figure 15. SEM image, energy dispersive X-ray (EDX) elemental mapping of (f)–(j) NiO.

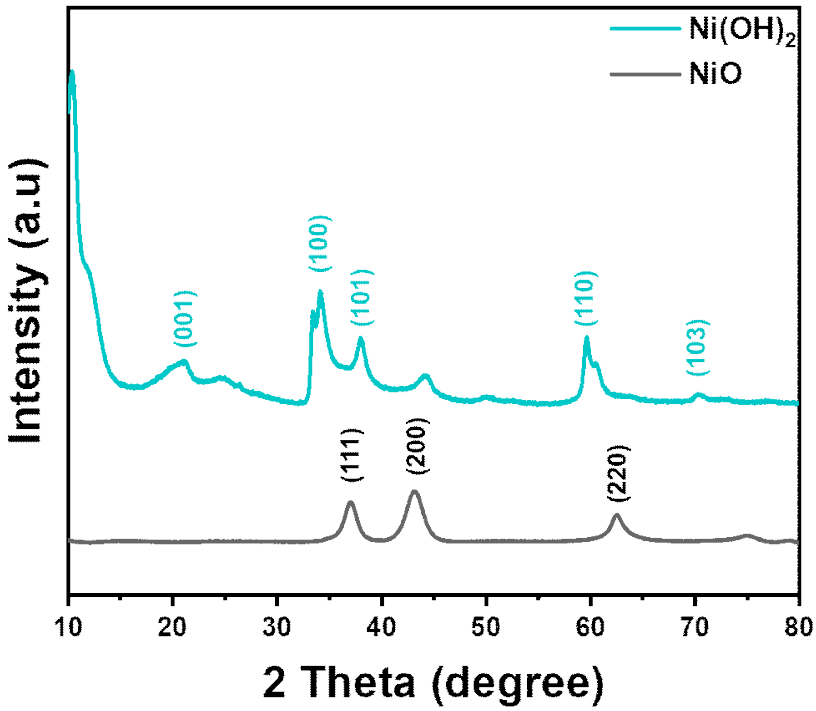

Figure 16. XRD patterns of $Ni(OH)_2$ and NiO.

7. Electrochemical Analysis

In this study, the working electrode was fabricated as shown in Figure 17. Based on this cross-linking study, the cyclic voltammogram (CV) test for NiO, the active material of supercapacitors, is shown in Figure 18 [49–51]. In order to observe the change in the CV curve of the C-PVIm_Si 100 binder, which exhibited the best physical and thermal stability, different scan rates were obtained. In the Nyquist plot (Figure 19), the impedance behaviour of the Ni electrode is portrayed and shown by a vertical line in the low-frequency region, showing ideal capacitive behavior coupled with low charge transfer resistance (Rct). Similarly, the PVDF revealed a larger semicircle than C-PVIm_Si 100.

Our binder showed higher capacity than PVDF binder (Figure 18 b). When comparing before and after cross-linking, it was confirmed that the capacity after cross-linking was significantly improved (Figure 18 c and d). It can be seen that the cross-linking rate affects the electrochemical capacity [52–55]. It is considered that the durability is improved because the binding force between the electrode and the binder is increased due to the cross-linking reaction. As a result, it was confirmed that the prepared binder showed high capacity in pseudo-capacitors and had cycle stability. Therefore, we are confident that our C-PVIm_Si binder has sufficient potential to replace the PVDF binder.

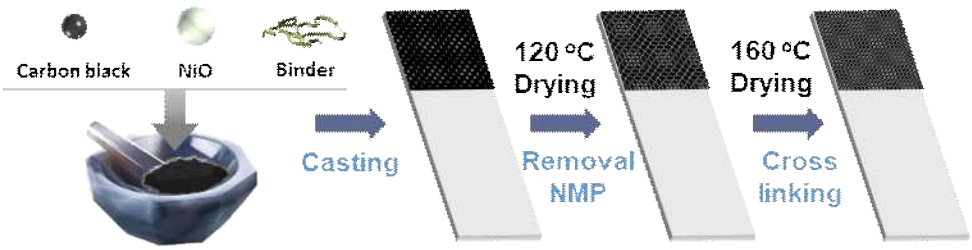

Figure 17. Schematic illustration of working electrode.

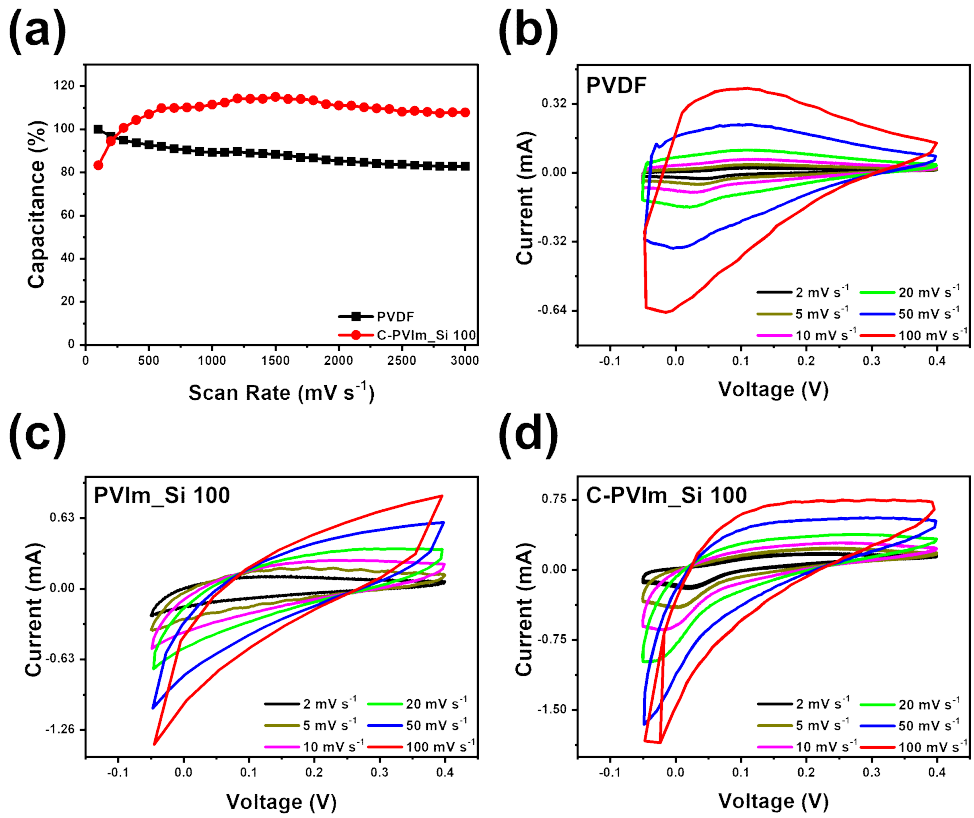

Figure 18. Cyclic voltammogram curve of (a) Cycle test; (b) PVDF; (c) PVIm_Si 100; (d) C-PVIm_Si 100.

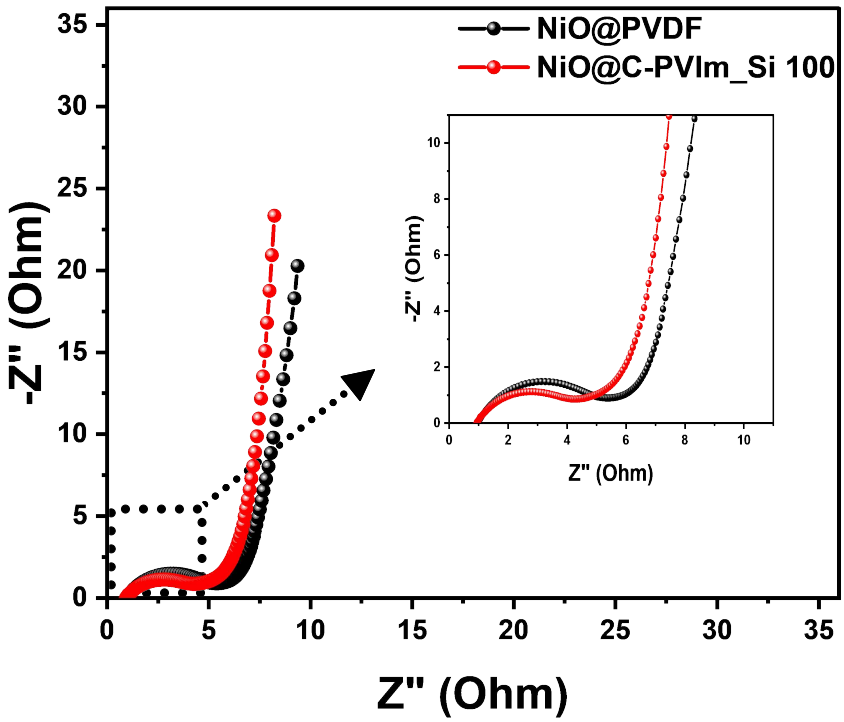

Figure 19. EIS spectra of the device showing the internal resistances NiO@PVDF and NiO@C-PVIm_Si 100.

D. Conclusion

A PVIm_Si binder was successfully synthesized to improve the cycle characteristics of PSEUDOs. This polymeric binder exhibited a strong binding ability with the electrode slurry and Ni electrode. ^{1}H-NMR and FT-IR analyses confirmed the synthesis of PVIm_Si, and the thermal stability and cross-linking degree increased as the ratio of silane increased through TGA and gel content. Additionally, a peel test was performed to confirm physical stability. Examining the electrochemical properties by manufacturing an electrode to which the C-PVIm_Si binder was applied revealed that the binding force between the electrode and binder was increased owing to the cross-linking effect. The resulting C-PVIm_Si 100 binder exhibited a better adhesion and cycle stability than the PVDF binder did. Thus, it was confirmed that the produced binder showed a high capacity in PSEUDOs and cycle stability. The C-PVIm_Si binder, which has advantages such as easy synthesis and excellent cross-linking, can be competitively used for its high adhesion and also be applied to high-capacity electrode materials other than PSEUDOs. This study revealed that cross-linked networks in functional polymers were long-cycle-life features for electrochemical redox capacitors.

Ⅴ. Summary

In this study, we fabricated functional binders exhibiting various properties. The first is an ionic liquid binder that has both a strong structure and ion conductivity by cross-linking; the second is a PAA/TAc binder that suppresses side reactions due to its radical scavenging ability in the battery; and the third is a pseudo-capacitor that improves durability. An ionic liquid binder incorporating a silanol reaction.

We conducted analysis to confirm the chemical structure, thermal stability, physical properties, and electrochemical property evaluation. All analyses showed improved characteristics compared to the existing commercially available binders, and it was verified that the electrochemical performance was improved remarkably. More importantly, our functional polymeric binder possesses a good cross-linking network structure, thereby outperforming currently used commercial binders. We expect our binders to be used in various energy storage devices, and we are expected to be the center of research and development of existing materials. In addition, our binder will serve as a starting point for spurring research on materials that have been lacking in the past.

References

[Ⅰ. Introduction]

[1] Y. Chen, Y. Kang, Y. Zhao, L. Wang, J. Liu, Y. Li, Z. Liang, X. He, X. Li, N. Tavajohi, B. Li, Journal of Energy Chemistry, 59 (2021) 83-99.

[2] A. Zecca, L. Chiari, Energy Policy, 38 (2010) 1-3.

[3] N. Shen, Y. Wang, H. Peng, Z. Hou, in Renewable Energy Green Innovation, Fossil Energy Consumption, and Air Pollution—Spatial Empirical Analysis Based on China, (2020).

[4] H. Zhao, Q. Wu, S. Hu, H. Xu, C.N. Rasmussen, Applied Energy, 137 (2015) 545-553.

[5] S. Thomas, M. Stieneker, R.W.D. Doncker, in Development of a modular high-power converter system for battery energy storage systems, pp. 1-10, (2011).

[6] B. Scrosati, Electrochimica Acta, 45 (2000) 2461-2466.

[7] P. Breeze, in Chapter 10 - Power System Energy Storage Technologies, P. Breeze Ed., pp. 219-249, Newnes, (2019).

[8] J. Castro-Gutiérrez, A. Celzard, V. Fierro, Frontiers in Materials, 7 (2020).

[9] S.C. Johnson, F. Todd Davidson, J.D. Rhodes, J.L. Coleman, S.M. Bragg-Sitton, E.J. Dufek, M.E. Webber, in Chapter Five - Selecting Favorable Energy Storage Technologies for Nuclear Power, H. Bindra, S. Revankar Eds., pp. 119-175, Academic Press, (2019).

[10] A. Yoshino, Angewandte Chemie International Edition, 51 (2012) 5798-5800.

[11] T. Wilberforce, Z. El-Hassan, F.N. Khatib, A. Al Makky, A. Baroutaji, J.G. Carton, A.G. Olabi, International Journal of Hydrogen Energy, 42 (2017) 25695-25734.

[12] B. Diouf, R. Pode, Renewable Energy, 76 (2015) 375-380.

[13] T.P. Narins, The Extractive Industries and Society, 4 (2017) 321-328.

[14] B. Frenzel, P. Kurzweil, H. Rönnebeck, Journal of Power Sources, 196 (2011) 5364-5376.

[15] F. Orecchini, A. Santiangeli, A. Dell'Era, in 10 - EVs and HEVs Using Lithium-Ion Batteries, G. Pistoia Ed., pp. 205-248, Elsevier, Amsterdam (2014).

[16] S. Zhang, K. Zhao, T. Zhu, J. Li, Progress in Materials Science, 89 (2017) 479-521.

[17] Y. Shi, X. Zhou, G. Yu, Accounts of Chemical Research, 50 (2017) 2642-2652.

[18] Y.-E. Miao, T. Liu, in Chapter 21 - Electrospun Nanofiber Electrodes: A Promising Platform for Supercapacitor Applications, B. Ding, X. Wang, J. Yu Eds., pp. 641-669, William Andrew Publishing, (2019).

[19] Y. Wang, Y. Song, Y. Xia, Chemical Society Reviews, 45 (2016) 5925-5950.

[20] S. Fleischmann, J.B. Mitchell, R. Wang, C. Zhan, D.-e. Jiang, V. Presser, V. Augustyn, Chemical Reviews, 120 (2020) 6738-6782.

[21] L. Zhou, C. Li, X. Liu, Y. Zhu, Y. Wu, T. van Ree, in 7 - Metal oxides in supercapacitors, Y. Wu Ed., pp. 169-203, Elsevier, (2018).

[22] M. Sarno, in Chapter 22 - Nanotechnology in energy storage: the supercapacitors, A. Basile, G. Centi, M.D. Falco, G. Iaquaniello Eds., pp. 431-458, Elsevier, (2020).

[23] J.-L. Shi, D.-D. Xiao, M. Ge, X. Yu, Y. Chu, X. Huang, X.-D. Zhang, Y.-X. Yin, X.-Q. Yang, Y.-G. Guo, L. Gu, L.-J. Wan, Advanced Materials, 30 (2018) 1705575.

[24] B. Xiao, X. Sun, Advanced Energy Materials, 8 (2018) 1802057.

[25] J.W. Fergus, Journal of Power Sources, 195 (2010) 939-954.

[26] C. Daniel, D. Mohanty, J. Li, D.L. Wood, AIP Conference Proceedings, 1597 (2014) 26-43.

[27] M.S. Whittingham, Chemical Reviews, 104 (2004) 4271-4302.

[28] T.R. Somo, T.E. Mabokela, D.M. Teffu, T.K. Sekgobela, B. Ramogayana, M.J. Hato, K.D. Modibane, in A Comparative Review of Metal Oxide Surface Coatings on Three Families of Cathode Materials for Lithium Ion Batteries, (2021).

[29] Y. Chen, S. Song, X. Zhang, Y. Liu, Journal of Physics: Conference Series, 1347 (2019) 012012.

[30] F. Meng, X. Xiong, L. Tan, B. Yuan, R. Hu, Energy Storage Materials, 44 (2022) 390-407.

[31] O.S. Mendoza-Hernandez, H. Ishikawa, Y. Nishikawa, Y. Maruyama, M. Umeda, Journal of Power Sources, 280 (2015) 499-504.

[32] Y. Meng, Y. Li, J. Xia, Q. Hu, X. Ke, G. Ren, F. Zhu, Applied Surface Science, 476 (2019) 761-768.

[33] A. Chakraborty, S. Kunnikuruvan, M. Dixit, D.T. Major, Israel Journal of Chemistry, 60 (2020) 850-862.

[34] A. Purwanto, C.S. Yudha, U. Ubaidillah, H. Widiyandari, T. Ogi, H. Haerudin, Materials Research Express, 5 (2018) 122001.

[35] H. Zhang, Y. Yang, D. Ren, L. Wang, X. He, Energy Storage Materials, 36 (2021) 147-170.

[36] M. Yoshio, H. Wang, K. Fukuda, Angewandte Chemie International Edition, 42 (2003) 4203-4206.

[37] L. Li, D. Zhang, J. Deng, Y. Gou, J. Fang, H. Cui, Y. Zhao, M. Cao, Carbon, 183 (2021) 721-734.

[38] in Chapter 7 - Lithium-Secondary Cell: Sources of Risks and Their Effects, J. Garche, K. Brandt Eds., pp. 143-266, Elsevier, (2019).

[39] Y.-Y. Hu, Z. Liu, K.-W. Nam, O.J. Borkiewicz, J. Cheng, X. Hua, M.T. Dunstan, X. Yu, K.M. Wiaderek, L.-S. Du, K.W. Chapman, P.J. Chupas, X.-Q. Yang, C.P. Grey, Nature Materials, 12 (2013) 1130-1136.

[40] W.-R. Liu, Z.-Z. Guo, W.-S. Young, D.-T. Shieh, H.-C. Wu, M.-H. Yang, N.-L. Wu, Journal of Power Sources, 140 (2005) 139-144.

[41] E. Kamali-Heidari, A. Kamyabi-Gol, M. Heydarzadeh sohi, A. Ataie, Journal of Ultrafine Grained and Nanostructured Materials, 51 (2018) 1-12.

[42] M.C. Buzzeo, C. Hardacre, R.G. Compton, ChemPhysChem, 7 (2006) 176-180.

[43] B. Garcia, S. Lavallée, G. Perron, C. Michot, M. Armand, Electrochimica Acta, 49 (2004) 4583-4588.

[44] X.-B. Cheng, C.-Z. Zhao, Y.-X. Yao, H. Liu, Q. Zhang, Chem, 5 (2019) 74-96.

[45] Y.-S. Ye, J. Rick, B.-J. Hwang, Journal of Materials Chemistry A, 1 (2013) 2719-2743.

[46] A. Fernicola, B. Scrosati, H. Ohno, Ionics, 12 (2006) 95-102.

[47] N. Chapman, O. Borodin, T. Yoon, C.C. Nguyen, B.L. Lucht, The Journal of Physical Chemistry C, 121 (2017) 2135-2148.

[48] J. Ryu, S. Kim, J. Kim, S. Park, S. Lee, S. Yoo, J. Kim, N.-S. Choi, J.-H. Ryu, S. Park, Advanced Functional Materials, 30 (2020) 1908433.

[49] S.-L. Chou, Y. Pan, J.-Z. Wang, H.-K. Liu, S.-X. Dou, Physical Chemistry Chemical Physics, 16 (2014) 20347-20359.

[50] Y.-M. Zhao, F.-S. Yue, S.-C. Li, Y. Zhang, Z.-R. Tian, Q. Xu, S. Xin, Y.-G. Guo, InfoMat, 3 (2021) 460-501.

[51] J.-T. Li, Z.-Y. Wu, Y.-Q. Lu, Y. Zhou, Q.-S. Huang, L. Huang, S.-G. Sun, Advanced Energy Materials, 7 (2017) 1701185.

[52] A. Cholewinski, P. Si, M. Uceda, M. Pope, B. Zhao, in Polymer Binders: Characterization and Development toward Aqueous Electrode Fabrication for Sustainability, (2021).

[53] H.A.N.W.-Q. Guo Rong-Nan, Journal of Inorganic Materials, 34 (2019) 1021-1029.

[54] S.S. Zhang, T.R. Jow, Journal of Power Sources, 109 (2002) 422-426.

[55] Y. Wang, H. Zheng, Q. Qu, L. Zhang, V.S. Battaglia, H. Zheng, Carbon, 92 (2015) 318-326.

[56] H. Chen, M. Ling, L. Hencz, H.Y. Ling, G. Li, Z. Lin, G. Liu, S. Zhang, Chemical Reviews, 118 (2018) 8936-8982.

[57] A.M. Haregewoin, A.S. Wotango, B.-J. Hwang, Energy & Environmental Science, 9 (2016) 1955-1988.

[58] A. Wang, S. Kadam, H. Li, S. Shi, Y. Qi, npj Computational Materials, 4 (2018) 15.

[59] S.J. An, J. Li, C. Daniel, D. Mohanty, S. Nagpure, D.L. Wood, Carbon, 105 (2016) 52-76.

[60] S. Phul, A. Deshpande, B. Krishnamurthy, Electrochimica Acta, 164 (2015) 281-287.

[61] Y.-S. Park, E.-S. Oh, S.-M. Lee, Journal of Power Sources, 248 (2014) 1191-1196.

[62] D. Shin, H. Park, U. Paik, Electrochemistry Communications, 77 (2017) 103-106.

[63] Chemical Reviews, 117 (2017) 6633-6635.

[64] Q. Zhao, J.L. Anderson, in 2.11 - Ionic Liquids, J. Pawliszyn Ed., pp. 213-242, Academic Press, Oxford (2012).

[65] N. Gupta, Y.N. Liang, X. Hu, Current Opinion in Chemical Engineering, 25 (2019) 43-50.

[66] H. Chen, Z. Wang, X. Xu, S. Gong, Y. Zhou, Physical Chemistry Chemical Physics, 23 (2021) 13300-13309.

[67] N. Delgado-Mellado, A. Ovejero-Perez, P. Navarro, M. Larriba, M. Ayuso, J. García, F. Rodríguez, The Journal of Chemical Thermodynamics, 131 (2019) 340-346.

[68] Y. Assadi, M.A. Farajzadeh, A. Bidari, in 2.10 - Dispersive Liquid−Liquid Microextraction, J. Pawliszyn Ed., pp. 181-212, Academic Press, Oxford (2012).

[69] H. Jia, X. Cao, J.-G. Zhang, W. Xu, in Electrolytes for Lithium-Ion and Lithium Metal Batteries, L.F. Cabeza Ed., pp. 108-122, Elsevier, Oxford (2022).

[70] R. Marcilla, J. Alberto Blazquez, J. Rodriguez, J.A. Pomposo, D. Mecerreyes, Journal of Polymer Science Part A: Polymer Chemistry, 42 (2004) 208-212.

[71] K. Liu, W. Liu, Y. Qiu, B. Kong, Y. Sun, Z. Chen, D. Zhuo, D. Lin, Y. Cui, Science Advances, 3 e1601978.

[72] J. Yuan, D. Mecerreyes, M. Antonietti, Progress in Polymer Science, 38 (2013) 1009-1036.

[73] S.-Y. Zhang, Q. Zhuang, M. Zhang, H. Wang, Z. Gao, J.-K. Sun, J. Yuan, Chemical Society Reviews, 49 (2020) 1726-1755.

[74] A.S. Shaplov, D.O. Ponkratov, Y.S. Vygodskii, Polymer Science Series B, 58

(2016) 73-142.

[75] H. Minami, Langmuir, 36 (2020) 8668-8679.

[76] S. Ravula, K.E. O'Harra, K.A. Watson, J.E. Bara, in Poly(ionic liquid)s with Dicationic Pendants as Gas Separation Membranes, (2022).

[77] H. Cheng, P. Wang, J. Luo, J. Fransaer, D.E. De Vos, Z.-H. Luo, Industrial & Engineering Chemistry Research, 54 (2015) 3107-3115.

[78] H. Lin, S. Zhang, J.-K. Sun, M. Antonietti, J. Yuan, Polymer, 202 (2020) 122640.

[79] F. Yang, Q. Liu, W. Xie, P. Xie, J. Shang, X. Shu, in High-Content Lithium Aluminum Titanium Phosphate-Based Composite Solid Electrolyte with Poly(ionic liquid) Binder, (2022).

[80] X. Tang, S. Lv, K. Jiang, G. Zhou, X. Liu, Journal of Power Sources, 542 (2022) 231792.

[81] R. Jamil, D.S. Silvester, Current Opinion in Electrochemistry, 35 (2022) 101046.

[Ⅱ. Dual Effect-Assisted Polymer Binder of LIBs]

[1] M. Wu, X. Xiao, N. Vukmirovic, S. Xun, P.K. Das, X. Song, P. Olalde-Velasco, D. Wang, A.Z. Weber, L.-W. Wang, V.S. Battaglia, W. Yang, G. Liu, Journal of the American Chemical Society, 135 (2013) 12048-12056.

[2] M.M. Thackeray, C. Wolverton, E.D. Isaacs, Energy & Environmental Science, 5 (2012) 7854-7863.

[3] M. Armand, J.M. Tarascon, Nature, 451 (2008) 652-657.

[4] A. Cholewinski, P. Si, M. Uceda, M. Pope, B. Zhao, Polymers, 13 (2021) 631.

[5] J. Liu, Q. Zhang, Y.-K. Sun, Journal of Power Sources, 396 (2018) 19-32.

[6] H. Chen, M. Ling, L. Hencz, H.Y. Ling, G. Li, Z. Lin, G. Liu, S. Zhang, Chemical Reviews, 118 (2018) 8936-8982.

[7] A. Miranda, K. Sarang, B. Gendensuren, E.-S. Oh, J. Lutkenhaus, R. Verduzco, Molecular Systems Design & Engineering, 5 (2020) 709-724.

[8] Y. Shi, X. Zhou, G. Yu, Accounts of Chemical Research, 50 (2017) 2642-2652.

[9] D. Bresser, D. Buchholz, A. Moretti, A. Varzi, S. Passerini, Energy & Environmental Science, 11 (2018) 3096-3127.

[10] S.K. Heiskanen, J. Kim, B.L. Lucht, Joule, 3 (2019) 2322-2333.

[11] R. Fong, U. von Sacken, J.R. Dahn, Journal of The Electrochemical Society, 137 (1990) 2009-2013.

[12] P. Verma, P. Maire, P. Novák, Electrochimica Acta, 55 (2010) 6332-6341.

[13] K.H. Kim, J.H. Cho, J.U. Hwang, J.S. Im, Y.-S. Lee, Journal of Industrial and Engineering Chemistry, 99 (2021) 48-54.

[14] S. Chen, J. Zheng, L. Yu, X. Ren, M.H. Engelhard, C. Niu, H. Lee, W. Xu, J. Xiao, J. Liu, J.-G. Zhang, Joule, 2 (2018) 1548-1558.

[15] Z. Hu, S. Zhang, S. Dong, W. Li, H. Li, G. Cui, L. Chen, Chemistry of Materials, 29 (2017) 4682-4689.

[16] H. Zheng, R. Yang, G. Liu, X. Song, V.S. Battaglia, The Journal of Physical Chemistry C, 116 (2012) 4875-4882.

[17] P. Periasamy, K. Tatsumi, M. Shikano, T. Fujieda, Y. Saito, T. Sakai, M. Mizuhata, A. Kajinami, S. Deki, Journal of Power Sources, 88 (2000) 269-273.

[18] A. Magistris, P. Mustarelli, F. Parazzoli, E. Quartarone, P. Piaggio, A. Bottino, Journal of Power Sources, 97-98 (2001) 657-660.

[19] J. Chen, J. Liu, Y. Qi, T. Sun, X. Li, Journal of The Electrochemical Society, 160 (2013) A1502-A1509.

[20] M.M. Loghavi, S. Bahadorikhalili, N. Lari, M.H. Moghim, M. Babaiee, R. Eqra, Zeitschrift für Physikalische Chemie, 234 (2020) 381-397.

[21] V.A. Nguyen, C. Kuss, Journal of The Electrochemical Society, 167 (2020) 065501.

[22] J. Zhao, X. Yang, Y. Yao, Y. Gao, Y. Sui, B. Zou, H. Ehrenberg, G. Chen, F. Du, Advanced Science, 5 (2018) 1700768.

[23] J. Yuan, D. Mecerreyes, M. Antonietti, Progress in Polymer Science, 38 (2013) 1009-1036.

[24] J. Yuan, M. Antonietti, Polymer, 52 (2011) 1469-1482.

[25] W. Qian, J. Texter, F. Yan, Chemical Society Reviews, 46 (2017) 1124-1159.

[26] G. Gebresilassie Eshetu, M. Armand, B. Scrosati, S. Passerini, Angewandte Chemie International Edition, 53 (2014) 13342-13359.

[27] M. Armand, F. Endres, D.R. MacFarlane, H. Ohno, B. Scrosati, Nature Materials, 8 (2009) 621-629.

[28] I. Spanos, S. Neugebauer, R. Guterman, J. Yuan, R. Schlögl, M. Antonietti, Sustainable Energy & Fuels, 2 (2018) 1446-1451.

[29] T.P. Jayakumar, R. Badam, N. Matsumi, ACS Applied Energy Materials, 3 (2020) 3337-3346.

[30] J.-S. Lee, K. Sakaushi, M. Antonietti, J. Yuan, RSC Advances, 5 (2015) 85517-85522.

[31] L.E. Nielsen, Journal of Macromolecular Science, Part C, 3 (1969) 69-103.

[32] J. Lopez, Z. Chen, C. Wang, S.C. Andrews, Y. Cui, Z. Bao, ACS Applied Materials & Interfaces, 8 (2016) 2318-2324.

[33] R. Rohan, T.-C. Kuo, C.-Y. Chiou, Y.-L. Chang, C.-C. Li, J.-T. Lee, Journal of Power Sources, 396 (2018) 459-466.

[34] J. Yuan, S. Prescher, K. Sakaushi, M. Antonietti, Journal of Materials Chemistry A, 3 (2015) 7229-7234.

[35] W.-F. Ren, J.-B. Le, J.-T. Li, Y.-Y. Hu, S.-Y. Pan, L. Deng, Y. Zhou, L. Huang, S.-G. Sun, ACS Applied Materials & Interfaces, 13 (2021) 639-649.

[36] S. Lim, K. Lee, I. Shin, A. Tron, J. Mun, T. Yim, T.-H. Kim, Journal of Power Sources, 360 (2017) 585-592.

[37] Z.H. Xie, M.Z. Rong, M.Q. Zhang, ACS Applied Materials & Interfaces, 13 (2021) 28737-28748.

[38] T.-w. Kwon, Y.K. Jeong, E. Deniz, S.Y. AlQaradawi, J.W. Choi, A. Coskun, ACS Nano, 9 (2015) 11317-11324.

[39] J.-S. Lee, C.-H. Jung, S.-Y. Jo, J.-H. Choi, I.-T. Hwang, Y.-C. Nho, Y.-M. Lee, J.-S. Lee, Journal of Polymer Science Part A: Polymer Chemistry, 48 (2010) 2725-2731.

[40] X.L. Huang, C.X. Lin, E.N. Hu, F. Soyekwo, Q.G. Zhang, A.M. Zhu, Q.L. Liu, RSC Advances, 7 (2017) 27342-27353.

[41] C. Zhou, H. Song, F. Zhang, J. Liu, J. Li, B. Liu, J. Liang, Polymer Bulletin, 76 (2019) 5433-5449.

[42] D. Guo, Y.Z. Zhuo, A.N. Lai, Q.G. Zhang, A.M. Zhu, Q.L. Liu, Journal of Membrane Science, 518 (2016) 295-304.

[43] H. El-Hamshary, M.M.G. Fouda, M. Moydeen, M.H. El-Newehy, S.S. Al-Deyab, A. Abdel-Megeed, International Journal of Biological Macromolecules, 72 (2015) 1466-1472.

[44] Z. Sekhavat Pour, M. Ghaemy, RSC Advances, 5 (2015) 64106-64118.

[45] A. Sengupta, S. Kumar Ethirajan, M. Kamaz, M. Jebur, R. Wickramasinghe, Separation and Purification Technology, 212 (2019) 307-315.

[46] T. Feng, B. Lin, S. Zhang, N. Yuan, F. Chu, M.A. Hickner, C. Wang, L. Zhu, J. Ding, Journal of Membrane Science, 508 (2016) 7-14.

[47] S. Yurdakul, B. Gürel, M. Varol, H. Gürbüz, K. Kurtuluş, Environmental Science and Pollution Research, 28 (2021) 63894-63904.

[48] N. Shimoi, M. Komatsu, Y. Tanaka, Coatings, 9 (2019) 732.

[49] Z.-Y. Wu, Y.-Q. Lu, J.-T. Li, S. Zanna, A. Seyeux, L. Huang, S.-G. Sun, P. Marcus, J. Światowska, ACS Omega, 6 (2021) 27335-27350.

[50] J.-i. Yamaki, S.-i. Tobishima, K. Hayashi, S. Keiichi, Y. Nemoto, M. Arakawa, Journal of Power Sources, 74 (1998) 219-227.

[51] Z.-i. Takehara, Journal of Power Sources, 68 (1997) 82-86.

[52] D. Luo, L. Zheng, Z. Zhang, M. Li, Z. Chen, R. Cui, Y. Shen, G. Li, R. Feng, S. Zhang, G. Jiang, L. Chen, A. Yu, X. Wang, Nature Communications, 12 (2021) 186.

[53] F. Ding, W. Xu, X. Chen, J. Zhang, M.H. Engelhard, Y. Zhang, B.R. Johnson, J.V. Crum, T.A. Blake, X. Liu, J.-G. Zhang, Journal of The Electrochemical Society, 160 (2013) A1894-A1901.

[54] K.N. Wood, G. Teeter, ACS Applied Energy Materials, 1 (2018) 4493-4504.

[55] K.T. Sarang, X. Li, A. Miranda, T. Terlier, E.-S. Oh, R. Verduzco, J.L. Lutkenhaus, ACS Applied Energy Materials, 3 (2020) 6985-6994.

[56] A.R. Kamali, H.-K. Kim, K.-B. Kim, R. Vasant Kumar, D.J. Fray, Journal of Materials Chemistry A, 5 (2017) 19126-19135.

[57] Y. Zheng, R. Zhang, P. Vanaphuti, J. Fu, Z. Yang, Y. Wang, ACS Sustainable Chemistry & Engineering, 9 (2021) 6087-6096.

[58] G. Yang, Z. Yan, L. Cui, Y. Qu, Q. Li, X. Li, Y. Wang, H. Wang, RSC Advances, 8 (2018) 15427-15435.

[59] Q.T. Wang, R.R. Li, X.Z. Zhou, J. Li, Z.Q. Lei, Journal of Solid State Electrochemistry, 20 (2016) 1331-1336.

[60] N.-L. Wu, Y.-T. Weng, F.-S. Li, N.-H. Yang, C.-L. Kuo, D.-S. Li, Progress in Natural Science: Materials International, 25 (2015) 563-571.

[Ⅲ. Radical Scavenging and Robust Polymer Binder]

[1] M. Cropper, C. Griffiths, Am. Econ. Rev., 84 (1994) 250-254.

[2] I. IEA, IEA publication, (2013).

[3] M. Höök, X. Tang, Energy Policy, 52 (2013) 797-809.

[4] T. Bhattacharya, T. Narayan, S. Chakraborty, S. Konar, S. Singh, IJITEE, 9 (2020) 1426-1431.

[5] N. Hajilary, M. Rezakazemi, A. Shahi, Mater. Sci. Technol., 3 (2020) 218-224.

[6] A. Roy, T. Bhattacharya, M. Kumari, Sci. Total Environ., 722 (2020) 137622.

[7] J. Rogelj, A. Popp, K.V. Calvin, G. Luderer, J. Emmerling, D. Gernaat, S. Fujimori, J. Strefler, T. Hasegawa, G. Marangoni, Nat. Clim. Change, 8 (2018) 325-332.

[8] H. Lund, energy, 32 (2007) 912-919.

[9] C. Liu, F. Li, L.P. Ma, H.M. Cheng, Adv. Mater., 22 (2010) E28-E62.

[10] F.M. Orr, Jr., SPE Journal, 23 (2018) 2444-2455.

[11] F. Wang, J.D. Harindintwali, Z. Yuan, M. Wang, F. Wang, S. Li, Z. Yin, L. Huang, Y. Fu, L. Li, S.X. Chang, L. Zhang, J. Rinklebe, Z. Yuan, Q. Zhu, L. Xiang, D.C.W. Tsang, L. Xu, X. Jiang, J. Liu, N. Wei, M. Kästner, Y. Zou, Y.S. Ok, J. Shen, D. Peng, W. Zhang, D. Barceló, Y. Zhou, Z. Bai, B. Li, B. Zhang, K. Wei, H. Cao, Z. Tan, L.-b. Zhao, X. He, J. Zheng, N. Bolan, X. Liu, C. Huang, S. Dietmann, M. Luo, N. Sun, J. Gong, Y. Gong, F. Brahushi, T. Zhang, C. Xiao, X. Li, W. Chen,

N. Jiao, J. Lehmann, Y.-G. Zhu, H. Jin, A. Schäffer, J.M. Tiedje, J.M. Chen, Innovations, 2 (2021) 100180.

[12] M. Gavrilescu, Environ. Eng. Manag. J., 7 (2008).

[13] A. Kumar, T. Bhattacharya, S.M. Mozammil Hasnain, A. Kumar Nayak, M.S. Hasnain, Mater. Sci. Technol., 3 (2020) 905-920.

[14] A.Z. Al Shaqsi, K. Sopian, A. Al-Hinai, Energy Rep., 6 (2020) 288-306.

[15] J.-K. Kim, F. Mueller, H. Kim, S. Jeong, J.-S. Park, S. Passerini, Y. Kim, ChemSusChem, 9 (2016) 42-49.

[16] Y. Chen, Y. Kang, Y. Zhao, L. Wang, J. Liu, Y. Li, Z. Liang, X. He, X. Li, N. Tavajohi, B. Li, J. Energy Chem., 59 (2021) 83-99.

[17] J. Asenbauer, T. Eisenmann, M. Kuenzel, A. Kazzazi, Z. Chen, D. Bresser, Sustain. Energy Fuels, 4 (2020) 5387-5416.

[18] M. Gu, Y. He, J. Zheng, C. Wang, Nano Energy, 17 (2015) 366-383.

[19] T.-w. Kwon, Y.K. Jeong, E. Deniz, S.Y. AlQaradawi, J.W. Choi, A. Coskun, ACS Nano, 9 (2015) 11317-11324.

[20] L. Sun, Y. Liu, R. Shao, J. Wu, R. Jiang, Z. Jin, Energy Storage Mater., 46 (2022) 482-502.

[21] X. Zuo, J. Zhu, P. Müller-Buschbaum, Y.-J. Cheng, Nano Energy, 31 (2017) 113-143.

[22] S.D. Beattie, M.J. Loveridge, M.J. Lain, S. Ferrari, B.J. Polzin, R. Bhagat, R.

Dashwood, J. Power Sources, 302 (2016) 426-430.

[23] L. Sun, Y. Liu, J. Wu, R. Shao, R. Jiang, Z. Tie, Z. Jin, Small, 18 (2022) 2102894.

[24] J. Moon, H.C. Lee, H. Jung, S. Wakita, S. Cho, J. Yoon, J. Lee, A. Ueda, B. Choi, S. Lee, K. Ito, Y. Kubo, A.C. Lim, J.G. Seo, J. Yoo, S. Lee, Y. Ham, W. Baek, Y.-G. Ryu, I.T. Han, Nat. Commun., 12 (2021) 2714.

[25] Y.H. Xu, G. Yin, Y. Ma, P. Zuo, X. Cheng, J. Mater. Chem., 20 (2010).

[26] Y. Liu, Z. Tai, T. Zhou, V. Sencadas, J. Zhang, L. Zhang, K. Konstantinov, Z. Guo, H.K. Liu, Adv. Mater., 29 (2017) 1703028.

[27] N. Liu, Z. Lu, J. Zhao, M.T. McDowell, H.-W. Lee, W. Zhao, Y. Cui, Nat. Nanotechnol., 9 (2014) 187-192.

[28] J. Zhou, T. Qian, M. Wang, N. Xu, Q. Zhang, Q. Li, C. Yan, ACS Appl. Mater. Interfaces, 8 (2016) 5358-5365.

[29] M. Ashuri, Q. He, L.L. Shaw, Nanoscale, 8 (2016) 74-103.

[30] M.A. Azam, N.E. Safie, A.S. Ahmad, N.A. Yuza, N.S.A. Zulkifli, J Energy Storage, 33 (2021) 102096.

[31] Z. Chen, H. Zhang, T. Dong, P. Mu, X. Rong, Z. Li, ACS Applied Materials & Interfaces, 12 (2020) 47164-47180.

[32] F. Zou, A. Manthiram, Adv. Energy Mater., 10 (2020) 2002508.

[33] A.M. Grillet, T. Humplik, E.K. Stirrup, S.A. Roberts, D.A. Barringer, C.M.

Snyder, M.R. Janvrin, C.A. Apblett, Journal of The Electrochemical Society, 163 (2016) A1859-A1871.

[34] S.D. Beattie, D. Larcher, M. Morcrette, B. Simon, J.M. Tarascon, Journal of The Electrochemical Society, 155 (2008) A158.

[35] A. Gören, J. Mendes, H.M. Rodrigues, R.E. Sousa, J. Oliveira, L. Hilliou, C.M. Costa, M.M. Silva, S. Lanceros-Méndez, Journal of Power Sources, 334 (2016) 65-77.

[36] H.A. Lee, M. Shin, J. Kim, J.W. Choi, H. Lee, Adv. Mater., 33 (2021) 2007460.

[37] G. Zhang, Y. Yang, Y. Chen, J. Huang, T. Zhang, H. Zeng, C. Wang, G. Liu, Y. Deng, Small, 14 (2018) 1801189.

[38] L. Wei, C. Chen, Z. Hou, H. Wei, ScI. Rep., 6 (2016) 19583.

[39] T.M. Higgins, S.-H. Park, P.J. King, C. Zhang, N. McEvoy, N.C. Berner, D. Daly, A. Shmeliov, U. Khan, G. Duesberg, V. Nicolosi, J.N. Coleman, ACS Nano, 10 (2016) 3702-3713.

[40] Y. Gu, S. Yang, G. Zhu, Y. Yuan, Q. Qu, Y. Wang, H. Zheng, Electrochim. Acta, 269 (2018) 405-414.

[41] H. Buqa, M. Holzapfel, F. Krumeich, C. Veit, P. Novák, J. Power Sources, 161 (2006) 617-622.

[42] B. Lestriez, S. Bahri, I. Sandu, L. Roué, D. Guyomard, Electrochem. Commun., 9 (2007) 2801-2806.

[43] A. Magasinski, B. Zdyrko, I. Kovalenko, B. Hertzberg, R. Burtovyy, C.F.

Huebner, T.F. Fuller, I. Luzinov, G. Yushin, ACS Applied Materials & Interfaces, 2 (2010) 3004-3010.

[44] T.-w. Kwon, J.W. Choi, A. Coskun, Chem. Soc. Rev., 47 (2018) 2145-2164.

[45] P. Baruah, R. Duarah, N. Karak, Iran. Polym. J., 25 (2016) 849-861.

[46] M. Tian, P. Wu, ACS Appl. Energy Mater., 2 (2019) 5066-5073.

[47] W. Yan, M. Shi, C. Dong, L. Liu, C. Gao, Advances in Colloid and Interface Science, 284 (2020) 102267.

[48] Y. Jing, Y. Diao, X. Yu, React Funct Polym, 135 (2019) 16-22.

[49] J. Liu, H. Pu, S. Liu, J. Kan, C. Jin, Carbohydr. Polym., 174 (2017) 999-1017.

[50] J.-G. Han, C. Hwang, S.H. Kim, C. Park, J. Kim, G.Y. Jung, K. Baek, S. Chae, S.J. Kang, J. Cho, S.K. Kwak, H.-K. Song, N.-S. Choi, Advanced Energy Materials, 10 (2020) 2000563.

[51] Y. Jing, Y. Diao, X. Yu, Reactive and Functional Polymers, 135 (2019) 16-22.

[52] İ. Gülçin, Z. Huyut, M. Elmastaş, H.Y. Aboul-Enein, Arabian Journal of Chemistry, 3 (2010) 43-53.

[53] A. Rolt, L.S. Cox, BMC Chemistry, 14 (2020) 50.

[54] D. Jeong, J. Shim, H. Shin, J.-C. Lee, ChemSusChem, 13 (2020) 2642-2649.

[55] J. Shim, K.Y. Bae, H.J. Kim, J.H. Lee, D.-G. Kim, W.Y. Yoon, J.-C. Lee, ChemSusChem, 8 (2015) 4133-4138.

[56] Y. Jiang, X. Yan, Z. Ma, P. Mei, W. Xiao, Q. You, Y. Zhang, Polymers (Basel), 10 (2018).

[57] Z. Yi, Y. Zhao, P. Li, K. Ho, N. Blozowski, G. Walker, S. Jaffer, J. Tjong, M. Sain, Z. Lu, Applied Surface Science, 448 (2018) 583-588.

[58] L. Pan, H. Wang, C. Wu, C. Liao, L. Li, ACS Applied Materials & Interfaces, 7 (2015) 16003-16010.

[59] J.-S. Lee, C.-H. Jung, S.-Y. Jo, J.-H. Choi, I.-T. Hwang, Y.-C. Nho, Y.-M. Lee, J.-S. Lee, Journal of Polymer Science Part A: Polymer Chemistry, 48 (2010) 2725-2731.

[60] A. Zhang, J. Li, S. Zhang, Y. Mu, W. Zhang, J. Li, RSC Adv., 7 (2017) 35135-35146.

[61] L. Chupin, C. Motillon, F. Charrier-El Bouhtoury, A. Pizzi, B. Charrier, Ind Crops Prod, 49 (2013) 897-903.

[62] J. Wu, W. Liao, J. Zhang, W. Chen, J. Therm. Anal. Calorim, 135 (2019) 2329-2335.

[63] I.I. Koleva, T.A. van Beek, J.P.H. Linssen, A.d. Groot, L.N. Evstatieva, Phytochem. Anal, 13 (2002) 8-17.

[64] Y. Gang, T.-Y. Eom, S.D. Marasinghe, Y. Lee, E. Jo, C. Oh, Mar. Drugs, 19 (2021) 256.

[65] K. Sirivibulkovit, S. Nouanthavong, Y. Sameenoi, Anal. Sci, 34 (2018) 795-800.

[66] İ. Gülçin, Z. Huyut, M. Elmastaş, H.Y. Aboul-Enein, Arab. J. Chem., 3 (2010) 43-53.

[67] Z. Aytac, S.I. Kusku, E. Durgun, T. Uyar, Food Chem., 197 (2016) 864-871.

[68] J.-G. Han, C. Hwang, S.H. Kim, C. Park, J. Kim, G.Y. Jung, K. Baek, S. Chae, S.J. Kang, J. Cho, S.K. Kwak, H.-K. Song, N.-S. Choi, Adv. Energy. Mater., 10 (2020) 2000563.

[69] Q. Zhang, C. Zhang, W. Luo, L. Cui, Y.-J. Wang, T. Jian, X. Li, Q. Yan, H. Liu, C. Ouyang, Y. Chen, C.-L. Chen, J. Zhang, Adv. Sci., 7 (2020) 2000749.

[70] X. Wan, T. Mu, B. Shen, Q. Meng, G. Lu, S. Lou, P. Zuo, Y. Ma, C. Du, G. Yin, Nano Energy, 99 (2022) 107334.

[71] B. Koo, H. Kim, Y. Cho, K.T. Lee, N.S. Choi, J. Cho, Angew. Chem., 124 (2012) 8892-8897.

[72] X. Jiao, X. Yuan, J. Yin, F. Boorboor Ajdari, Y. Feng, G. Gao, J. Song, ACS Appl. Energy Mater., 4 (2021) 10306-10313.

[73] Y. Wang, H. Xu, X. Chen, H. Jin, J. Wang, Energy Storage Mater., 38 (2021) 121-129.

[Ⅳ. Cross-Linked Organic/Inorganic Polymer Binder]

[1] Y. Chen, Y. Kang, Y. Zhao, L. Wang, J. Liu, Y. Li, Z. Liang, X. He, X. Li, N. Tavajohi, B. Li, Journal of Energy Chemistry, 59 (2021) 83-99.

[2] J. Ma, Y. Li, N.S. Grundish, J.B. Goodenough, Y. Chen, L. Guo, Z. Peng, X. Qi, F. Yang, L. Qie, C.-A. Wang, B. Huang, Z. Huang, L. Chen, D. Su, G. Wang, X. Peng, Z. Chen, J. Yang, S. He, X. Zhang, H. Yu, C. Fu, M. Jiang, W. Deng, C.-F. Sun, Q. Pan, Y. Tang, X. Li, X. Ji, F. Wan, Z. Niu, F. Lian, C. Wang, G.G. Wallace, M. Fan, Q. Meng, S. Xin, Y.-G. Guo, L.-J. Wan, Journal of Physics D: Applied Physics, 54 (2021) 183001.

[3] M. Hoel, S. Kverndokk, Resource and Energy Economics, 18 (1996) 115-136.

[4] R. Gross, M. Leach, A. Bauen, Environment International, 29 (2003) 105-122.

[5] Poonam, K. Sharma, A. Arora, S.K. Tripathi, Journal of Energy Storage, 21 (2019) 801-825.

[6] A. González, E. Goikolea, J.A. Barrena, R. Mysyk, Renewable and Sustainable Energy Reviews, 58 (2016) 1189-1206.

[7] M. Vangari, T. Pryor, L. Jiang, Journal of Energy Engineering, 139 (2013) 72-79.

[8] S. Chakraborty, M. N. L, Journal of The Electrochemical Society, 169 (2022) 020552.

[9] N.I. Jalal, R.I. Ibrahim, M.K. Oudah, Journal of Physics: Conference Series, 1973 (2021) 012015.

[10] S. Fleischmann, J.B. Mitchell, R. Wang, C. Zhan, D.-e. Jiang, V. Presser, V.

Augustyn, Chemical Reviews, 120 (2020) 6738-6782.

[11] J.P. Zheng, P.J. Cygan, T.R. Jow, Journal of The Electrochemical Society, 142 (1995) 2699-2703.

[12] J.-T. Li, Z.-Y. Wu, Y.-Q. Lu, Y. Zhou, Q.-S. Huang, L. Huang, S.-G. Sun, Advanced Energy Materials, 7 (2017) 1701185.

[13] J. Zhang, M. Li, H.A. Younus, B. Wang, Q. Weng, Y. Zhang, S. Zhang, Nano Materials Science, 3 (2021) 124-139.

[14] I. Kovalenko, B. Zdyrko, A. Magasinski, B. Hertzberg, Z. Milicev, R. Burtovyy, I. Luzinov, G. Yushin, Science, 334 (2011) 75-79.

[15] A. Magasinski, B. Zdyrko, I. Kovalenko, B. Hertzberg, R. Burtovyy, C.F. Huebner, T.F. Fuller, I. Luzinov, G. Yushin, ACS Applied Materials & Interfaces, 2 (2010) 3004-3010.

[16] J.S. Bridel, T. Azaïs, M. Morcrette, J.M. Tarascon, D. Larcher, Chemistry of Materials, 22 (2010) 1229-1241.

[17] L. Fransson, T. Eriksson, K. Edström, T. Gustafsson, J.O. Thomas, Journal of Power Sources, 101 (2001) 1-9.

[18] S.S. Zhang, T.R. Jow, Journal of Power Sources, 109 (2002) 422-426.

[19] D. Guy, B. Lestriez, D. Guyomard, Advanced Materials, 16 (2004) 553-557.

[20] C.K. Chan, H. Peng, G. Liu, K. McIlwrath, X.F. Zhang, R.A. Huggins, Y. Cui, Nature Nanotechnology, 3 (2008) 31-35.

[21] A.M. Grillet, T. Humplik, E.K. Stirrup, S.A. Roberts, D.A. Barringer, C.M. Snyder, M.R. Janvrin, C.A. Apblett, Journal of The Electrochemical Society, 163 (2016) A1859-A1871.

[22] S. Rajeevan, S. John, S.C. George, Journal of Energy Storage, 39 (2021) 102654.

[23] Y. Sun, X. Liu, Y. Jiang, J. Li, J. Ding, W. Hu, C. Zhong, Journal of Materials Chemistry A, 7 (2019) 18183-18208.

[24] C. Chen, H. Ma, Y. Wang, Highlights in Science, Engineering and Technology, 3 (2022) 31-42.

[25] R.D. Lahiru Sandaruwan, R. Kuramoto, B. Wang, S. Ma, H. Wang, Langmuir, 38 (2022) 8934-8942.

[26] H.L. Leira, A. Tiltnse, K. Svendsen, L. Vetlesen, Contact Dermatitis, 27 (1992) 148-150.

[27] V. Haufroid, V.K. Jaeger, S. Jeggli, R. Eisenegger, A. Bernard, D. Friedli, D. Lison, P. Hotz, International Archives of Occupational and Environmental Health, 87 (2014) 663-674.

[28] Z.W. Seh, Q. Zhang, W. Li, G. Zheng, H. Yao, Y. Cui, Chemical Science, 4 (2013) 3673-3677.

[29] F. Zou, A. Manthiram, Advanced Energy Materials, 10 (2020) 2002508.

[30] R. Ni, J. Peng, M. Wen, H. Peng, Z. Zhang, S. Li, X. Wang, J. Chen, D. Long, H. Xian, Analytical Methods, 12 (2020) 324-332.

[31] Y.S. Chi, J.K. Lee, S.-g. Lee, I.S. Choi, Langmuir, 20 (2004) 3024-3027.

[32] S. Mallakpour, M. Naghdi, Progress in Materials Science, 97 (2018) 409-447.

[33] C.P. Fredlake, J.M. Crosthwaite, D.G. Hert, S.N.V.K. Aki, J.F. Brennecke, Journal of Chemical & Engineering Data, 49 (2004) 954-964.

[34] M.G. Freire, P.J. Carvalho, A.M. Fernandes, I.M. Marrucho, A.J. Queimada, J.A.P. Coutinho, Journal of Colloid and Interface Science, 314 (2007) 621-630.

[35] S.-I. Kim, J.-S. Lee, H.-J. Ahn, H.-K. Song, J.-H. Jang, ACS Applied Materials & Interfaces, 5 (2013) 1596-1603.

[36] Y. Zhao, X. Zhang, X. Xu, Y. Zhao, H. Zhou, J. Li, H. Jin, CrystEngComm, 18 (2016) 4836-4843.

[37] J.-S. Lee, C.-H. Jung, S.-Y. Jo, J.-H. Choi, I.-T. Hwang, Y.-C. Nho, Y.-M. Lee, J.-S. Lee, Journal of Polymer Science Part A: Polymer Chemistry, 48 (2010) 2725-2731.

[38] J. Yuan, M. Antonietti, Macromolecules, 44 (2011) 744-750.

[39] R. Marcilla, J. Alberto Blazquez, J. Rodriguez, J.A. Pomposo, D. Mecerreyes, Journal of Polymer Science Part A: Polymer Chemistry, 42 (2004) 208-212.

[40] T. Oh, C. Choi, Journal of the Korean Physical Society, 56 (2010) 1150-1155.

[41] J.-S. Lee, K. Sakaushi, M. Antonietti, J. Yuan, RSC Advances, 5 (2015) 85517-85522.

[42] X. Chen, J. Zhao, J. Zhang, L. Qiu, D. Xu, H. Zhang, X. Han, B. Sun, G. Fu,

Y. Zhang, F. Yan, Journal of Materials Chemistry, 22 (2012) 18018-18024.

[43] N. Pekel, Z.M.O. Rzaev, O. Güven, Macromolecular Chemistry and Physics, 205 (2004) 1088-1095.

[44] M. Mecozzi, M. Pietroletti, M. Scarpiniti, R. Acquistucci, M.E. Conti, Environmental Monitoring and Assessment, 184 (2012) 6025-6036.

[45] L. Wei, C. Chen, Z. Hou, H. Wei, Scientific Reports, 6 (2016) 19583.

[46] L. Chen, X. Xie, J. Xie, K. Wang, J. Yang, Journal of Applied Electrochemistry, 36 (2006) 1099-1104.

[47] J. Liu, P. Chen, L. Deng, J. He, L. Wang, L. Rong, J. Lei, Scientific Reports, 5 (2015) 15576.

[48] D.U. Lee, J. Fu, M.G. Park, H. Liu, A. Ghorbani Kashkooli, Z. Chen, Nano Letters, 16 (2016) 1794-1802.

[49] A. Sankar, S.V. Chitra, M. Jayashree, M. Parthibavarman, T. Amirthavarshini, Diamond and Related Materials, 122 (2022) 108804.

[50] M. Liu, J. Chang, J. Sun, L. Gao, RSC Advances, 3 (2013) 8003-8008.

[51] S. Goel, A.K. Tomar, R.K. Sharma, G. Singh, ACS Applied Energy Materials, 1 (2018) 1540-1548.

[52] J.Y. Chu, K.H. Lee, A.R. Kim, D.J. Yoo, Journal of Membrane Science, 611 (2020) 118385.

[53] M. Moussa, M.F. El-Kady, D. Dubal, T.T. Tung, M.J. Nine, N. Mohamed, R.B.

Kaner, D. Losic, ACS Applied Energy Materials, 3 (2020) 923-932.

[54] H.W. Jiang, Y. Yang, Y.M. Nie, Z.F. Su, Y.F. Long, Y.X. Wen, J. Su, RSC Adv, 12 (2022) 5997-6006.

[55] L. Xu, H. Xin, C. Su, Polymer Bulletin, 79 (2022) 5261-5278.